REPORT DOCUMENTATION PAGE

OMB No. 0704-0188

1. AGENCY USE ONLY (Leave blank)	2. REPORT DATE May 95	3. REPORT TYPE AND DATES COVERED

4. TITLE AND SUBTITLE
Spatical information content Analysis of Optical Polarimetric Imagery

5. FUNDING NUMBERS

6. AUTHOR(S)
Ian A. North

7. PERFORMING ORGANIZATION NAME(S) AND ADDRESS(ES)
AFIT Students Attending:

State University of New York

8. PERFORMING ORGANIZATION REPORT NUMBER
AFIT/CI/CIA
95-011D

9. SPONSORING/MONITORING AGENCY NAME(S) AND ADDRESS(ES)
DEPARTNEMT OF THE AIR FORCE
AFIT/CI
2950 P STREET, BDLG 125
WRIGHT-PATTERSON AFB OH 45433-7765

10. SPONSORING/MONITORING AGENCY REPORT NUMBER

DTIC
SELECTED
JUN 1 9 1995

11. SUPPLEMENTARY NOTES

12a. DISTRIBUTION/AVAILABILITY STATEMENT
Approved for Public Release IAW AFR 190-1
Distribution Unlimited
BRIAN D. GAUTHIER, MSgt, USAF
Chief Administration

12b. DISTRIBUTION CODE
F

13. ABSTRACT (Maximum 200 words)

19950615 065

14. SUBJECT TERMS

15. NUMBER OF PAGES
176

16. PRICE CODE

17. SECURITY CLASSIFICATION OF REPORT	18. SECURITY CLASSIFICATION OF THIS PAGE	19. SECURITY CLASSIFICATION OF ABSTRACT	20. LIMITATION OF ABSTRACT

DTIC QUALITY INSPECTED 5

Abstract

NORTH, JAN A., <u>Spatial Information Content Analysis of Optical Polarimetric Imagery</u>. Typed and bound thesis, 176 pages, 11 tables, 113 figures, and 123 equations, May 1995.

In this study the spatial information content of optical polarimetric (Stokes vector) imagery of both synthetic and natural scenes is analyzed. The intent of this study is to evaluate the utility of polarimetric imagery in the extraction of spatial information content from scenes containing spatially correlated features that can be described by their spatial (two-dimensional) power spectra.

This study was conducted in four phases: 1) construct an imaging polarimeter system for the purpose of collecting representative imagery containing both synthetic and natural scenes of spatially correlated features illuminated under clear sky conditions; 2) process the collected image data to create the Stokes vector images and derivative images; 3) construct a polarimetric imaging simulation for the purpose of comparing synthetic data with actual results; and 4) analyze both the synthetic and actual Stokes imagery for the purpose of evaluating the spatial information content of the processed scenes.

Analysis of the study results produced five main conclusions: 1) characteristic curve co-calibration of the input images is important for the accurate calculation of the Stokes parameters and derivatives; 2) the polarimetric difference (D) image provides a direct measurement of sensitometric co-calibration error; 3) the polarization ellipse orientation angle (T) image histogram can provide an indirect measure of the azimuthal difference between the principal plane and the polarizer reference plane; 4) the percent polarization (P) and orientation angle (T) components provide more stable estimates of spatial power spectral density (PSD) compared with the unpolarized intensity (I) component; and 5) the PSD stablities of the P and T components demonstrate a relative insensitivity to imaging geometry compared with the I component.

The results of this study provide a refined understanding of the potential contributions that polarimetric imagery can provide in the analysis of spatial information content from optical imagery.

Author's name in full: **Jan Arthur North**

Candidate for the degree of   **Doctor of Philosophy**

Date of defense: **02 May 1995**

Major Professor: **Dr. Michael J. Duggin**

Faculty of Environmental and Resource Engineering

State University of New York (SUNY) College of Environmental Science and Forestry (ESF), Syracuse New York

Signature of Major Professor: _____
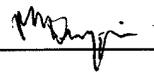
Acknowledgments

I would like to thank Dr. Mike Duggin for his mentorship and guidance in the many aspects and details of this study; in particular, thanks for bringing the uniqueness of this topic to light; also, thanks for providing the wherewithal to execute the airborne collection phase of this research.

Thanks to all the members of the Facility for Image Processing and Remote Sensing at SUNY ESF (FIRS) for their kind assistance during the many phases of this study; in particular, thanks to Captain Darryl Murdock (USAR) for his superb aviator skills.

Thanks to the members of my examining committees for their academic oversight, consideration, and forbearance: Drs. Bob Brock, Jim Hassett, Lee Herrington, Rosemary Kennett, Dave Kieber, Robin Kimmerer, and Chuck Lee.

Finally, I'd like to thank my sponsor, the United States Air Force Institute of Technology (AFIT) Directorate of Civilian Institution Programs, for giving me this remarkable opportunity to pursue a doctorate while on active duty.

iii

Dedication

To

Kathy, Hollie, and Janson,

for keeping the light on

at the end of the tunnel.

Table of Contents

1.0   Introduction

1.1   Purpose

The purpose of this study is to obtain an improved understanding of the contribution that sensed polarization can provide in the analysis of spatial information content from optical imagery. Toward that end, the primary focus is to obtain both qualitative and quantitative evaluations of the utility of optical polarimetric (Stokes vector) imagery in the extraction of spatial information content from scenes containing spatially correlated features that can be described by their spatial power spectra. Polarimetric imagery containing both natural and synthetic scene features are analyzed.

1.2   Objectives

This objectives of this investigation are described in four phases:

Phase 1 - Image Data Collection

Construct an imaging polarimeter system using a 4-lens 35-mm camera with linearly polarizing filters differentially rotated about their optic axes. Execute a controlled experiment: collect representative polarized imagery containing both synthetic and natural scenes of spatially correlated features illuminated under naturally polarized (clear sky) illumination conditions.

Phase 2 - Image Data Processing

Process the differentially polarized image sets to create calibrated Stokes parameter images and Stokes derivative images: convert the photographic images into digital images; co-register the digital images; co-calibrate the images for relative sensitometry; and then mathematically combine the co-registered, co-calibrated digital images to create the Stokes parameter and Stokes derivative imagery.

Phase 3 - Image Data Simulation

Synthesize a reasonable imaging model which can simulate the effects of resolving differentially polarized imagery of a mirror-reflected skydome under various imaging geometries. Exercise the model to create synthetic images which can be compared with actual calibration images of the mirror-reflected skydome.

Phase 4 - Image Data Analysis

Analyze the errors associated with calibrating the Stokes parameter and Stokes derivative imagery from digitally processed, 4-lens 35-mm polarized photographs.

Analyze and compare both the synthetic and actual polarized image features: specify sub-images within each image that contain similar in-scene content and texture; transform these sub-images into their spatial power spectra; analyze and compare the resulting spectra to determine the effects that imaging geometry may have on the stability of spatial spectral estimation for each of the polarized image components (i.e., the Stokes parameter and Stokes derivative images).

1.3 Motivation

The prime motivation for this study is to utilize a large body of current research of one spatially correlated natural feature, wind-driven waterwave surfaces, as the basis for the study of other natural background and clutter features, definable by their spatial power (Wiener) spectra, under polarized optical imaging conditions. A secondary motivation is to consider the potential utility of polarized waterwave scenes as natural opportunistic targets for synoptic image calibration. This motivation is based on several unique aspects of water and waterwaves enumerated below. A final motivation is to demonstrate the feasibility of extending this analysis to more sophisticated imaging systems, using the relatively simple techniques employed in this study.

There are several reasons for selecting natural waterwave surfaces (and their simulcra) as the initial object of polarized image analysis:

1) Terrestrial surface water is ubiquitous; fully three quarters of the Earth's surface is covered with water. For airborne and spaceborne sensors, this represents a large window of opportunity to image this natural feature, even in the presence of clouds.

2) In comparison with other terrestrial surface features, water surfaces are optically homogeneous: only two radiance functions, one for surface reflection and one for upwelling subsurface refraction (i.e., volume reflectance), are required to describe the unique radiance contribution of the imaged water scene. However, in the visible red region (and at longer wavelengths), water is increasingly opaque to the point that only surface reflection (and/or emission in the infrared) requires description.

3) Except for the rare instances of sustained windlessness where water is smooth and specular, its surface is disturbed by the addition of directional friction energy applied by wind passing over it. Up to a defined maximum wind velocity, the disturbed surface remains analytic (infinitely differentiable) and can be described as a quasi-stationary, pseudo-Gaussian process; the resulting power spectrum approximations for elevation, slope, and curvature can be analyzed by Fourier methods [Kinsman,1965]. See, for example, Figure 1.3-1.
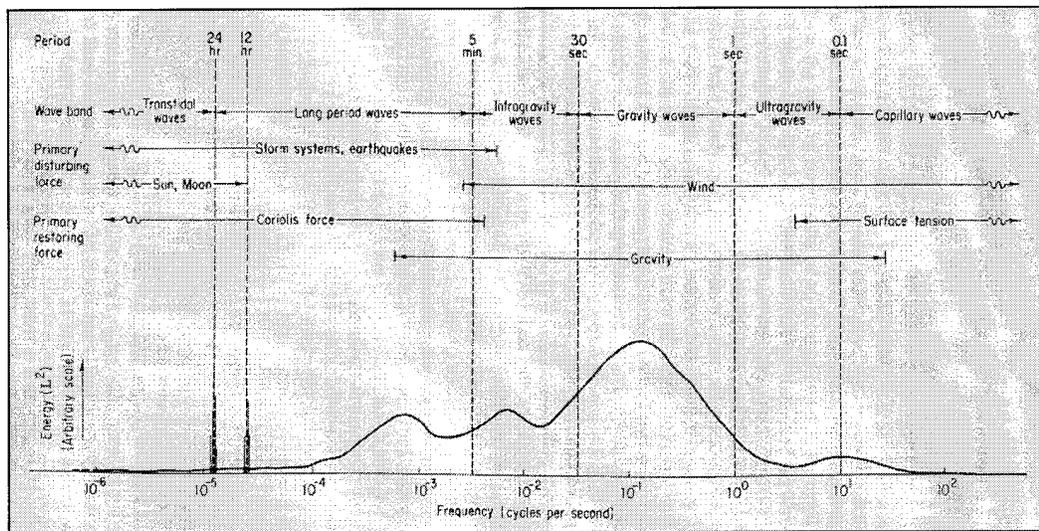
Figure 1.3-1. Schematic representation of the energy contained in the surface waves of the oceans - in fact, a guess at the power spectrum [from Kinsman, 1965].

4) As an extension of 3), waterwaves can be imaged over several orders of spatial frequency. Also, the well-behaved surface statistics of waterwave surfaces (e.g., mean slope = 0°, 3-sigma slope << 30°) allow for a broad range of off-vertical imaging geometries without having to consider the complex effects of surface obscuration. See, for example, Figure 1.3-2.

5) Also as an extension of 3), the assumption of quasi-spatial and quasi-temporal invariance of local surface spectra allows for considerable

4

tolerance in both image collection and processing: precise pointing to an exact ground reference point by multiple sensors is not critical; precise collection timing by multiple sensors is not critical; and the registration of multi-sensor imagery is not required.
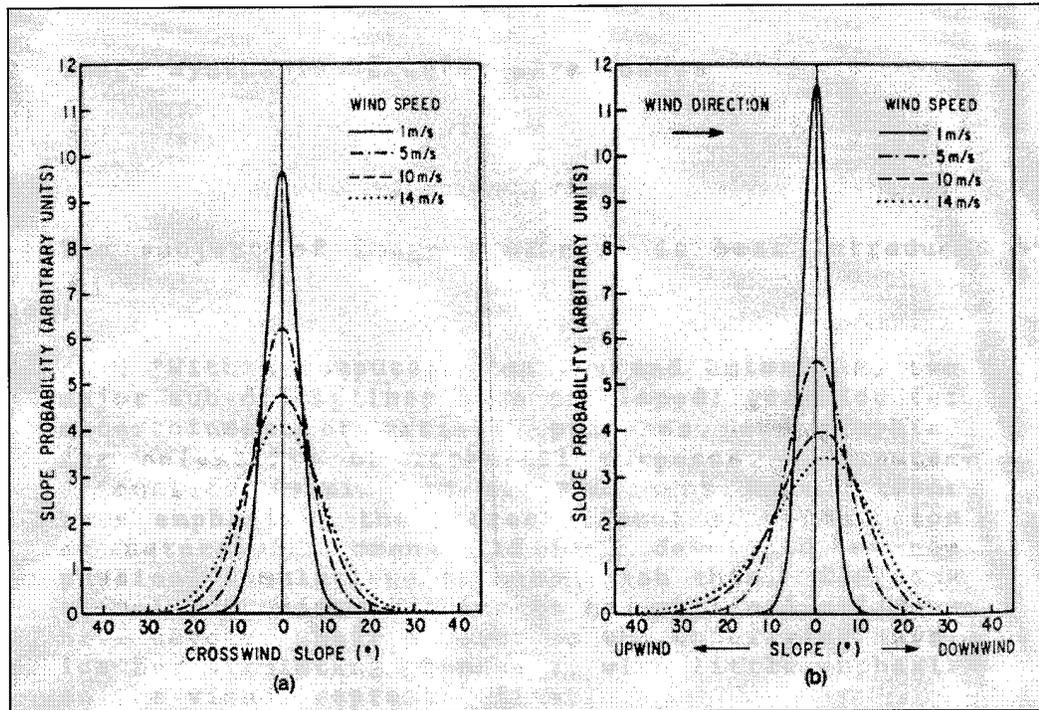

Figure 1.3-2. Facet slope angle (beta) probability distribution for a wind-roughened water surface, computed for various wind speeds [from Sidran, 1981].

6) Finally, the natural air-water interface represents a strong polarizing dielectric. High contrasts within and between polarized images should be readily detectable in a significant range of imaging geometries.

In sum, this study will exploit one of the more analytically straightforward terrestrial surface features, and its simulation, for the evaluation of polarized (Stokes vector) imagery in the extraction of texture information from more complex scenes of spatially correlated features (such as cultivated forests and fields) that can be described by their spatial power spectra.

5

2.0 Literature review

The full literature review consists of three sections:

Overview of optical polarization - This section provides a fundamental description of optical polarization and its measurement. The work of Maxwell, Stokes, Malus, Brewster, Fresnel,Young, Snell, *et al.*, is highlighted.

Polarimetric image analysis - This section provides a review of research that advances the use of imaging techniques to measure the polarization state of sensed spatial radiation distributions.

Spatial information content analysis - This section provides a review of research that advances the use of imaging techniques to analyze the spatial information content of scenes, to include spatial spectrum analysis. The analysis of remotely sensed waterwave scenes is emphasized.

2.1 Overview of optical polarization

Maxwell's Equations

The property of polarization is common to all transverse vector waves, to include all electromagnetic waves. The complete description of an electromagnetic wave requires four field vectors:

E = the electric-field strength,

B = the magnetic-flux density,

D = the electric-displacement density, and

H = the magnetic-field strength,

that are interrelated by Maxwell's equations:

$$\mathbf{D} = \varepsilon_m \varepsilon_0 \mathbf{E},$$

<div style="text-align: right;">Equation 2-1</div>

$$\mathbf{B} = \mu_m \mu_0 \mathbf{H},$$

<div style="text-align: right;">Equation 2-2</div>

$$\text{div } \mathbf{D} = 4\pi p,$$

<div style="text-align: right;">Equation 2-3</div>

$$\text{div } \mathbf{B} = 0,$$

<div style="text-align: right;">Equation 2-4</div>

$$d\mathbf{D}/dt = w\varepsilon_m\varepsilon_0 \, d\mathbf{E}/dt = c \text{ curl } \mathbf{H} - 4\pi j,$$

<div style="text-align: right;">Equation 2-5</div>

and

$$d\mathbf{B}/dt = w\mu_m\mu_0 \, d\mathbf{H}/dt = -c \text{ curl } \mathbf{E},$$

<div style="text-align: right;">Equation 2-6</div>

where

ε = the electric permittivity, or dielectric constant, of the medium under consideration (ε_m) and of free space (ε_0),

μ = the magnetic permeability of the medium under consideration (μ_m) and of free space (μ_0),

p = the electric charge density,

c = the velocity of light in free space,

j = the electric field current,

w = the cross-sectional area of the medium normal to the direction of propagation,

and where the vector operators, **div** (divergence) and **curl**, can be expressed in the form of differential equations:

$$DIVergence\ of\ F = \frac{\partial F_x}{\partial x} + \frac{\partial F_y}{\partial y} + \frac{\partial F_z}{\partial z}$$

Equation 2-7

and

$$CURL\ of\ F = \left[\left(\frac{\partial F_z}{\partial y} - \frac{\partial F_y}{\partial z} \right) \ \left(\frac{\partial F_x}{\partial z} - \frac{\partial F_z}{\partial x} \right) \ \left(\frac{\partial F_y}{\partial x} - \frac{\partial F_x}{\partial y} \right) \right]$$

Equation 2-8

Polarization of an electromagnetic wave refers to the variation of one of these four vectors with respect to time, t, at a fixed spatial observation point, s. Of the four field vectors, convention defines the state of light polarization relative to the **E**-vector; the reasoning behind this choice of convention is that, for light-matter interactions, the electric field force exerted on the material electrons by a light wave is much larger than that of its magnetic field force:

> "The total force exerted by the electromagnetic field on a particle of charge q moving with velocity **v** consists of two terms: the electric force q**E** and the Lorentz force q**v** x **B**. The ratio of magnitudes of the latter to the former cannot exceed vB/E or v/c where c is the velocity of light. Because v/c << 1 (for all cases of interest), the Lorentz force can be neglected." [Azzam & Bashara, 1977]

Therefore, all subsequent polarization analysis will limit the description of light-matter interactions to the behavior of the electric-field strength vector **E(s,t)**.
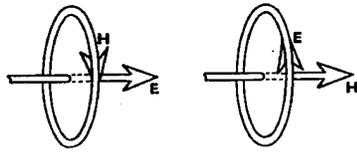
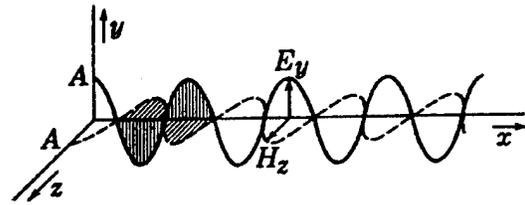**Figure 2.1-1.** Curl relationships between **E**- and **H**- vectors [from Partington, 1953].

Figure 2.1-2. E- and H-vectors in a linearly polarized monochromatic wave [from Jenkins & White, 1976].

Stokes Parameters

Any electromagnetic wave of arbitrary polarization can be mathematically represented by two orthogonal linearly polarized complex waves:

$$\mathbf{E}(\mathbf{s},t) = \mathbf{E}_x(z,t) + \mathbf{E}_y(z,t) ,$$

Equation 2-9

assuming **s** specifies the coordinates of a right-handed Cartesian system with the wave propagating along the z-axis in the positive direction. The two complex waves can then be analyzed into their real and imaginary components:

$$\mathbf{E}(\mathbf{s},t) =$$

Equation 2-10

$$E_0 e^{i\Phi} = E_{x0} e^{i\Phi_x} + E_{y0} e^{i\Phi_y}$$

$$= E_{x0} [\cos(\Phi_x) - i \sin(\Phi_x)] + E_{y0} [\cos(\Phi_y) - i \sin(\Phi_y)]$$

Finally, the general description of the two real component waves requires eight parameters as functions of z & t:

$E_x(z,t) = E_{x0} \cos(\Phi_x) = E_{x0}(t) \cos[(\omega t - kz) + \delta_x(t)]$,

<div align="right">| Equation 2-11 |</div>

and

$E_y(z,t) = E_{y0} \cos(\Phi_y) = E_{y0}(t) \cos[(\omega t - kz) + \delta_y(t)]$,

<div align="right">| Equation 2-12 |</div>

where

$E_x, E_y =$ the values of the electric field in the x & y direction, respectively, at position z and time t,

$E_{x0}, E_{y0} =$ the amplitude of the electric field oscillation in the x & y direction, respectively, at time t and z = 0,

$\omega =$ the angular frequency of the wave,

$k =$ the wavenumber of the wave = 2π/wavelength, and

$\delta_x, \delta_y =$ the phases (or epochs) of the electric field oscillation in the x & y direction, respectively, at time t.

Only four of these parameters - E_{x0}, E_{y0}, δ_x, and δ_y - are required to establish the equation of the state of the polarization ellipse at some fixed point along the wavetrain, e.g. z = 0:

$$\frac{E_x^2}{E_{x_0}^2} + \frac{E_y^2}{E_{y_0}^2} - \frac{2 E_x E_y \cos(\delta_y - \delta_x)}{E_{x_0} E_{y_0}} = \sin^2(\delta_y - \delta_x)$$

<div align="right">| Equation 2-13 |</div>

Note that the cross-product exists because the coordinate axes do not, in general, coincide with the axes of the ellipse.
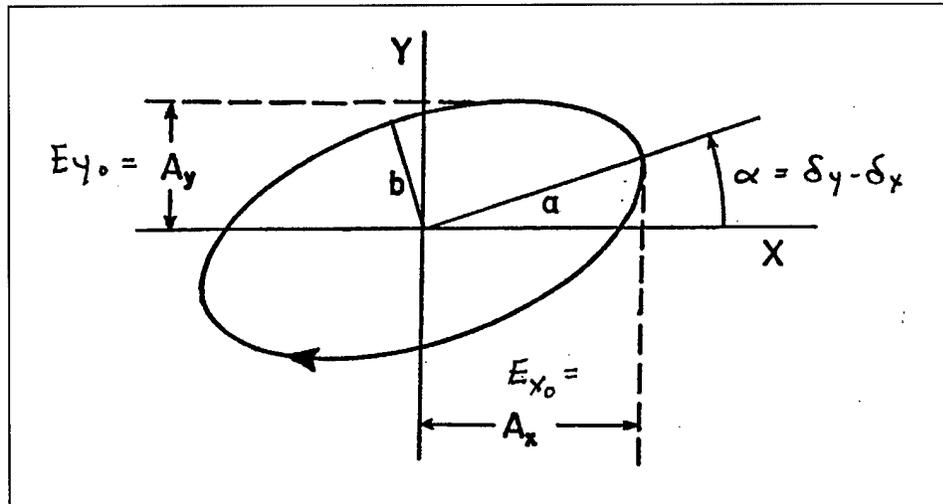

Figure 2.1-3. Specification of a polarization ellipse, using Shurcliff's notation: azimuth = a, ellipticity = b/a, handedness = right (+) [adapted from Shurcliff, 1962].

The Stokes vector, containing the four Stokes parameters, provides a more empirically accessible description of polarization for the more general case of partially polarized light, since they are directly derivable from measurable irradiance values:

$$\mathbf{S} = \{\ I,\ Q,\ U,\ V, \}\ ,$$

<div align="right">Equation 2-14</div>

where

$$I = (c\varepsilon_0/2)\ [<E_{x0}^2(t) + E_{y0}^2(t)>]\ ,$$

<div align="right">Equation 2-15</div>

the total irradiance of the light wave without respect to polarization (always positive),

$$Q = (c\varepsilon_0/2)\ [<E_{x0}^2(t) - E_{y0}^2(t)>]\ ,$$

<div align="right">Equation 2-16</div>

the differential irradiance measuring the preference for linear polarization along the x-axis (positive), y-axis (negative), or no preference (zero),

$$U = (c\varepsilon_0/2) \; [<2 \; E_{x0}(t) \; E_{y0}(t) \; \cos(\delta_y(t) - \delta_x(t))>] \; ,$$

<div style="text-align: right;">

Equation 2-17
</div>

the differential irradiance measuring the preference for linear polarization along the +45° bisector (positive), -45° bisector (negative), or no preference (zero), and

<div style="text-align: right;">

Equation 2-18
</div>

$$V = (c\varepsilon_0/2) \; [<2 \; E_{x0}(t) \; E_{y0}(t) \; \sin(\delta_y(t) - \delta_x(t))>],$$

the differential irradiance measuring the preference for circular polarization that is right-handed (positive), left-handed (negative), or no preference (zero).
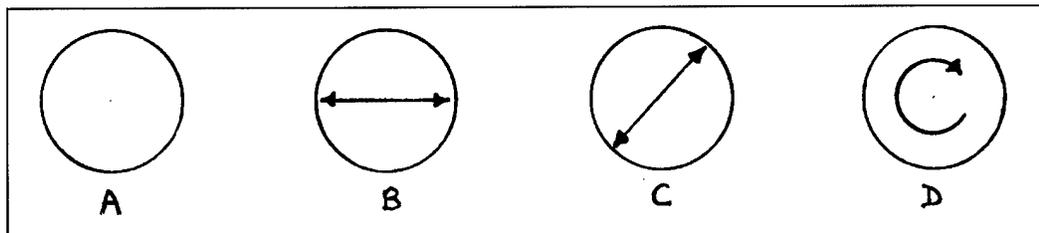
Figure 2.1-4 a,b,c,d. Schematic representation of the measured Stokes vector parameters I, Q, U, and V, respectively.

For the special case of monochromatic light, which by definition is perfectly polarized, the quantities $E_{x0}(t)$, $E_{y0}(t)$, $\delta_x(t)$, and $\delta_y(t)$ are time-independent, i.e., temporal averaging is not required.

$$< F(t) > \; = \; \frac{1}{T} \int_0^T F(t) \, dt$$

<div style="text-align: right;">

Equation 2-19
</div>

Note that < > specifies the temporal average of the enclosed quantities.

The parameters of the Stokes vector provide a full specification of the polarization ellipse:

$$Scale\ (Irradiance)\ =\ I\ =\ (\frac{c\varepsilon_0}{2})[\ E_{x_0}{}^2\ +\ E_{y_0}{}^2\ ]$$

<div style="text-align:right">Equation 2-20</div>

$$Azimuth = \frac{U}{Q} = \frac{2E_{x_0}E_{y_0}\cos(\delta_y - \delta_x)}{E_{x_0}{}^2 - E_{y_0}{}^2}$$

<div style="text-align:right">Equation 2-21</div>

$$Shape = \frac{|V|}{I} = \frac{2E_{x_0}E_{y_0}\sin(\delta_y - \delta_x)}{E_{x_0}{}^2 + E_{y_0}{}^2}$$

<div style="text-align:right">Equation 2-22</div>

and

$$Handedness\ =\ Sign\ Of\ V$$

<div style="text-align:right">Equation 2-23</div>

Another important description is fully consistent with the Stokes vector specification:

$$Irradiance\ =\ I$$

<div style="text-align:right">Equation 2-24</div>

$$Degree\ of\ Polarization\ =\ P\ =\ \frac{\sqrt{Q^2 + U^2 + V^2}}{I}$$

<div style="text-align:right">Equation 2-25</div>

$$Azimuth\ Angle\ =\ \Theta\ =\ \frac{1}{2}\ \tan^{-1}\left[\frac{U}{Q}\right]$$

<div style="text-align:right">Equation 2-26</div>

and

$$\textit{Ellipticity Angle} \; = \; \varepsilon \; = \; \frac{1}{2} \sin^{-1}\left(\frac{V}{\sqrt{Q^2 + U^2 + V^2}} \right)$$

The Stokes vector can then be recast using these parameters:

$$\mathbf{S} = I \{1, \; P \cos(2\varepsilon) \cos(2\Theta), \; P \cos(2\varepsilon) \sin(2\Theta), \; P \sin(2\varepsilon)\}$$

Alternatively, a derivative Stokes vector can be specified using these four independent parameters:

$$\mathbf{S}_{derivative} = \{ I, \; P, \; \Theta, \; \varepsilon \}$$

As an introduction to the next section of this chapter, it is this derivative Stokes vector that is of primary interest within this study. First, these derivative Stokes parameters have a more direct correlation with the physical properties of imaged features from which reflected polarized radiance is measured. Second, the Stokes parameters Q and U have a dependent variation with the azimuth angle of polarization ellipse Θ, as specified in Equation 2-27. As will be shown later, direct evaluation of the derivative Θ (or T) image provides a sensitive indication of the azimuthal deviation in polarimeter reference plane from its expected alignment with the principal plane, a deviation that would otherwise be masked as a systematic error within both the Q and U images.

Figure 2.1-5 provides examples of some common polarization forms and their Stokes vector representations. Note that the current Stokes' notation convention {I,Q,U,V} is replaced here by Shurcliff's notation {I,M,C,S}, after Perrin and Jones. (Stokes' initial notation was {A,B,C,D}.)

Table 2-1 Stokes parameter conventions			
Equation	Current	Shurcliff	Stokes
[2-14]	I	I	A
[2-15]	Q	M	B
[2-16]	U	C	C
[2-17]	V	S	D

Polarization form					Normalized Stokes vector,	Jones vector	
Sectional pattern	α (deg)	b/a	A_y/A_x	γ (deg)	$\{I,\ M,\ C,\ S\}$	Standard normalized	Full
———	0	0	0	—	$\{1,\ 1,\ 0,\ 0\}$	$\begin{bmatrix}1\\0\end{bmatrix}$	$\begin{bmatrix}A_x e^{i\varepsilon_x}\\0\end{bmatrix}$
|	90	0	∞	—	$\{1,\ -1,\ 0,\ 0\}$	$\begin{bmatrix}0\\1\end{bmatrix}$	$\begin{bmatrix}0\\A_y e^{i\varepsilon_y}\end{bmatrix}$
/	45	0	1	0	$\{1,\ 0,\ 1,\ 0\}$	$\frac{\sqrt{2}}{2}\begin{bmatrix}1\\1\end{bmatrix}$	$\begin{bmatrix}A_x e^{i\varepsilon_x}\\A_x e^{i\varepsilon_x}\end{bmatrix}$
\	-45	0	1	±180	$\{1,\ 0,\ -1,\ 0\}$	$\frac{\sqrt{2}}{2}\begin{bmatrix}1\\-1\end{bmatrix}$	$\begin{bmatrix}A_x e^{i\varepsilon_x}\\-A_x e^{i\varepsilon_x}\end{bmatrix}$
General	linear	0	Any positive number	0 or ±180	$\{1,\ \cos 2\alpha,\ \sin 2\alpha,\ 0\}$	$\begin{bmatrix}\cos R\\\pm\sin R\end{bmatrix}$	$\begin{bmatrix}A_x e^{i\varepsilon_x}\\\pm A_y e^{i\varepsilon_x}\end{bmatrix}$
⟳	—	$1,R$	1	90	$\{1,\ 0,\ 0,\ 1\}$	$\frac{\sqrt{2}}{2}\begin{bmatrix}-i\\1\end{bmatrix}$	$\begin{bmatrix}A_x e^{i\varepsilon_x}\\A_x e^{i(\varepsilon_x+\pi/2)}\end{bmatrix}$
⟲	—	$1,L$	1	-90	$\{1,\ 0,\ 0,\ -1\}$	$\frac{\sqrt{2}}{2}\begin{bmatrix}i\\1\end{bmatrix}$	$\begin{bmatrix}A_x e^{i\varepsilon_x}\\A_x e^{i(\varepsilon_x-\pi/2)}\end{bmatrix}$
⬭	0	$\frac{1}{2},R$	$\frac{1}{2}$	90	$\{1,\ 0.6,\ 0,\ 0.8\}$	$\frac{2\sqrt{5}}{5}\begin{bmatrix}-i\\\frac{1}{2}\end{bmatrix}$	$\begin{bmatrix}A_x e^{i\varepsilon_x}\\\frac{1}{2}A_x e^{i\left(\varepsilon_x+\frac{\pi}{2}\right)}\end{bmatrix}$
⬭	90	$\frac{1}{2},R$	2	90	$\{1,\ -0.6,\ 0,\ 0.8\}$	$\frac{2\sqrt{5}}{5}\begin{bmatrix}\frac{-i}{2}\\1\end{bmatrix}$	$\begin{bmatrix}A_x e^{i\varepsilon_x}\\2A_x e^{i\left(\varepsilon_x+\frac{\pi}{2}\right)}\end{bmatrix}$
⬭	22.5	0.318, R	0.518	45	$\left\{1,\ \sqrt{\frac{1}{3}},\ \sqrt{\frac{1}{3}},\ \sqrt{\frac{1}{3}}\right\}$ 0.325	$\begin{bmatrix}2.73\\1+i\end{bmatrix}$	$\begin{bmatrix}A_x e^{i\varepsilon_x}\\0.518 A_x e^{i\left(\varepsilon_x+\frac{\pi}{4}\right)}\end{bmatrix}$
General elliptical					$\begin{bmatrix}1\\\cos 2\omega \cos 2\lambda\\\cos 2\omega \sin 2\lambda\\\sin 2\omega\end{bmatrix}$	$\begin{bmatrix}(\cos R)e^{-i\frac{\chi}{2}}\\(\sin R)e^{i\frac{\chi}{2}}\end{bmatrix}$	$\begin{bmatrix}A_x e^{i\varepsilon_x}\\A_y e^{i\varepsilon_y}\end{bmatrix}$
General elliptical, partially polarized	$\dfrac{1}{\langle a_x^2 + a_y^2\rangle}$				$\begin{bmatrix}\langle a_x^2 + a_y^2\rangle\\\langle a_x^2 - a_y^2\rangle\\\langle 2a_x a_y \cos\gamma\rangle\\\langle 2a_x a_y \sin\gamma\rangle\end{bmatrix}$	None	None
Unpolarized					$\{1,\ 0,\ 0,\ 0\}$	None	None

Figure 2.1-5. Stokes vector parameters for various polarization forms [from Shurcliff, 1962].

Reflection Polarization

In 1808, the French scientist Etienne-Louise Malus discovered the polarization of light by its reflection from dielectric media:

"The Paris Academy had offered a prize for a mathematical
theory of double refraction, and Malus accordingly undertook
a study of the problem. He was standing at the window of
his house in the Rue d'Enfer one evening, examining a
calcite crystal. The Sun was setting, and its image reflected
toward him from the windows of the Luxemborg Palace not
far away. He held up the crystal and looked through it at the
Sun's reflection. To his astonishment, he saw one of the
double images disappear as he rotated the calcite. After the
Sun had set, he continued to verify his observations into the
night, using candlelight reflected from the surfaces of water
and glass." [Hecht, 1987]

Andrews [1960] offers some later details:

"After Malus' discovery Thomas Young pondered for eight
years how light waves could be polarized. Polarization was
being used as evidence for the corpuscular theory of light,
Suddenly the idea occurred to Young that if light waves were
transverse they could be polarized.

Sir David Brewster discovered a simple law to define
Malus' certain angle of incidence for which the light is
reflected from the dielectric surface is totally plane polarized:
The reflected light is plane polarized when the angle
between the reflected ray and the refracted ray is $\pi/2$
[radians or 90°]."

This certain angle of incidence Θ_{ip} at a dielectric interface is now referred
to as Brewster's angle. The simple geometric relation between Brewster's
law and Snell's law is:

$$n_i \sin \Theta_{ip} = n_t \sin \Theta_t \qquad \text{(Snell's Law)}$$

Equation 2-30

$$\Theta_p + \Theta_t = 90° \rightarrow \Theta_t = 90° - \Theta_p$$

Equation 2-31

$$n_i \sin \Theta_{ip} = n_t \sin (90° - \Theta_p) = n_t \cos \Theta_p$$

Equation 2-32

and

$$(n_t / n_i) = (\sin \Theta_p / \cos \Theta_p) = \tan \Theta_p \quad \text{(Brewster's Law)}$$

Equation 2-33

Figure 2.1-6 provides two illustrations of the geometric relationship between Brewster's law and Snell's law at a dielectric interface.
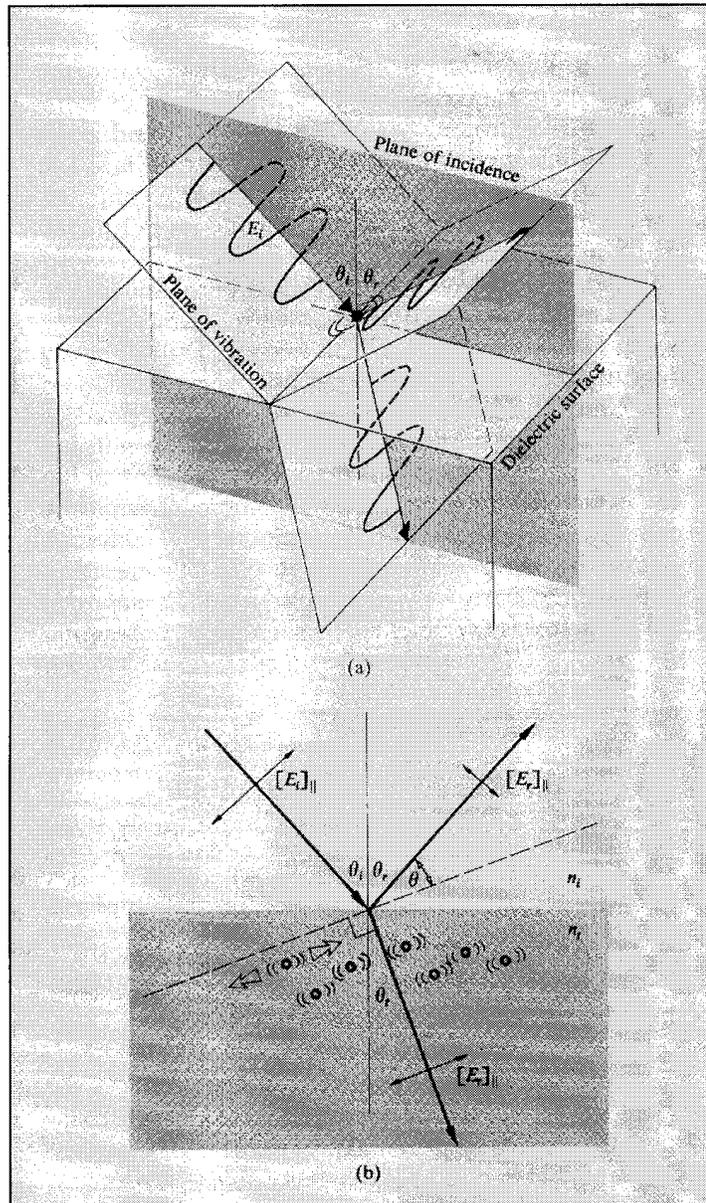

Figure 2.1-6 (a) and (b). Two schematic representations of the geometric relations between Brewster's law and Snell's law [from Hecht, 1987].

Application of Maxwell's equations to reflection polarization

Electromagnetic theory can be applied to confirm the empirical laws for reflection (to include Snell's and Brewster's) and to determine the polarization of the reflected beam, i.e., the amplitude, phase, and direction of the electric field **E**.

The laws of reflection and refraction can be derived from Maxwell's equations by imposing four boundary conditions:

1) the tangential components of magnetic force **H** are continuous across the dielectric boundary (Ampere's circuital law),

2) the tangential components of electric force **E** are continuous across the dielectric boundary (Faraday's law of induced electromotive force),

3) the normal components of electric displacement **D** are continuous across the dielectric boundary (Gauss' law), and

4) the normal components of magnetic induction **B** are continuous across the dielectric boundary (Gauss' law).

Electromagnetic theory predicts that when a wave crosses a dielectric boundary, i.e., a discontinuity in ε and μ, the amplitude reflection coefficients are dependent on the angle between the electric vector and the plane of incidence. These coefficients are determined from the following relations:

1) the vectors **E**, **H**, and the propagation vector **P**, are defined through Poynting's theorem: **S** = **E** x **H** (x is the cross-product),

2) from the ratio $E / H = \sqrt{(\mu\mu_0/\varepsilon\varepsilon_0)}$, refractive index $n = \sqrt{\varepsilon}$, $\mu \approx 1$ for both media at optical wavelengths, the relation between amplitudes E, H, and n is
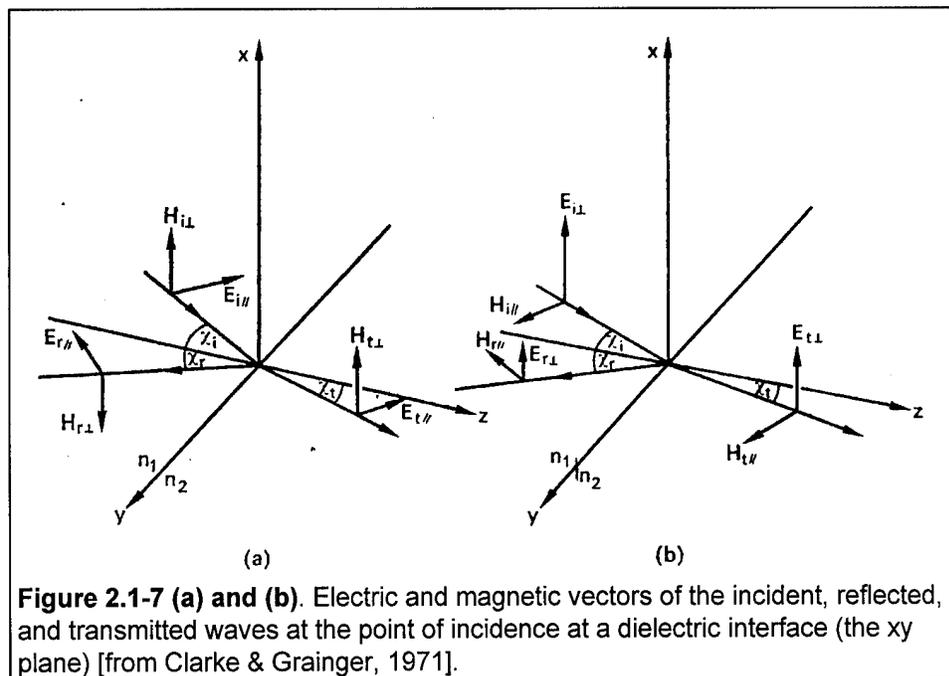
$$H = n \sqrt{(\varepsilon_0/\mu\mu_0)} E$$

| Equation 2-34 |

$$\approx n \sqrt{\varepsilon_0} E \text{ , and}$$

3) the components of **E** and **H** that are parallel to the dielectric boundary are continuous across it.

The remaining derivation follows from Clarke and Grainger [1971], using their figures and notation.

Figure 2.1-7 (a) and (b). Electric and magnetic vectors of the incident, reflected, and transmitted waves at the point of incidence at a dielectric interface (the xy plane) [from Clarke & Grainger, 1971].

<u>Case 1. $E_\parallel$ (parallel) to the incident plane [refer to Figure 2.1-7(a)].</u>

The continuous boundary condition for **E** and **H** is satisfied by

$$E_{i\parallel} \cos \chi_i + E_{r\parallel} \cos \chi_r = E_{t\parallel} \cos \chi_t$$

<div style="float:right">Equation 2-35</div>

and

$$H_{i\perp} - H_{r\perp} = H_{t\perp}$$

<div style="float:right">Equation 2-36</div>

The refractive index condition for E and H is satisfied by

$$n_1 E_{i\parallel} - n_1 E_{r\parallel} = n_2 E_{t\parallel}$$

<div style="float:right">Equation 2-37</div>

"The amplitude reflection coefficient is $E_{r\parallel}$ / $E_{i\parallel}$ = $r_\parallel$, say, and is easily seen from [the equations above] and the law of reflection ($x_i = x_r$), to be given by:

$$r_\parallel = -\frac{n_2 \cos \chi_i - n_1 \cos \chi_t}{n_2 \cos \chi_i + n_1 \cos \chi_t}$$

<div style="float:right">Equation 2-38</div>

Using the law of refraction that $n_1 \sin x_i = n_2 \sin x_t$, [this equation] reduces to:

$$r_\parallel = -\frac{\tan(\chi_i - \chi_t)}{\tan(\chi_i + \chi_t)}$$

<div style="float:right">Equation 2-39</div>

For angles of incidence not very different from zero, the two tangents are both positive and so the minus sign indicates that, in fact, the reflected wave undergoes a phase shift of π [radians] with respect to the situation shown in [figure (a)], i.e. nodality is predicted. For ($x_i + x_t$) = $\pi/2$ [radians], the reflection coefficient for $E_\parallel$ falls to zero and so the reflected beam can only contain a perpendicularly vibrating component. It is easy to

21

show that $(x_i + x_t) = \pi/2$ [radians] corresponds to a value for x_i of arctan(n_2/n_1). This angle of incidence is known as *Brewster's angle*. For x_i greater than Brewster's angle, $r_\parallel$ changes sign and becomes positive."
[Clarke & Grainger, 1971]

Case 2. $E_\perp$ (perpendicular) to the incident plane [refer to Figure 2.1-7(b)].

The continuous boundary condition for **E** and **H** is satisfied by

$$H_{i\parallel} \cos \chi_i \ + \ H_{r\parallel} \cos \chi_r \ = \ H_{t\parallel} \cos \chi_t$$

Equation 2-40

and

$$E_{i\perp} \ - \ E_{r\perp} \ = \ E_{t\perp}$$

Equation 2-41

The refractive index condition for E and H is satisfied by

$$n_1 E_{i\perp} \cos \chi_i \ - \ n_1 E_{r\perp} \cos \chi_r \ = \ n_2 E_{t\perp} \cos \chi_t$$

Equation 2-42

The amplitude reflection coefficient is $E_{r\perp} / E_{i\perp} = r_\perp$; once again, combining the equations above with the law of reflection ($x_i = x_r$), the reflection coefficient for $E_\perp$ is:

$$r_\perp \ = \ \frac{n_1 \cos \chi_i \ - \ n_2 \cos \chi_t}{n_1 \cos \chi_i \ + \ n_2 \cos \chi_t}$$

Equation 2-43

Again, using the law of refraction that $n_1 \sin x_i = n_2 \sin x_t$, this equation reduces to:

22

$$r_\perp = -\frac{\sin(\chi_i - \chi_t)}{\sin(\chi_i + \chi_t)}$$

The key insight in reflection polarization is that, at Brewster's angle, energy could only be directed to the production of an incident-plane wave if the wave was a longitudinal wave. The observation by Brewster, Fresnel, and ultimately Young (in 1817) that no such polarized wave is produced was taken as proof that light vibrations are transverse.

Stokes vector analysis of reflection polarization

The reflection matrix defined by Mueller calculus is of the form:

$$R = \frac{1}{2}\begin{bmatrix} \left(r_\perp^2 + r_\parallel^2\right) & \left(r_\perp^2 - r_\parallel^2\right) & 0 & 0 \\ \left(r_\perp^2 - r_\parallel^2\right) & \left(r_\perp^2 + r_\parallel^2\right) & 0 & 0 \\ 0 & 0 & \left(-2r_\perp r_\parallel\right) & 0 \\ 0 & 0 & 0 & \left(-2r_\perp r_\parallel\right) \end{bmatrix}$$

Mueller calculus will predict the Stokes vector of the reflected light by pre-multiplying the reflection Mueller matrix R by the Stokes vector of the incident light ray **S**:

$$\mathbf{S}_{reflection} = R\ \mathbf{S}_{incident}$$

The Mueller calculus, based on the work of Hans Mueller, is an empirical matrix-based formalism for treating all the possible physical transformations of Stokes vectors. Since the Stokes vector is a four-parameter vector, the Mueller operators are all 4 x 4 matrices.

Without resorting to the inclusion of a coordinate transformation matrix, the Stokes parameters here are presumed to be measured such that the z-axis corresponds to the direction of propagation and the x- and y-axes are respectively perpendicular and parallel to the plane of incidence.

The benefits of using this type of formalism (the Mueller calculus) are noted by Clarke and Grainger [1971]:

> "This one matrix succinctly summarizes all the behaviour we have been describing, including the distinction between phase changes and nodality. For example, the [V] Stokes parameter of the reflected light will have the opposite sign to that of the incident light if $r_\perp$ and $r_\parallel$ have the same sign, as they do for angles of incidence less than Brewster's angle. Thus the matrix predicts a change of handedness under these circumstances. For angles of incidence greater than Brewster's angle, $r_\perp$ and $r_\parallel$ have opposite signs, and hence the [V] parameters of both incident and reflected light have the same sign - indicating no handedness reversal.
>
> Another interesting prediction of this matrix is that the azimuths of the incident and reflected beams are, in general, different. This is well illustrated by considering the reflection of linearly polarized light at normal incidence, when $r_\perp = r_\parallel = r$. The matrix becomes:

$$R = r^2 \begin{bmatrix} 1 & 0 & 0 & 0 \\ 0 & 1 & 0 & 0 \\ 0 & 0 & -1 & 0 \\ 0 & 0 & 0 & -1 \end{bmatrix}$$

> Application of this matrix to the Stokes vector, $\{[I,Q,U,V]\}$, of the incident light, shows that the reflected light is linearly polarized, but with the opposite sign of [U / Q]. The azimuths of the incident and reflected light are thus not the same."

2.2 Optical polarimetric imaging

<u>Overview</u>

Optical imaging polarimetry is a relatively new measurement technique. Although the required methods and materials have been available for some time, the first demonstrations and applications of optical imaging polarimetry did not appear in literature until the 1970s. This unique research activity is distinguished from the substantial quantity of current studies that utilize <u>non-imaging</u> optical polarimetric techniques, e.g., photopolarimetry; and also the substantial number of current studies that utilize <u>non-optical</u> imaging polarimetric techniques, e.g., polarimetric synthetic aperature radar (SAR).

Initial studies evaluated the feasibility of optical imaging polarimetry in the enhanced discrimination and classification of terrestrial features, in particular, vegetation [Curran, 1981b, 1982; Walraven, 1981; Egan, 1985; Duggin *et al.*, 1989; Egan *et al.*, 1992] and soil moisture [Curran, 1978, 1979, 1980, 1981a; Egan, 1985]. These studies utilized a single 35-mm camera with a linear polarizer that was manually rotated 90° in order to achieve discrimination of the first two Stokes parameters and obtain an estimate of the degree of polarization (Q/I).

Prosch *et al.* [1983] constructed a video imaging polarimeter to study the polarization of solar radiation reflected from the natural environment. The system was composed of three vidicons aligned in parallel, with linear polarizers rotated at 0°, 60°, and 120° relative to the reference plane such that the Stokes parameters I, Q, and U could be measured. The composite color video signal was coded so that deviation

from white would represent increasing polarization; tint specified the azimuth angle of the polarization ellipse whereas hue defined the degree of polarization.

Designs for a spaceborne imaging multispectral polarimeter have been proposed [Egan, 1986]. While a full scale testbed was infeasible, limited spaceborne polarimetric photography experiments were executed onboard six Space Shuttle missions, STS 51A (October 1984) through STS 28 (August 1989) [Coulson *et al*, 1986; Duggin *et al.*, 1989; Egan *et al.*, 1991, 1992]. In these experiments, two 70-mm Hasselblad cameras were aligned in parallel, with linear polarizers (Polaroid HN22) rotated at 0° and 90° relative to a reference plane: only the Stokes parameters I and Q were measured. A significant consideration for accurate measurement was the ability of the mission specialist to align the two-camera system with the mean principal plane of the imaged radiance field. Also, the experiment suffered from the lack of sensitometric calibration, particularly important for a dual camera (hence dual film roll) system. Again, the first two Stokes parameters provided an estimate of the degree of polarization as a simple ratio (Q/I).

Based upon the promising results of the Space Shuttle experiment, the US Army flew a helicopter-borne video polarimeter over various cover types and spanning a range of imaging geometries [Israel, 1991]. In this experiment, a rotating linear polarizer was mounted on a single video camera: each imaged scene collection contained a complete 360° rotation of the polarizer.

Figure 2.2-1 illustrates the execution of the Space Shuttle polarimeter experiment onboard STS 51A. One of the concerns in the evaluation of results was the extent of depolarization created by imaging through the multi-layer laminate shuttle windows [Egan *et al.*,1991].
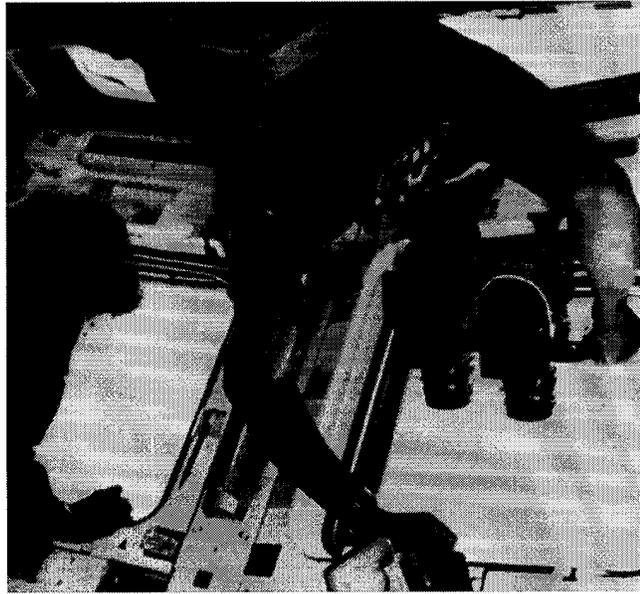
Figure 2.2-1. NASA-JSC photograph 51A-S19-08-008 [from Israel, 1991].

The most current operational imaging polarimeter is the airborne POLDER (POLarization and Directionality of the Earth's Reflectances) instrument, first flown in 1990 under the auspices of the French space agency, l'Centre National d'Etudes Spatiales [Breon & Deschamps, 1993; Deuze *et al.*, 1993; Deschamps *et al.*, 1994]. The stated mission of POLDER is to measure the spectral bi-directional reflectance and polarization of solar radiation reflected by the earth-atmosphere system. The instrument consists of a CCD detector array, a rotating wheel containing 16 filter slots, and a wide-field-of-view telecentric lens system. One slot on the rotating wheel contains an opaque filter for measuring detector dark current, six slots carry unpolarized spectral filters, and nine slots carry polarized spectral filters (three spectral regions with 0°, 60°, and 120°-rotated linear polarizations for each spectral region).

Figure 2.2-2 illustrates the main components of the POLDER instrument.
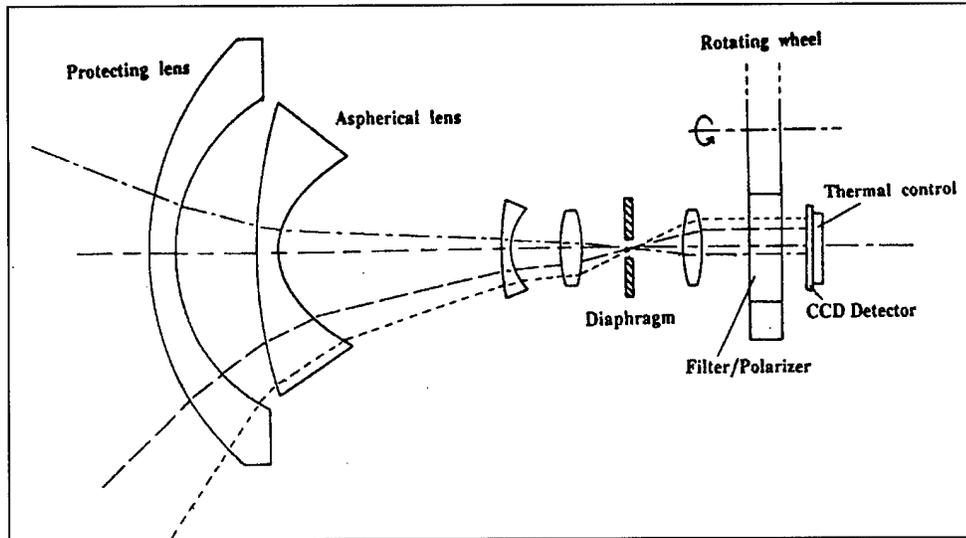
Figure 2.2-2. System design of the POLDER instrument [from Deschamps *et al.*, 1994].

Deschamps *et al.* [1994] describe plans to place a modified POLDER sensor onboard the Japanese ADEOS (Advanced Earth Observing Satellite), scheduled for launch in 1996, in support of the World Climate Research Program (WCRP) and the International Geosphere and Biosphere Program (IGBP). The only other planned spaceborne system capable of measuring global polarized reflectance is the Earth Observing Scanning Polarimeter (EOSP), scheduled for launch in 2003 [Travis, 1992].

In sum, optical polarimetric imaging for remote sensing purposes is a recently emergent technology, with a modest level of investigation to-date compared with the polarimetric studies of active imaging systems, e.g., SAR and LASER.

Review of Walraven [1977, 1981]

A detailed review of Walraven's [1977, 1981] polarimetric imaging technique follows. The main purpose of this review is to present the

28

underlying Stokes parameter derivation, since the current study duplicates much of Walraven's basic approach to Stokes parameter measurement.

An important element of Walraven's and preceeding remote sensing investigations is the deliberate omission of the measurement of the Stokes parameter V, the magnitude of circular polarization. For terrestrial imaging, the V Stokes parameter of the reflected light is two to three orders of magnitude smaller than Q and U, is therefore assumed to be near-zero, and absorbed within the overall system error [Talmage & Curran, 1986]. The simplifying benefit of this omission is that polarimeter design and construction requires the use of linear polarizers only.

The generalized Mueller matrix description for an ideal linear polarizer is of the form:

$$M_\theta = \frac{1}{2} \begin{bmatrix} 1 & \cos 2\theta & \sin 2\theta & 0 \\ \cos 2\theta & \cos^2 2\theta & \cos 2\theta \sin 2\theta & 0 \\ \sin 2\theta & \cos 2\theta \sin 2\theta & \sin^2 2\theta & 0 \\ 0 & 0 & 0 & 0 \end{bmatrix}$$

Equation 2-47

where θ is the angle of rotation of the polarizer with respect to the reference axis. The resulting transformation of an incident Stokes vector by an ideal linear polarizer can then be described by Mueller calculus:

$$S_\theta = M_\theta S_{incident}$$

Equation 2-48

Again, the Mueller calculus is an empirical matrix-based formalism for treating the physical transformation of radiation as described by Stokes vectors; in this case, it treats the effect of transmission through a linear polarizer through premultiplication by the matrix operator M.

Walraven used a single 35-mm camera with a linear polarizer. He exposed four images of each scene, rotating the polarizer for each image at 0°, 45°, 90°, and 135°, respectively. The effective Stokes vector transformation for each of the image collections follows directly from Equations 2-47 and 2-48 for θ values of 0°, 45°, 90°, and 135° applied as arguments to the general Mueller matrix M_θ:

$$S_o = M_0 S_{in} = \frac{1}{2}\begin{bmatrix} 1 & 1 & 0 & 0 \\ 1 & 1 & 0 & 0 \\ 0 & 0 & 0 & 0 \\ 0 & 0 & 0 & 0 \end{bmatrix}\begin{bmatrix} I_{in} \\ Q_{in} \\ U_{in} \\ V_{in} \end{bmatrix} = \frac{1}{2}\begin{bmatrix} I_{in} + Q_{in} \\ I_{in} + Q_{in} \\ 0 \\ 0 \end{bmatrix}$$

Equation 2-49

$$S_{45} = M_{45} S_{in} = \frac{1}{2}\begin{bmatrix} 1 & 0 & 1 & 0 \\ 0 & 0 & 0 & 0 \\ 1 & 0 & 1 & 0 \\ 0 & 0 & 0 & 0 \end{bmatrix}\begin{bmatrix} I_{in} \\ Q_{in} \\ U_{in} \\ V_{in} \end{bmatrix} = \frac{1}{2}\begin{bmatrix} I_{in} + U_{in} \\ 0 \\ I_{in} + U_{in} \\ 0 \end{bmatrix}$$

Equation 2-50

$$S_{9o} = M_{90} S_{in} = \frac{1}{2}\begin{bmatrix} 1 & -1 & 0 & 0 \\ -1 & 1 & 0 & 0 \\ 0 & 0 & 0 & 0 \\ 0 & 0 & 0 & 0 \end{bmatrix}\begin{bmatrix} I_{in} \\ Q_{in} \\ U_{in} \\ V_{in} \end{bmatrix} = \frac{1}{2}\begin{bmatrix} I_{in} - Q_{in} \\ Q_{in} - I_{in} \\ 0 \\ 0 \end{bmatrix}$$

Equation 2-51

and

$$S_{135} = M_{135} S_{in} = \frac{1}{2}\begin{bmatrix} 1 & 0 & -1 & 0 \\ 0 & 0 & 0 & 0 \\ -1 & 0 & 1 & 0 \\ 0 & 0 & 0 & 0 \end{bmatrix}\begin{bmatrix} I_{in} \\ Q_{in} \\ U_{in} \\ V_{in} \end{bmatrix} = \frac{1}{2}\begin{bmatrix} I_{in} - U_{in} \\ 0 \\ U_{in} - I_{in} \\ 0 \end{bmatrix}$$

Equation 2-52

Figure 2.2-3 illustrates the preferred linear polarization state of the transmitted light for each of the four polarizers.
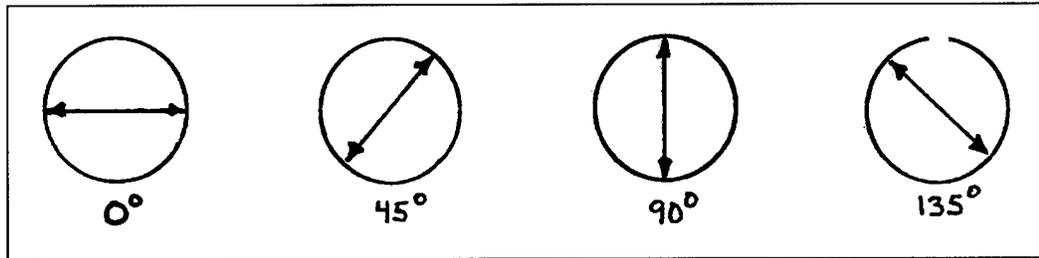
Figure 2.2-3. Schematic representation of the four imaging measurements of the linear polarization state of the incident radiance, after Walraven [1981].

However, since the film records only the intensity I of the filtered radiance, this transformation can be simplified to consider only the effect of polarizer rotation on the first Stokes parameter:

$$I_\theta = \frac{1}{2}\left[I_{in} + (Q_{in}\cos 2\theta) + (U_{in}\sin 2\theta)\right]$$

Equation 2-53

For each of these cases, the intensity of the transformed Stokes vector that is measured on film is:

$$I_0 = \frac{1}{2}\left[I_{in} + Q_{in}\right]$$

Equation 2-54

$$I_{45} = \frac{1}{2}\left[I_{in} + U_{in}\right]$$

Equation 2-55

$$I_{90} = \frac{1}{2}\left[I_{in} - Q_{in}\right]$$

Equation 2-56

and

$$I_{135} = \frac{1}{2}\left[I_{in} - U_{in}\right]$$

Equation 2-57

31

The recovery of the first three parameters of the incident Stokes vector image S_{in} is accomplished through addition and subtraction of the four filtered images:

$$I_{in} = \left[I_0 + I_{90}\right] = \left[I_{45} + I_{135}\right] = \frac{1}{2}\left[I_0 + I_{45} + I_{90} + I_{135}\right]$$

Equation 2-58

$$Q_{in} = \left[I_0 - I_{90}\right]$$

Equation 2-59

and

$$U_{in} = \left[I_{45} - I_{135}\right]$$

Equation 2-60

where

$$S_{in} = \begin{bmatrix} I_{in} \\ Q_{in} \\ U_{in} \\ \approx 0 \end{bmatrix}$$

Equation 2-61

Consistent with Walraven's approach, the current study employs a derivative transformation of the Stokes vector that has a more direct correlation with the physical properties of the imaged features from which the polarized radiance is reflected:

$$S'_{in} = \begin{bmatrix} I_{in} \\ P_{in} \\ \Theta_{in} \\ \varepsilon_{in} \end{bmatrix} \text{, where}$$

Equation 2-62

I_{in} = the irradiance of the incident radiance (unchanged),

P_{in} = the degree of polarization of the incident radiance,

Θ_{in} = the azimuth angle of the polarization ellipse of the incident radiance, and

ε_{in} = the ellipticity angle of the polarization ellipse of the incident radiance.

The definition of these parameters is reprised here from Equations 2-25 through 2-27:

$$P = \frac{\sqrt{Q^2 + U^2 + V^2(\approx 0)}}{I} = \frac{\sqrt{Q^2 + U^2}}{I}$$

<div style="float:right;border:1px solid;padding:4px">Equation 2-63</div>

$$\Theta = \frac{1}{2}\tan^{-1}\frac{U}{Q}$$

<div style="float:right;border:1px solid;padding:4px">Equation 2-64</div>

and

$$\varepsilon = \frac{1}{2}\sin^{-1}\left(\frac{V(\approx 0)}{\sqrt{Q^2 + U^2 + V^2(\approx 0)}}\right) \cong 0$$

<div style="float:right;border:1px solid;padding:4px">Equation 2-65</div>

For linearly polarized light, the polarization ellipse approaches a line segment, with ellipticity (b/a) and ellipticity angle ε both approaching zero.

The four photographic slides from each imaging collection were then digitized into a 512 x 512 pixel array, using a vidicon camera with 8-bit (0-255 grayscale) resolution. The four images were then co-registered and the derivative Stokes parameter images I, P, and Θ were calculated from the application of Equations 2-58 through 2-64.

A significant enhancement of the current study over Walraven's technique is the incorporation of sensitometric co-calibration prior to the calculation of the Stokes parameters. The co-calibration, or joint calibration of the four images to a single common characteristic curve, corrects for the non-linear transformation of light irradiance to emulsion density that is inherent to film, especially in the highest and lowest exposure regions. The effect of this co-calibration is to provide a more accurate estimate of the derived Stokes parameters that are directly calculated from measured irradiance.

2.3 Spatial information content analysis of imagery

Introduction

Within this study, spatial information content analysis refers to those analytic techniques that are applied to the measurement of spatial scene structure - in particular, the measurement of remotely sensed surface structure - through the analysis of their spatial reflected intensity distributions. This unique research activity is distinguished from existing studies that use spatial information content analysis to characterize the performance of imaging systems independent of image content, e.g., optical transfer function (OTF) measurement; and also existing studies that use spatial information content analysis to characterize surface structure under controlled conditions, e.g., LASER scatterometry.

Terrestrial remote sensing of waterwave surfaces

In 1925, Schumacher made simultaneous near-horizontal stereo-pairs from a ship with the intent of measuring the variability of wave heights. The utility of this method was severely limited due to many factors: 1) the camera baseline was restricted to the length of the ship (one camera fore and aft); 2) waves in the foreground obstructed waves in the background; 3) backsides of waves were not visible; and 4) there was a lack of 'ground' control on the open seas for height determination - the errors are especially pronounced from an oblique perspective [Pos,1988]. This experiment represents a limiting case for spatial feature measurement via image analysis.

In 1933, Hulburt [1934] made polarized and unpolarized oblique photographs of sun glitter on sea waves to measure the polarization of light at sea with respect to surface roughness, sun angle, and weather conditions. Because the widths of glitter patterns correlate to the maximum slope of the sea surface, Hulburt was able to demonstrate that waves in the North Atlantic varied from 15° inclination when winds were blowing at 3 knots up to 25° inclination at 18 knots.

Sawyer [1949] mounted a Sonne strip camera on a fast low-flying airplane to photograph narrow strips of the sea surface and measure the directional spectrum of the waves. The field of view was too narrow to capture significant amounts of surface data orthogonal to the flightline. The accuracy of the spectral estimate decreased with the angle from the flightline.

Also in 1949, Barber [1949, 1954] analyzed single photographs of sea surfaces to determine wave direction, but he was unable to determine the two-dimensional spatial spectrum due to the computing limitations of the time.

At this point, it became apparent that an essential requirement for future analysis of spatially correlated surfaces is to have near-nadir, high-resolution, high-contrast images covering large areas. The intent is to photographically capture significant information about the largest range of spatial frequency components without perspective distortion or hidden surface detail. It also became apparent that the analysis of large amounts of spatial information would require the forthcoming capabilities of the digital computer.

In 1951, Cox and Munk [1954a, b] measured the wave-slope distributions of the sea surface from aerial photographs of sun glitter patterns. They computed the distribution from the measured variation of radiance within a glitter pattern instead of computing maxima from the pattern boundaries as done by Hulburt. Four cameras were flown from a single airplane at altitudes of 2000 feet, with two used as imagers and two used as radiometers. Their image analysis was quite sophisticated; it accounted for sun diameter, angular reflectivity, lens falloff (vignetting), film sensitivity, exposure calibration (sensitometry), and ultimately provided a first-order relationship between film density and directional wave-slope probability.

In 1953, Schooley [1954] performed a simplified version of the Cox & Munk experiment by taking flash photographs of a river surface from a 45-foot bridge elevation at night. The main limitation of his experiment was the probable inhomogeneity of the water surface due to limited fetch (the surface area where waterwaves are being generated by the wind) and the presence of wave-refracting obstacles in the water.

In 1954, medium-altitude (3000 feet) stereophotography was employed by Marks and Ronne [1955] to generate stereopairs of sea surfaces. Two airplanes carried radio-synchronized cameras and a surface ship acted as 'ground' control in the photographs. Elevations were photogrammetrically measured at discrete points and the sampled elevation array was then autocorrelated (the sampling distance determined the desired spatial resolution). This experiment marks the first recorded use of a digital computer to calculate the two-dimensional spectra of waterwaves. The work of Cote et al. [1960] enhanced this basic technique. More recent stereophotogrammetric efforts include Holthuijsen [1983a, b] and Pos et al. [1988]. Elements of this later work include

37

methods to render the water opaque so that a more exact calculation of the height field can be made.

During the 1950s and early 1960s, Longuet-Higgins [1952-1962; Cartwright & Longuet-Higgggins,1956] elaborated on the results of Cox and Munk to formulate the statistical theory of patterns, paths, number, frequency, and distributions of specular reflection points on randomly moving surfaces. Stilwell [1969; Stilwell & Pilon, 1974] correlated the statistics of sea-surface images to the wave-slope statistics of the actual sea surface. Under the assumptions of uniform sky radiance, optimized viewing geometry, and small surface slopes, Stilwell derived the relationship between the film transmittance of an imaged surface point and the range component of the wave slope at that surface point. He further demonstrated a 'linearizable' relationship between the spatial image spectrum and the imaged surface slope spectrum. Kasevitch [1975] extended Stilwell's model to second order to develop an optimization criterion for the relationship. Chapman and Irani [1981] took this work one step further by creating a synthetic model and executing a limited quantification of the error magnitudes associated with the parametric dependence of this linear model. North [1989] enhanced Chapman and Irani's model to consider sub-resolution wave slopes and then executed a more comprehensive parametric surface exploration.

Sheres [1980, 1981] developed a novel technique for remotely sensing surface-flow velocities based on imagery of monochromatic wavetrains of known frequency (such as those generated by a motor boat) propagating over the region of interest. His work demonstrated that the wavelength and direction of two wavetrains provided all the information required to calculate surface flows. Gotwols and Irani [1980] developed a similar technique to determine the phase velocity of short gravity waves.

Exotic sensors using LASER [Palm *et al.*, 1977; Schau, 1978; Abshire & McGarry, 1987] and LIDAR [Weinman, 1988] have been used to extract directional spectra and surface backscatter data at higher wavenumbers (i.e., the capillary wave regime). Synthetic Aperture Radar (SAR) imagery has been used to estimate spectra, phase velocities, and propagation directions at lower wavenumbers (i.e., the gravity wave regime) [Monaldo & Lyzenga, 1986; Monaldo & Kasevich, 1982; Carlson, 1984]. Also, Long Wave Infrared (LWIR) sensors have been used to calculate spatial spectra of ocean-surface temperature [Saunders, 1967, 1968; McLeish, 1970].

Lybanon [1985] reported on the implementation of an automated image-analysis system by the U.S. Naval Ocean Research and Development Activity (NORDA, now the Naval Research Laboratory or NRL). The Interactive Digital Satellite Image Processing System (IDSIPS) can automatically derive the sea-surface slope statistics from sun glitter images through analysis of the imaging geometry. As a late practical example, Fisher [1986] analyzed four sun glitter images taken from the space shuttle Challenger (STS-41G) to locate acoustically important oceanographic features in support of hydro-acoustical sensor placement.

Breon and Deschamps [1993] described the use of the POLDER (Polarization and Directionality of the Earth Reflectance) instrument to derive ocean wave slope distributions from polarized directional specular reflectance measurements. Inversion of an analytical model against their data accurately fit (< 1.2%) all spectral and angular reflectance variations observed with the POLDER sensor. These observations included a large reflectance asymmetry relative to the principal plane that they correlated with anisotropic wave slope distribution created by directional wind stress.

Spatial spectrum analysis of correlated scenes

A comprehensive review would include the work of Stillwell and Pilon [1974], and Kasevich *et al.* [1971, 1972]. The emphasis of this earlier work is on the analysis of coherent optical processing techniques as applied to photographic emulsions of spatially correlated scenes. Kasevich [1975] provides a general introduction to the first-order theory subsequent to the development of an geometric-optics-approximation second-order theory that estimates the optimum viewing geometry for obtaining reasonable spectra. Stillwell [1969] provides additional development of optical imaging theory subsequent to performing an optical analysis to derive two-dimensional spectra.

Review of Kasevich [1975]

The essential requirement for the determination of spectra from spatially correlated scenes (in this case, waterwave scenes) is to have the spatial modulation of the imaged scene be proportional to the surface profile. Kasevich uses the example of a transparency with film exposure, E, defined over its linear region by

$$E(y) = f_0(y)^{-\gamma/2} \left[\frac{1 + f(y)}{f_0(y)} \right]^{-\gamma/2} \qquad \text{Equation 2-66}$$

where

$$E(y) = f_0(y) + f(y) \qquad \text{Equation 2-67}$$

and

γ = the film gamma

such that

$f_0(y)$ = the mean exposure on film

and

$f(y)$ = the exposure modulation due to scattering of radiance from specular wave-slope facets.

This example is given for the one-dimensional case.

If $f_0(y) >> f(y)$, then Equation 2-66 can be expanded in a binomial series to yield the approximation

$$E(y) \cong f_0(y)^{-\gamma/2}\left[1 - \left(\frac{\gamma}{2}\right)\left(\frac{f(y)}{f_0(y)}\right)\right]$$

Equation 2-68

The estimation of the slope spectrum from the forward Fourier transform of the image requires that f(y) be linear with respect to the wave slope *dz/dy*, where z is the surface elevation. This condition can only be approximately satisfied for waterwave surfaces because of the non-linearity of 1) the spatial radiance distributions found in nature, 2) the Fresnel reflectivity variation with respect to incidence angle, and 3) the refraction of upwelling subsurface radiance in the direction of the observer.

41

Review of Stillwell [1969]

For a small wave-slope angle β, the small angle approximation is:

$$\beta = \tan^{-1}\left[\frac{dz}{dy}\right] \cong \frac{dz}{dy}$$

<div style="text-align: right;">Equation 2-69</div>

where β is the fundamental parameter for extracting wave-slope spectra from imagery. The reflected radiance observed at azimuth angle θ is a simple function of Fresnel reflectivity and incident radiance:

$$L_0(\theta, \beta, \omega) = L(\mu) R(\omega)$$

<div style="text-align: right;">Equation 2-70</div>

where

$L_0(\theta, \beta, \omega)$ = the observed reflected radiance,

$L(\mu)$ = the incident radiance to be reflected,

$R(\omega)$ = the Fresnel reflectivity (for any arbitrary polarization),

θ = the zenith angle of observation,

β = the slope of the reflecting surface facet,

μ = the zenith angle of the incident radiance,

and

ω = the angle of incidence,

such that

$$\omega = \theta - \beta$$

Equation 2-71

and

$$\mu = \omega - \beta$$

Equation 2-72

Figure 2.3-1 illustrates the angular relations for the one-dimensional case.
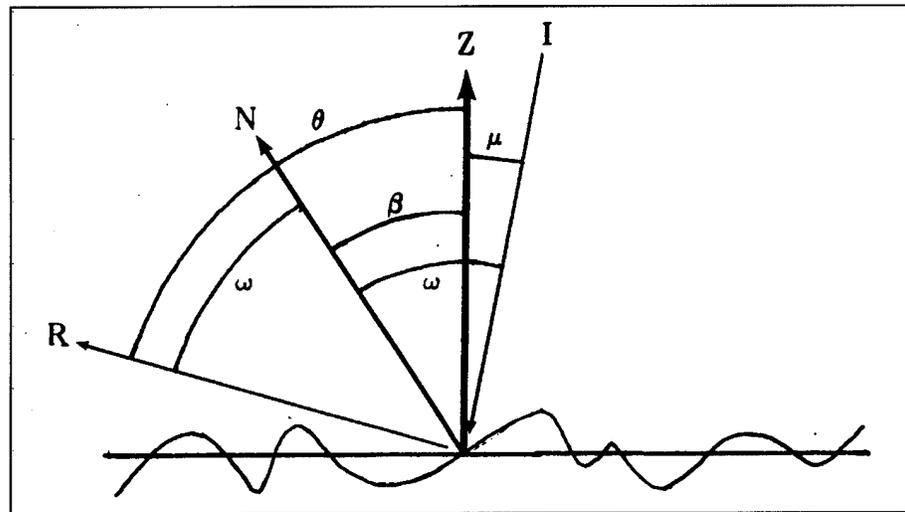
Figure 2.3-1. One-dimensional angle relationships [from North, 1989].

The variation of observed radiance with respect to a change of surface slope $d\beta$ at some point is

$$\frac{dL(\theta)}{d\beta} = \left[\frac{dL(\mu)}{d\mu}\right](R(\omega))\left[\frac{d\mu}{d\beta}\right] + (L(\mu))\left[\frac{dR(\omega)}{d\omega}\right]\left[\frac{d\omega}{d\beta}\right]$$

Equation 2-73

If β is a small angle and $\omega \cong \mu$, then

$$\frac{dL(\theta)}{d\beta} = [L'(\mu) R(\omega) + L(\mu) R'(\omega)]\frac{d\omega}{d\beta} , \qquad \boxed{\text{Equation 2-74}}$$

where the prime (') denotes the first derivative with respect to the argument.

With the assumption that the water surface remains analytic (i.e., infinitely differentiable), the small-angle linear approximation holds in the Fourier transform for waveslope angles (β) up to at least 30°.

3.0   Methods and Materials

The full description of methods and materials comprises four sections, one for each of the four phases of this study:

Image Data Collection - This section describes the design and construction of an imaging polarimeter system and the execution of both in-field and aerial image data collections.

Image Data Processing - This section describes the post-collection processing of the image data: film development, image digitization, digital image data manipulation, and production of Stokes imagery.

Image Data Simulation - This section describes the model that was used to simulate Stokes imagery of the reflected, polarized skydome under clear sky conditions - as a basis for comparison with an image subset from the in-field data collection.

Image Data Analysis - This section describes the analytic techniques that were applied to the Stokes imagery, to include two-dimensional fast Fourier transformation (FFT) of selected subimages.

In addition, the source code developed in this study for the image data simulation is found in Appendix A.

3.1 Image Data Collection

3.1.1 General

<u>Construction of the imaging polarimeter</u>

A filter mount was constructed to fit over the 30-mm four-lens system of a Nishika N8000 3-D camera. Four small (18.5 mm x 18.5 mm) square sections were cut from the same sheet of Polaroid HN38 linear polarizer such that the transmission axes of first filter pair are rotated $0°$ and $90°$ about the optic axis with respect to a common reference plane; and that the transmission axes of the second filter pair are rotated $45°$ and $135°$ about the optic axis with respect to the same reference plane. The four filter squares were aligned in the mount, secured in place, and the full assembly was then fitted over the four-lens system and secured. If the four small filter squares were cut perfectly, the abutment of their edges against each other and against the interior edge of the mount would ensure rotational alignment of the linear polarizers.

Figure 3.1-1 illustrates the resulting imaging polarimeter system. The mount containing the four rotated linear filters lies between the camera and two samples of Polaroid HN38 linear sheet polarizer.

<u>Alignment of the imaging polarimeter</u>

A key assumption is that the optic
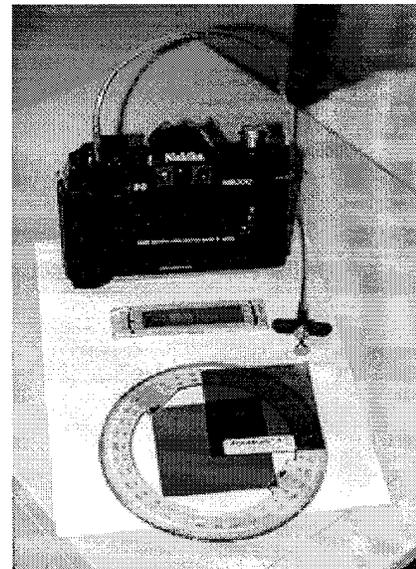
Figure 3.1-1. Imaging Polarimeter.

46

axes in the four-lens system are all in parallel; by definition, the common reference plane for filter rotation contains these four optic axes. Another key assumption is that the transmission axis of the HN38 polarizer is in parallel with the specified edge of the manufacturer-supplied square sheet, since all subsequent cuts along the parallel, diagonal, and perpendicular were made relative to this specified edge. A test was performed with the intent to verify the second assumption and to align the four filters to their proper rotations relative to the common reference plane.

The filter mount assembly was placed over a diffuse, unpolarized illumination source. A second HN38 square sheet was mounted over a protractor (refer to Figure 3.1-1) with the corners fixed at the four ordinates. The sheet was rotated until a relative minimum transmission (maximum absorption) via cross-polarization was detected with a light meter for each of the four filters. For each rotation, the angle on the protractor was measured to within 0.5 degree. This process was repeated three times and the measurements then averaged and examined for bias. The standard error was within the measurement accuracy; no rotational bias was detectable for any of the four filters within the measurement accuracy of this test.

Figures 3.1-2 through 5 illustrate the alignment process for each of the four filters. These figures also serve as a simple demonstration of the law of Malus: transmission of light through the two overlapping linear sheet polarizers is proportional to the square of the cosine of the angle between their principal axes of transmission.
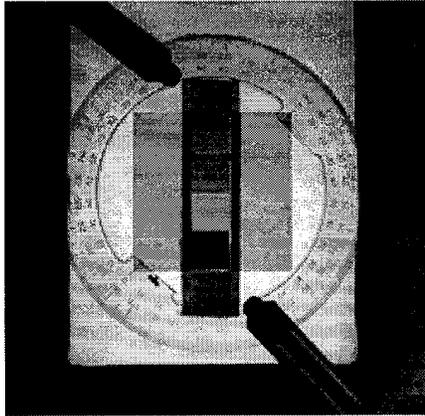
Figure 3.1-2. Cross-polarized 0° filter (bottom filter).
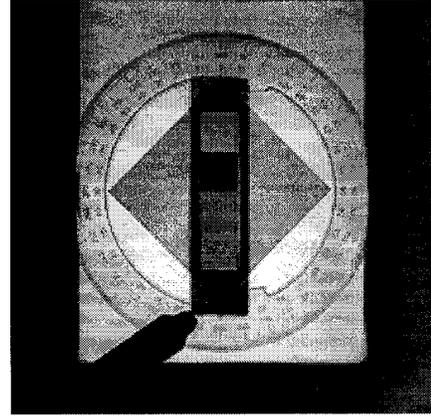
Figure 3.1-3. Cross-polarized 45° filter (second filter from top).
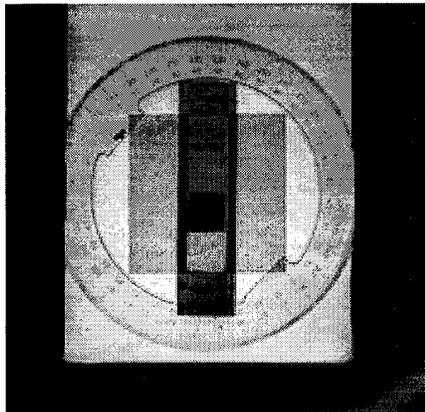
Figure 3.1-4. Cross-polarized 90° filter (second filter from bottom).
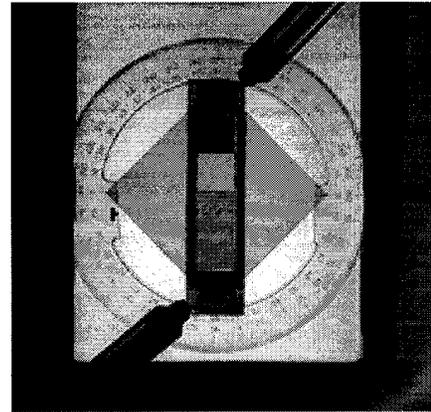
Figure 3.1-5. Cross-polarized 135° filter (top filter).

<u>Film calibration</u>

One type of film was used for the entire data collection: 36-exposure Kodak Gold 200-speed color negative film. This film was bulk purchased from a single vendor; and, the cartons were inspected to ensure that the film rolls had the same manufacturing lot number.

A sensitometric 24-step wedge was exposed on the leading edge of each film roll with a Joyce-Gevaert type 2L sensitometer. A frame mask overlay was created that would simulate the frame placement of the Nashika camera and yet include coverage of all 24 exposure steps. The

48

intent of this mask was to support digital image transfer of the full step wedge during photo CD processing.

3.1.2 In-field imaging

<u>Overview</u>

The intent of in-field imaging was to collect polarimetric data on a set of controlled test surfaces under natural illumination conditions: in this experiment, under polarized clear sky radiance. The camera orientation was fixed with respect to solar azimuth, the test surfaces were rotated through four discrete angles, and images were collected at four distinct solar elevations.

<u>Construction of the in-field test stand</u>

A test stand was constructed for the purpose of fixing the imaging polarimeter over a set of test surfaces in the field.

Figure 3.1-6 illustrates the full setup of the in-field test stand (under less than ideal illumination conditions).

Figure 3.1-6. Setup of the test stand.

A 4x8 foot (122x244 cm) plywood sheet served as the base of the test stand. Four 10-foot (3.05 m) sections of electrical conduit formed the legs. A plastic flange provided a rigid camera mount at the apex of the test stand. The resulting effective focal distance between the camera system aperture and the test stand base is nine feet (2.74 m). This distance provided reasonable

mitigation of the parallax effects created by the finite separation of the four lenses (55 mm between the two most distant lens centers).

Figure 3.1-7 shows the alignment of the imaging polarimeter over the in-field test stand.
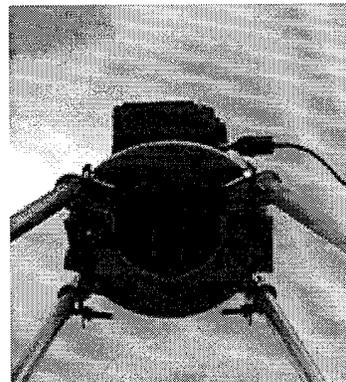
Figure 3.1-7. Alignment of the imaging polarimeter on the in-field test stand.

Construction of the test surface panels

Two identical 2x4 foot (61x122 cm) lighting diffuser panels were used as test surface panels. The unique feature of these panels is their 'cracked ice' pseudo-random texture, which ensures a high degree of spatial correlation. To ensure that the experiment contained at least one surface that was within the linear range of the characteristic curves, one panel was coated with chrome aluminum spray paint and the other was coated with gray primer. The two panels were mounted on a 4x4 foot (122x122 cm) plywood sheet with white thumbtacks, which also served as in-scene ground control points during image co-registration. The entire assembly was then mounted on the center of the test stand with a single bolt through the center of both plywood sheets. This mounting strategy allowed for 360° rotation of the test surface panels in relation to the fixed reference plane of the imaging polarimeter.

Other test stand features

An 18-inch (45.7 cm) back-surfaced acrylic hemispherical security mirror was used to reflect a polar representation of the complete skydome at the beginning of each collection. A 20-foot air-driven shutter release was employed to minimize in-scene obscuration of the sky radiance by

the photographer. A 5.5-inch (14 cm) vertical post was mounted on the front (sun-facing) edge of the base in order to cast a linear shadow that could support test stand alignment with the changing solar azimuth. Finally, a Kodak 10-step gray scale, 8-step color control patch, and neutral density card was included in each image collection to support in-scene secondary calibration.

Figure 3.1-8 illustrates the two base-mounted test panels and the several test stand features.
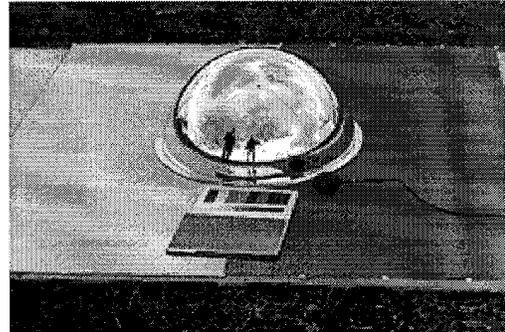
Figure 3.1-8. In-field test panels and supporting test stand features.

Mission planning for the in-field collection

A key requirement for optimal in-field data collection was to obtain clear sky illumination during the collection period, nominally a four-hour window that would either begin or end at solar noon.

Hourly visible and infrared weather satellite (GOES) imagery was available from a University of Illinois (Champaign-Urbana) database hosted on the Internet. Based on a one-week forecast of regional high pressure fronts during the first days of November 1994, this satellite imagery was downloaded in support of near-term prediction of an optimal collection window for the in-field test. Weather images from the early morning of 07 Nov 94 indicated that such a collection window would exist over Syracuse NY for the entire daylight period. The in-field collection was subsequently scheduled to begin at solar noon, approximately 1155 EST. The intent was to provide the largest range of solar elevations beginning with the maximum elevation at solar noon and the minimum at sunset.
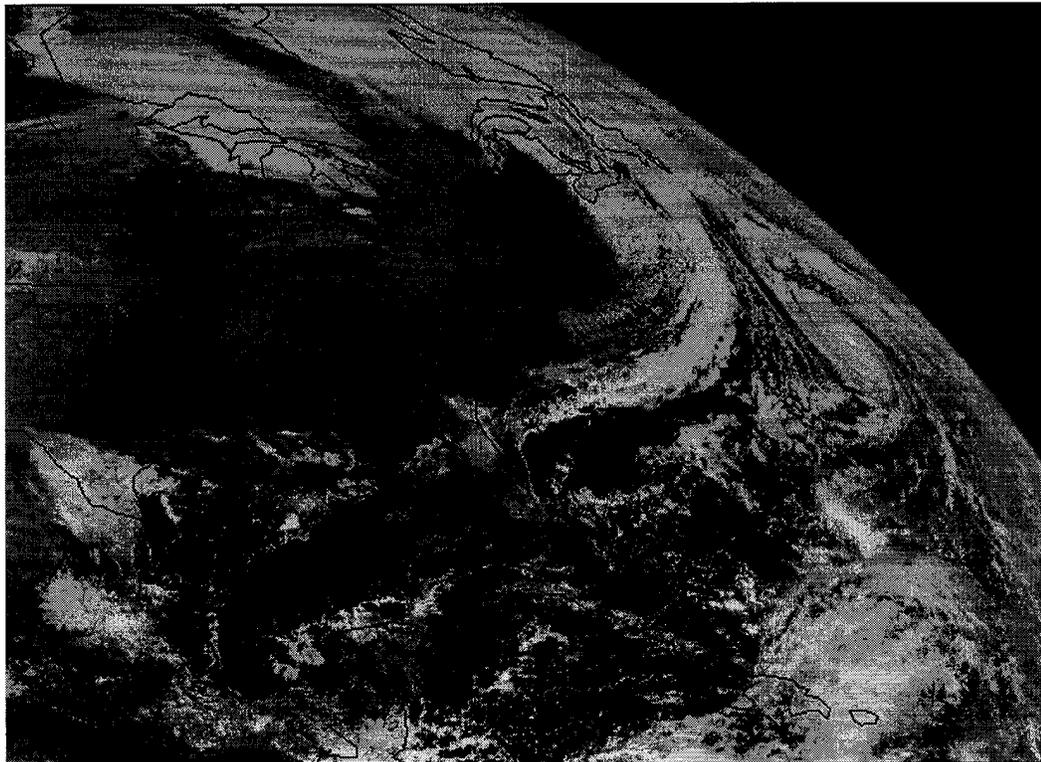
Univ of Illinois, Urbana/Champaign – Dept of Atmospheric Sciences   Mon, Nov 07, 11AM CST 94110717Z

Figure 3.1-9. Visible satellite image, 1200 Eastern Standard Time.
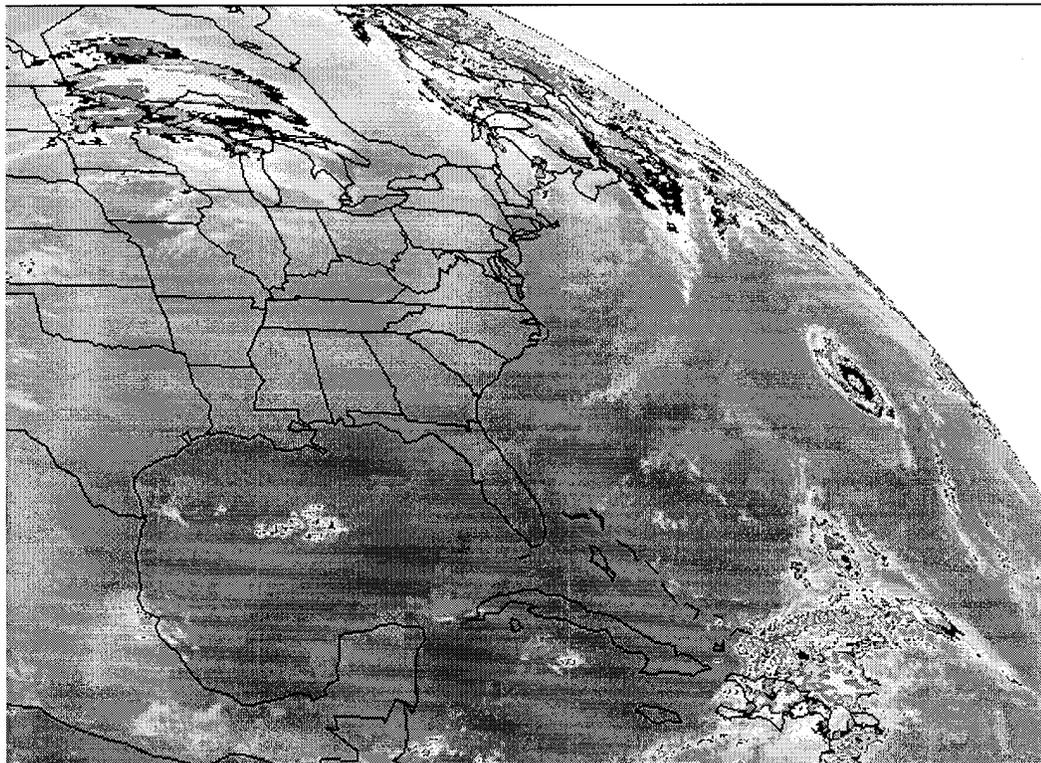
Univ of Illinois, Urbana/Champaign – Dept of Atmospheric Sciences   Mon, Nov 07, 07AM CST 94110713Z

Figure 3.1-10. Infrared satellite image, 0800 Eastern Standard Time.

Figures 3.1-9 and 10 illustrate the presence of a high-pressure front with cloud-free skies over the Syracuse NY area on 07 November 1994. (Note the large tropical storm over the Atlantic.)

Execution

In-field polarized photographs were taken on a near-cloudless day, 07 Nov 94, near the Skytop parking lot on the Syracuse University NY campus. This location afforded nearly horizon-to-horizon visibility at most azimuths. Six sets of photographs were taken over a six-hour period, beginning one hour before solar noon and then at subsequent one-hour intervals. The entire platform was rotated slightly for each collection so that the polarimeter reference plane remained parallel with the principal plane: a plane containing the sun and a vertical line running through the base center, the polarimeter, and local zenith. The shadow cast by the small vertical post mounted on the platform was used to maintain this alignment. The length of the post shadow was also used to provide an in-scene secondary measurement of solar elevation.

Each of the six datasets consisted of five collections. For the first collection, the dome mirror was placed over the center of the test stand base. The resulting collection provided a nearly complete image of the full skydome reflecting off the mirror and onto the four focal planes of the overhead polarimeter.

Figure 3.1-11 illustrates the first test scene, containing a dome mirror, that was collected for each of the four datasets. Note the substantial cloud cover that is apparent in the skydome reflection, indicative of an earlier unsuccessful collection attempt that was not included in the data analysis or results.
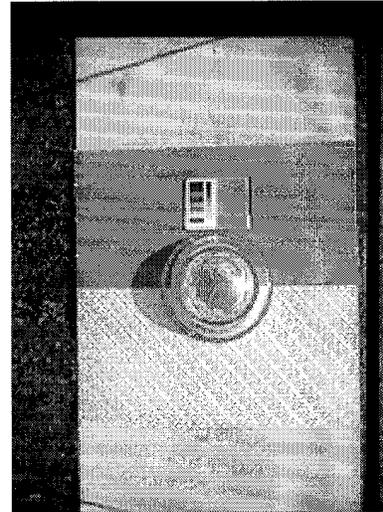
Figure 3.1-11. Test scene 1.

For the remaining four collections, the test panels were rotated 0°, 45°, 90°, and 135° with respect to the defined reference plane. The intent of this rotation was to vary the illumination geometry of the scene relative to the test target, an effect which would normally be difficult (if not impossible) to achieve with most natural scene contents in the terrestrial environment (e.g., a forest or lake).

Figures 3.1-12 through 15 illustrate examples of the four remaining test scenes that were collected for each of the four datasets. The test panels were succesively rotated counterclockwise 45° for each collection: test scene 2 is at 0° rotation, scene 3 is at 135°, scene 4 is at 90°, and scene 5 is at 45°. These examples are taken from the first image in each of the quad series, i.e., the quad image with the polarizer rotated 90° from the reference plane.
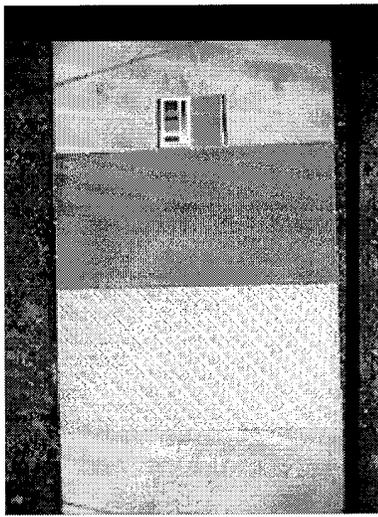
Figure 3.1-12. Test scene 2.
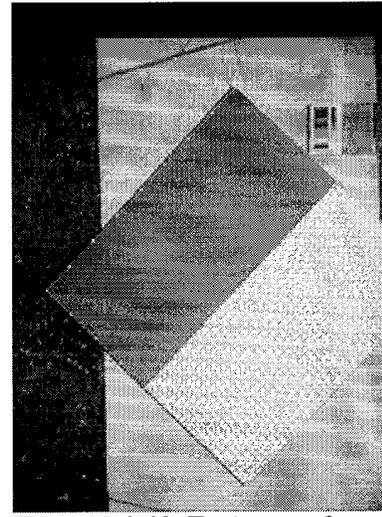
Figure 3.1-13. Test scene 3.
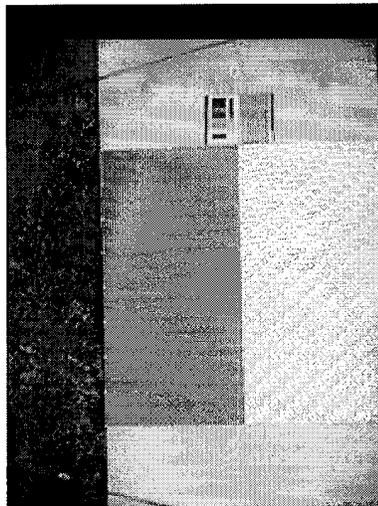
Figure 3.1-14. Test scene 4.
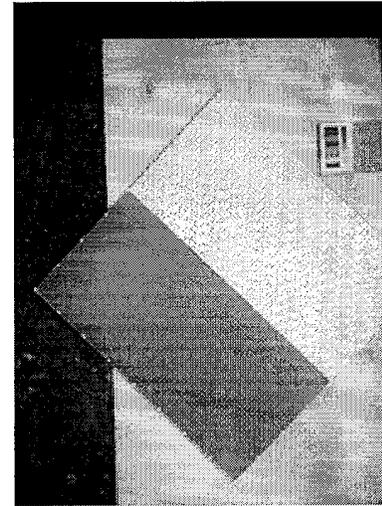
Figure 3.1-15. Test scene 5.

3.1.3 Aerial Imaging

Overview

  The intent of aerial imaging was to collect polarimetric data under clear skies of large natural surface features containing resolvable

homogeneous texture, in particular, the waterwave surface of the Hinckley reservoir near Marcy NY. Other features of possible future research interest would be collected as targets of opportunity. Because of the relative lack of control of the collection geometry, compared with the in-field test, much of the subsequent data analysis would qualify this collection as a demonstration.

Mission planning for the aerial collection

The opportunity to collect aerial polarimetric imagery presented itself with a short timetable. The flight was scheduled for 03 November 1994 based on 24-hour weather information: sunny, lightly scattered clouds, and light winds. Two missions would be flown, one occuring close to solar noon and the other approximately two hours later.

Description of the flight platform

A Cessna Skyhawk single-engine airplane was rented from Landcare Aviation, Inc., located at the Marcy NY regional airport. The aircraft had two inspection ports in the aft underbelly of the fuselage, both available for use as camera viewports. The imaging polarimeter was mounted over one of the viewports and aligned with its reference plane roughly parallel with the flightline; in lieu of a rigid mounting frame, the polarimeter was cradled on an exposed area of the aircraft's foam rubber insulation. The aircraft's on-board magnetic compass and altimeter provided the only indications of camera azimuth and elevation.

Figures 3.1-16 through 18 show the aircraft used for the aerial data collection, indications of the weather and illumination conditions, and the location of the polarimeter in the aircraft.
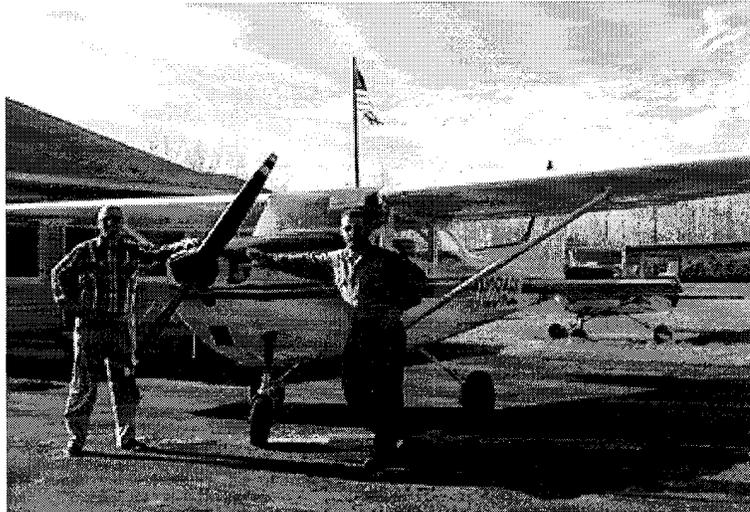
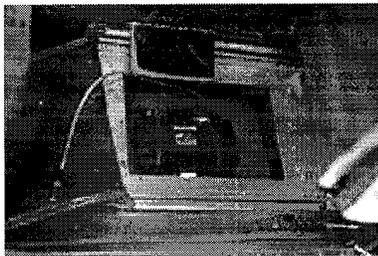**Figure 3.1-16**. L-R: photographer, flight platform, and pilot.

Figure 3.1-17. Interior view of polarimeter placement.
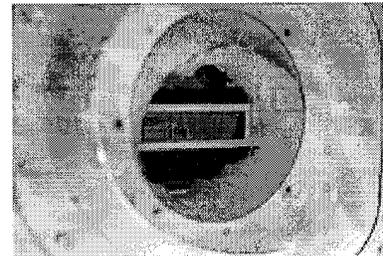

Figure 3.1-18. Exterior view of polarimeter placement.

Execution

  The primary imaging target for both missions was the water surface of the Hinckley reservoir, located approximately 10 miles NNE of the Marcy NY airport and four miles ESE of Griffiss Air Force Base near Rome NY. Three passes of the reservoir were made at three different flying heights: approximately 1000, 500, and 150 feet above the water surface. During the return leg of both flights, targets of opportunity were also collected: farm fields, tree stands, rural buildings, *et cetera*.

Figure 3.1-19. Subset of the USGS quadrangle containing the Hinckley reservoir.

For the first mission, 10 aerial images were collected during the interval 1312 -1327: two images were collected for each of the three overflights of the reservoir and four images were collected of opportunistic targets. For the second mission, 10 aerial images were collected during the interval 1530 - 1548: again, two images were collected for each of the

three overflights of the reservoir and another four images were collected of opportunistic targets.

Figure 3.1-20. Aerial view of the Hinckley reservoir.

3.2 Image Data Processing

<u>Film development and image digitization</u>

The film was turned over to a commercial vendor for standard KODAK film development and direct Photo CD™ processing. Special processing instructions included requests to turn off the automatic color balance control, to scan in the step wedge, and to center the two pairs of images within two standard 35-mm frames - since the dimensions of each photo pair are approximately 22 mm x 37 mm. The standard Photo CD™ process converts a normal 35 mm frame (24 mm x 36 mm) into a 2048 x 3076 pixel image at a scanning resolution of approximately 11.7 microns x 11.7 microns. As a result, one millimeter of exposed film from each frame was not scanned, but two millimeters of unexposed film were scanned.

Figures 3.2-1 and 2 illustrate a complete photo 'quad' for one data collection. Note that each cross-polarized pair exists as two subimages that occupy the same 35-mm image frame; the two 35-mm frames that form each quad are sequential on the roll of film. Also note the two mm of unexposed film on the upper edge of the frame and the unexposed vertical band that separates the two subimages; the one mm of exposed but unscanned film is, for obvious reasons, missing from the left and right edges of the digitized image frames.
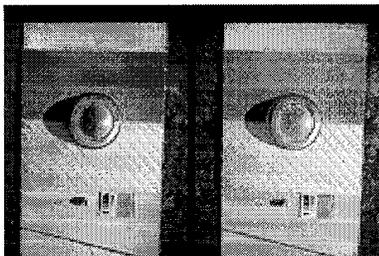
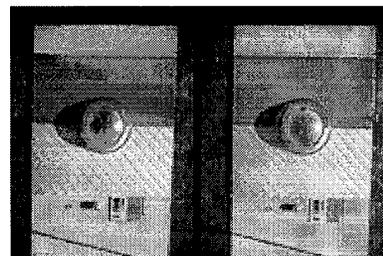**Figure 3.2-1**. 90° and 0° polarized image pair.

Figure 3.2-2. 135° and 45° polarized image pair.

Creation of the digital image quads

Each Photo CD[TM] compact disk was mounted on a Compudyne 486 DX2 computer system operating in a Windows[TM] environment. The commercial software program ADAPTEC Magic Lantern[TM] was used to ingest each image pair, crop the pair to create two separate digital images, and then convert each image into a Tagged Image Format (TIF) file for transfer to a 1-gigabyte hard disk drive. Each dataset, comprising four uncompressed 3-color TIF files, occupied almost 38 megabytes of hard disk space; the 80 TIF files generated by the in-field collection required almost 756 megabytes.

The software program NOVASTOR Novatar[TM] was used to copy all TIF files from the Compudyne hard disk drive to 8-mm data tape. The files were put into a TAR format acceptable to a SUN UNIX[TM] environment.

Co-registration of the digital image quads

The software program SRI Environment for Visualizing Images (ENVI[TM]) was used for the remainder of the data processing. It was hosted on a SUN Sparc[TM] 2 workstation operating in a UNIX[TM] environment. All computer systems and software utilized in this study are part of the FIRS[1] cluster located in Bray Hall on the SUNY ESF campus.

---

[1] Facility for Image Processing & Remote Sensing at SUNY ESF

Figure 3.2-3 illustrates the SUN workstation configuration that was utilized for the majority of the digital image processing.
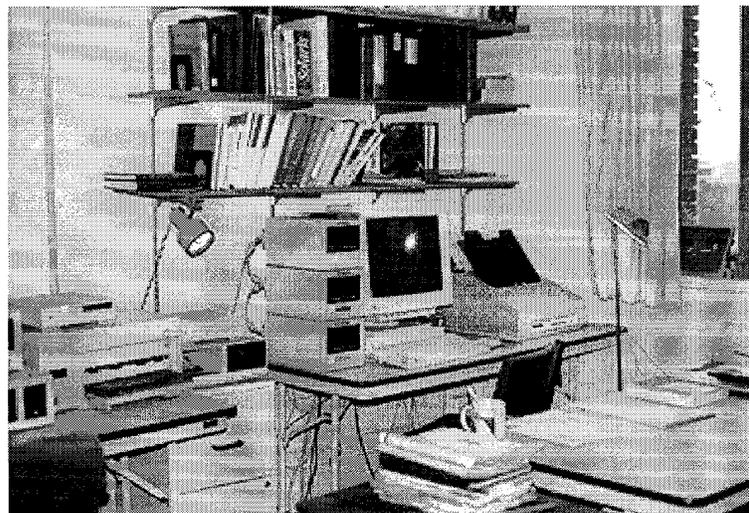

Figure 3.2-3. SUN workstation and peripherals at the FIRS.

The four images from each collection were co-registered, using in-scene markers (thumbtacks) as common ground control points and then selecting a first-order, four-point (rotation, scaling, & translation) solution within ENVI. Due to the close imaging geometries of the four images, co-registration was predominantly a simple translation of image coordinates: standard errors of less than 0.30 pixel were readily achievable.

Creation of the Stokes images and Stokes derivative images

Using the ENVI Band Math option, the co-registered images were mathematically combined to form the Stokes parameter images:

I =   [Img(0°) + Img (45°) + Img(90°) + Img(135°)] / 2 | Equation 3-1 |

Q =   [Img(0°) - Img(90°)] | Equation 3-2 |

U =   [Img(45°) - Img(135°)] | Equation 3-3 |

The Stokes parameter images were then mathematically combined to form the Stokes derivative images, P, the percentage polarization, and T, the orientation angle of the polarization ellipse:

$$P = \left(\frac{\sqrt{Q^2 + U^2}}{I} \right) * 100 \, [\%] \qquad \text{, and}$$

$$T = \left(\frac{1}{2} * \tan^{-1} \frac{U}{Q} \right) * \frac{180}{\pi} \, [\text{deg}]$$

Also, since the sum of each orthogonally polarized image pair represents an estimate of the unpolarized intensity image (I), the histogram statistics of the difference of the two sums were calculated in order to provide a system calibration check. If the system was perfectly calibrated, the difference image, D, should be everywhere zero:

$$D = I' - I'' = [Img(0°) + Img(90°)] - [Img(45°) + Img(135°)]$$

Other derivative images were also calculated:

IN = the difference between the maximum image digital count and I (effectively, a digital negative),

$$IN = 510 - I$$

PN = the percent depolarization,

$$PN = 100 - P \, [\%]$$

TC = the 90° complement of T,

$$TC = \frac{180}{\pi} * \left(\tan^{-1}\left(\tan\left((T + 90^{o}) \Big/ \left(\frac{\pi}{180}\right)\right)\right)\right) \text{[deg]}$$ Equation 3-9

Also, the 45° and 135° complements of T were calculated for subsets of the in-field collection images:

TB = the 45° complement of T,

$$TB = \frac{180}{\pi} * \left(\tan^{-1}\left(\tan\left((T + 45^{o}) \Big/ \left(\frac{\pi}{180}\right)\right)\right)\right) \text{[deg]}$$ Equation 3-10

and

TD = the 135° complement of T,

$$TD = \frac{180}{\pi} * \left(\tan^{-1}\left(\tan\left((T + 135^{o}) \Big/ \left(\frac{\pi}{180}\right)\right)\right)\right) \text{[deg]}$$ Equation 3-11

Based on considerations elaborated in Chapters 1 and 2, only the red color band of the three spectral bands was processed and retained for image data analysis. One additional consideration that came to light during image processing was the data limit imposed by the 64-megabyte capacity of the workstation's random access memory (RAM). The first six equations in the preceeding section were used to process each full co-registered image quad, creating an effective six-image real array with nominal dimensions:

6 images x (1400 x 1850) pixels/image x 4 bytes/pixel = 62,160,000 bytes.

However, this array represents a single color band. While ENVI provides for several options which store image bands on disk versus RAM, it became apparent that the logistics of creating one-band image files and then aggregating multiple one-band image files into single multiband image files would be impractical for large numbers of three-color-band quad images - effectively, images containing 12 co-registered bands.

3.3 Image Data Simulation

A synthetic imaging model was created to simulate Stokes imagery of the reflected, polarized skydome under clear sky conditions to compare with the first scene of each of the four datasets of the in-field test (refer to Figure 3.1-11). This section describes the composition of the image data simulation.

In addition, the FORTRAN source code that was developed in this study for the simulation is listed in Appendix A. The code is written in Microsoft FORTRAN for Windows™; the executable files run under MS Windows™.

<u>Calculation of clear sky radiance</u>

A typical clear skydome radiance distribution is the CIE model [CIE, 1973]:

$$L_{sky}(\theta,\phi) = L_{ref}\frac{AB}{C}$$

Equation 3-12

where

$$A = 0.91 + 10e^{-3\mu} + 0.45\cos^2\mu$$

Equation 3-13

$$B = 1 - e^{-0.32/\cos\theta}$$

Equation 3-14

and

$$C = 0.274(0.91 + 10e^{-3\theta_0}) + 0.45\cos^2\theta_0$$

Equation 3-15

66

such that

θ = the zenith angle to a sky element,

φ = the azimuth angle to a sky element,

μ = the angle from the sun center to a sky element,

$$\mu = \cos^{-1}[\cos\theta_0 \cos\theta + \sin\theta_0 \sin\theta \cos(\varphi - \phi_0)]$$

Equation 3-16

θ_0 = the zenith angle to the sun center, and

φ_0 = the azimuth angle to the sun center.

Although the CIE model provides broadband spectral radiance values, results from this model must be used with caution when applied to narrowband spectral radiance, particularly in the vicinity of the solar spectral radiance peak at 460 nanometers.

Calculation of clear sky polarization

The direct radiance from the sun is fully unpolarized. However, the fraction of unpolarized solar radiance that becomes partially polarized by atmospheric Rayleigh scattering can be described by the function:

$$p = 0.94\left(\frac{1 - \cos^2\mu}{1 + \cos^2\mu}\right)$$

Equation 3-17

This function accounts for multiplicative depolarization created by the anisotropy of atmospheric scatterers [Coulson,1975]: in this model, fractional polarization varies from 0 (unpolarized) in the vicinity of the sun to .94 (94% polarized) at the anti-solar point.

Calculation of the azimuth angle of the polarization ellipse

The direction of polarization is always normal to a plane that contains both the incident radiance vector from the sky element of interest and the incident solar radiance vector. These two vectors are first analyzed into their unit vector components:

Q = the sky incident radiance vector

$$Q = \begin{bmatrix} Q_x \\ Q_y \\ Q_z \end{bmatrix} = \begin{bmatrix} \sin\theta\cos\varphi \\ \sin\theta\sin\varphi \\ \cos\theta \end{bmatrix}$$

Equation 3-18

S = the solar incident radiance vector

$$S = \begin{bmatrix} S_x \\ S_y \\ S_z \end{bmatrix} = \begin{bmatrix} \sin\theta_0\cos\varphi_0 \\ \sin\theta_0\sin\varphi_0 \\ \cos\theta_0 \end{bmatrix}$$

Equation 3-19

The polarization vector P is the cross product of S and Q:

$$P = \begin{bmatrix} P_x \\ P_y \\ P_z \end{bmatrix} = S \times Q = \begin{bmatrix} S_y Q_z - S_z Q_y \\ S_z Q_x - S_x Q_z \\ S_x Q_y - S_y Q_x \end{bmatrix}$$

Equation 3-20

This cross-product specifies the orientation of the polarization ellipse for the pure Rayleigh scattering model.

For the in-field experiment, the reference axis is the z-axis and the reference plane is the y-z plane (the sun is always in the +y direction).

Therefore, the calculation of the azimuth angle of the polarization ellipse for each sky element is:

$$\Theta_{pol} = \tan^{-1}\left(\frac{P_x}{P_y}\right)$$

If a sky element is within the reference plane (which also coincides with the principal plane for the in-field test), the azimuth angle is 0°.

Calculation of the incident radiance Stokes vector

The incident radiance Stokes vector S_{sky} for each sky element is readily calculated using Equation 2-28:

$$S_{sky}(\theta,\varphi) = \begin{bmatrix} I \\ Q \\ U \\ \approx 0 \end{bmatrix} = \begin{bmatrix} L \\ LP\cos 2\Theta_{pol} \\ LP\sin 2\Theta_{pol} \\ \approx 0 \end{bmatrix}$$

Calculation of the reflected Stokes vector

The Stokes vector image resulting from this imaging system can be fully described by Mueller matrix calculus:

$$S_{out} = [Polarizer(\theta)][Rot(\alpha)][Mirror(\beta)][Rot(-\alpha)]S_{sky}$$

where

$Rot(-\alpha) = $ rotation of the incident Stokes vector S_{sky} from the polarizer reference frame to the mirror reference frame (the azimuth angle α of each facet),

$$Rot(-\alpha) = \begin{bmatrix} 1 & 0 & 0 & 0 \\ 0 & \cos(-\alpha) & \sin(-\alpha) & 0 \\ 0 & -\sin(-\alpha) & \cos(-\alpha) & 0 \\ 0 & 0 & 0 & 1 \end{bmatrix}$$

$Mirror(\beta) =$ the polarizing effect of reflection from the mirror,

$$Mir(\beta) = \frac{1}{2} \begin{bmatrix} (r_\perp^2 + r_\parallel^2) & (r_\perp^2 - r_\parallel^2) & 0 & 0 \\ (r_\perp^2 - r_\parallel^2) & (r_\perp^2 + r_\parallel^2) & 0 & 0 \\ 0 & 0 & -2r_\perp r_\parallel & 0 \\ 0 & 0 & 0 & -2r_\perp r_\parallel \end{bmatrix}$$

$Rot(\alpha) =$ rotation of the mirror-reflected Stokes vector back to to the polarizer reference frame,

$$Rot(+\alpha) = \begin{bmatrix} 1 & 0 & 0 & 0 \\ 0 & \cos(+\alpha) & \sin(+\alpha) & 0 \\ 0 & -\sin(+\alpha) & \cos(+\alpha) & 0 \\ 0 & 0 & 0 & 1 \end{bmatrix}$$

and

$Polarizer(\theta) =$ the polarizing effect of each linear polarizer,

$$Pol(\theta) = \frac{1}{2} \begin{bmatrix} 1 & \cos(2\theta) & \sin(2\theta) & 0 \\ \cos(2\theta) & \cos^2(2\theta) & \cos(2\theta)\sin(2\theta) & 0 \\ \sin(2\theta) & \cos(2\theta)\sin(2\theta) & \sin^2(2\theta) & 0 \\ 0 & 0 & 0 & 0 \end{bmatrix}$$

A detailed description of the underlying mathematics can be found in Clarke and Grainger [1971]. Although the parameter V (which quantifies the fraction of right-handed circular polarization) is negligible in most terrestrial applications, it is recognized that the aluminum coating on the mirror might induce a small amount of circular polarization. However, the fact that the mirror is back-surfaced on an acrylic matrix suggests that any otherwise measurable amount of circular polarization will be masked through depolarization; the results bear out this hypothesis.

3.4 Image Data Analysis

This section describes the analytic techniques that were applied to the Stokes imagery obtained from both the in-field and aerial image data collections. The majority of the image data analysis was accomplished with the use of ENVI™ on-line analytic software capabilities.

3.4.1 In-field image data analysis

Full image scene analysis

Means, variances, and histograms of pixel intensity were calculated for full scenes from the calibrated image datasets. These statistics provide coarse benchmarks for comparison with the sub-scene (feature) statistics that follow.

Dome mirror scene analysis

512 x 512 pixel subsets of the dome mirror subimages in the Scene 1 images were cropped for qualitative comparison with the synthetic imagery from the image data simulation.

In-scene step wedge and neutral density card analysis

Means and variances of pixel intensity were calculated for 10 x 10 pixel subsets from each of the 10 steps on the in-scene step wedge that is visible in each collection. Means and variances of pixel intensity were calculated for 66 x 66 pixel subsets from the neutral density card visible in

each collection. Figure 3.4-1 illustrates the ENVI™ capability for selecting small regions for statistical analysis.
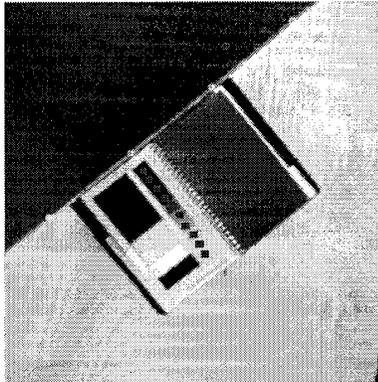

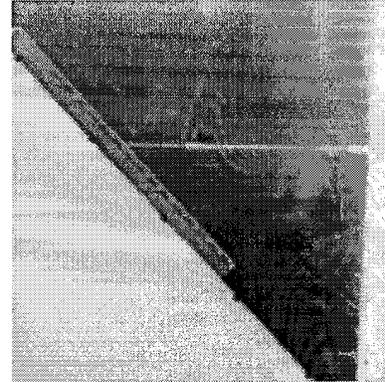**Figure 3.4-1.** In-scene step wedge and neutral density card measurement.

Figure 3.4-2. In-scene solar elevation measurement.

In-scene solar elevation measurement

The length of the shadow formed by a small (5.5-inch) vertical post mounted on the platform was measured using the ENVI™ cursor location capability. The pixel length was calibrated with the known length of the panels in order to accurately estimate the solar elevation. Figure 3.4-2 illustrates the visible shadow in a negative intensity image.

The solar elevation is then directly calculated:

$$Solar\ Elevation = \tan^{-1}\left(\frac{Shadow\ Length[in]}{5.5\ [in]}\right)$$

Equation 3-28

Panel scene analysis

Means, variances, and histograms of pixel intensity were calculated for large representative areas of the textured panels. The statistics were

collected for both fully illuminated and mirror-shadowed areas in the Scene 1 images.

Power Spectral Density (PSD) analysis

Representative 128 x 128 pixel subsets of the two panels were cropped from Scenes 2 through 6 for PSD analysis. The means, variances, and histograms were first calculated from the image subsets prior to fast Fourier transformation (FFT) and generation of the PSDs.

In order to establish a basis for comparison between scenes, normalized power spectral densities (PSDs) were calculated for each subimage:

$$PSD_{norm}(k_x, k_y) = \frac{\left[\left|FFT_{2D}(I(x,y) - \bar{I})\right|\right]^2}{s^2} \, x \, 100\%$$

<div align="right">Equation 3-29</div>

The mean intensity is first subtracted from the image. The motivation for subtracting the mean is to make the central ordinate of the FFT zero. Since the central ordinate of the FFT is the mean, does not contribute to the evaluation of image variance, and generally has the greatest magnitude of all the spectral components, this step facilitates scaling of the transformed image:

$$FFT_{2D}(0,0) = \bar{I} = 0$$

<div align="right">Equation 3-30</div>

The unbiased image is then 2D fast Fourier transformed through the ENVI^{TM} filter option. The PSD is created by squaring the transform:

$$PSD(k_x, k_y) = \left|FFT(k_x, k_y)\right|^2$$

<div align="right">Equation 3-31</div>

The third step divides the PSD by the intensity variance of the image. The motivation is to scale the PSD so that each spectral component now represents its fractional contribution to the total variance, since

$$\iint PSD(k_x, k_y)\, dk_x\, dk_y = s^2$$

<div style="float:right; border:1px solid black; padding:2px;">Equation 3-32</div>

Scaling the PSD by 100% converts the fractional contribution of each spectral component to a percent contribution.

PSD stability analysis

A primary objective of this study is to compare the relative stability of polarimetric power spectral estimation over the given range of imaging geometries. In the absence of more robust stability analysis techniques, existing ENVI[TM] capabilities provide for an averaged periodogram approach, as described by Kay [1988]. The underlying assumptions in applying this approach are 1) the PSD from each realization represents an estimate of a similar process, in this case, reflected intensity from the same pseudo-random (and therefore deterministic) surface, i.e., the imaged scenes of the 'cracked ice' diffuser panels; and 2) significant deviations from the averaged PSD are the result of differences in imaging geometry.

In order to establish a basis of comparison between image spectra, the images were first rotated to a common azimuth with respect to panel orientation, taking into account the bias error caused by rotation of the polarimeter. 128 x 128 pixel subimages of the panels were cropped and the statistics (mean and variance) calculated. As before, the mean was subtracted from each image prior to calculation of the PSD and the PSDs

75

normalized. An average PSD was calculated for each combination of imaging geometry factors, azimuth angle and solar elevation angle:

$$\overline{PSD}_{(elv\,A)} = \frac{1}{4}\sum_{B=1}^{4} PSD_{(elv\,A,az\,B)}$$

<div style="text-align: right">Equation 3-33</div>

$$\overline{PSD}_{(az\,B)} = \frac{1}{4}\sum_{A=1}^{4} PSD_{(elv\,A,az\,B)}$$

<div style="text-align: right">Equation 3-34</div>

The Averaged Difference PSD (ADP) was then calculated for each combination of factors:

$$ADP_{(elv\,A)} = \frac{1}{4}\sum_{B=1}^{4} \left| PSD_{(elv\,A,az\,B)} - \overline{PSD}_{(elv\,A)} \right|$$

<div style="text-align: right">Equation 3-35</div>

$$ADP_{(az\,B)} = \frac{1}{4}\sum_{A=1}^{4} \left| PSD_{(elv\,A,az\,B)} - \overline{PSD}_{(az\,B)} \right|$$

<div style="text-align: right">Equation 3-36</div>

This spectrum represents the average difference in the variance at each spectral component between the averaged PSD and each of the PSDs that contributed to the average; it represents a relatively straightforward estimate of the stability of $\overline{PSD}$. The figure-of-merit for PSD stability is the integrated difference variance (IDV):

$$IDV = \iint ADP(k_x, k_y)dk_x dk_y$$

<div style="text-align: right">Equation 3-37</div>

In lieu of a packaged ENVI^{TM} capability to execute a double integration over a scalar ADP array, an alternative approach was to run the ENVI^{TM} statistics tool, create a histogram of the ADP, transfer the histogram data

to a file, and then run a simple FORTRAN program to integrate over the histogram:

$$IDV \cong \sum_{w=0}^{\Delta Var_{max}} (Pixel\ Count)(\Delta Var_w)$$

The deficit of using this approach is that the histogram bins ΔVar into discrete values, creating an unknown approximation error for values in the lowest bin. Since the expectation is that a majority of values are near-zero, all the variances below the value of the next lowest bin are truncated to zero by the histogram and there is no way to evaluate them. However, there is a related side benefit to this approach: on the assumption that it is the larger values of ΔVar that indicate significant trends, a raised (non-zero) threshold can be used to evaluate a fractional IDV:

$$IDV_{fractional} \cong \sum_{w=threshold}^{\Delta Var_{max}} (Pixel\ Count)(\Delta Var_w)$$

Several threshold values are used in order to demonstrate the validity of this histogram approach in the calculation of IDV.

3.4.2 Aerial image data analysis

While leaving the details to Chapter 4, this section must address the fact that only one of the 12 over-water collections was fully processed and available for polarimetric image analysis. The results from this truncated analysis of the one aerial image are provided as a qualified demonstration of feasibility rather than as an experimental outcome.

Homeogeneous sub-scene analysis

Means, variances, and histograms of pixel intensity were calculated for one large (512 x 512 pixel) representative area (wind-driven water-wave surface) that contained homogeneous spatial content.

Power Spectral Density (PSD) analysis

Four 256 x 256 pixel subsets were cropped from the larger sub-scene for PSD analysis. The means, variances, and histograms were first calculated from the image subsets prior to Fast Fourier Transformation (FFT) and generation of the PSDs. The normalized PSDs were then generated using the same method described for the in-field analysis.

PSD stability analysis

In the absence of experimental data relating the imaging geometry factors of elevation and flight azimuth, an average PSD was calculated for the four spatially contiguous sub-scene PSDs:

$$\overline{PSD}_{(sub-scene)} = \frac{1}{4} \sum_{C=1}^{4} PSD_{(subscene\,C)}$$

Equation 3-40

This analysis should demonstrate the assumption of spatial invariance for the quasi-stationary pseudo-Gaussian process of a localized wind-driven waterwave surface [Kinsman, 1965]. This analysis should also provide yet a third averaged periodogram method for comparing the relative PSD stabilities of the polarimetric image components.

4.0　Results and discussion

The full description of results and discussion comprises five sections:

General results - This section describes the analysis of the general execution of the collection and processing phases.

In-field calibration results - This section describes the calibration analysis of the in-field imaging experiment.

Image simulation results - This section describes the qualitative comparison of the imaging simulation with real imagery.

Aerial calibration results - This section describes the calibration analysis of the aerial imaging demonstration.

Spatial analysis results - This section describes the spatial analysis of sub-image features in both the in-field and aerial collections.

4.1　General results

Quad image co-registration

The four members of each image quad were co-registered using the registration tools available within ENVI^{TM}. For the in-field images, a black dot in the center of each of eight in-scene markers (thumbtacks) served as a common ground control point in each of the quad members.

For the aerial images, spatially distributed high-contrast corners and edges were used to the maximum possible extent.

Pre-registration evaluation of the marker pixel coordinates for all 20 in-field image quads indicated that a simple translation of image pixel coordinates was the only requirement for co-registration. This requirement was consistent with the expectations for the specified imaging geometry:

1) the exterior orientation aligns the four optic axes parallel with nadir and aligns the web axis parallel with the defined reference plane, i.e., the orientation angles omega (ω), phi (φ), and kappa (κ) are zero within small tolerances; and rotation errors (that were detected during analysis) that make kappa non-zero would cause a uniform change in translation to all four quad members during quad co-registration,
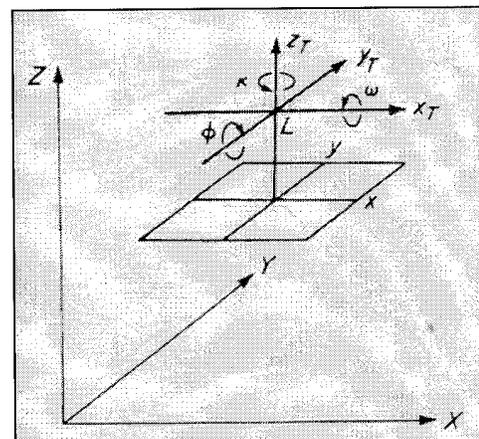
Figure 4.1-1. Exterior orientation coordinate system [from Moffitt & Mikhail, 1980].

2) the primary imaging target (the textured flat panels) were centered on the nadir point and aligned perpendicular with the optic axes,

and

3) the four image quad members were exposed on the same spool of film; the single film spool is processed in-line on the same digitizer;

centering errors would only cause a change in x-axis translation between frames (image pairs) during quad registration.

The overall root-mean-square (RMS) error for the 60 co-registrations required for the 20 in-field quad images was 0.29 pixel with a standard deviation of 0.34 pixel; the overall RMS error for the six co-registrations required for the two aerial quad images (of the nine that were successfully transferred to photo CD) was 0.45 pixel with a standard deviation of 0.37 pixel. This result was, for the most part, due to the lack of sharp, high-contrast common ground points. The extent to which low resolution optics, atmospheric attenuation, and aircraft motion were underlying causes is currently unknown but worthy of future analysis.

The main observation made during the co-registration process was that operator error must be considered within the registration error budget. The visual selection of the centroids of the in-field markers and the common intersections of the ground features in the aerial images was subjective. Considering that co-registration of polarimetric imagery is predominantly a translation of coordinates, the operator could be removed as a source of error by the introduction of a semi-automated local cross-correlation tool to detect the centroid coordinates of a common in-scene feature between two images.

This topic will be further developed in Chapter 5.

<u>Primary characteristic curve calibration</u>

The intended primary method for providing radiometric calibration of the imagery was to use the sensitometric 24-step density wedge that was exposed on the leading edge of each film roll. The step wedge would

be transferred to photo CD and the digital number (0 to 255) mean and variance corresponding to the film exposure at each wedge step could then be directly calculated from the digital image using the ENVI region statistics option.

Two errors in processing the sensitometric step wedge occurred. The automatic color/contrast balance controls were not disengaged (as requested) during photo CD processing, resulting in incomplete transfer of the full step wedge (due to automatic rejection of low-contrast images) and contrast distortion (due to automatic contrast enhancement) of the few step wedge images that were transferred. These errors rendered the digitized step wedges unuseable for direct digital radiometric calibration.

However, the secondary in-scene step wedges were available on each image for the in-field imaging experiment and were subsequently used for backup characteristic curve calibration. This backup calibration source was crucial in the presence of automatic color/contrast balance control since each image frame (containing a quad pair) was contrast-adjusted based on its scene content. This loss of calibration was most significant for the aerial collections since the inclusion of secondary in-scene step wedges was not feasible for the aerial imagery.

Base upon this outcome, there are three options to be considered for future polarimetric image data processing:

1) include a calibrated in-scene (or rather, in-frame) step wedge within each image frame on the film so that sensitometric calibration can be achieved independent the effects of any post-development processing that may occur,

82

2) include a single calibrated step wedge on each roll of film, as was currently done, but maintain full control of post-development film processing, e.g., operate an in-house film scanner/digitizer, so that all post-development effects are known and controllable,

or

3) eliminate the use of film as an intermediate image data transfer medium and instead use a calibrated focal plane detector array to directly generate a calibrated digital image.

This topic will be further developed in Chapter 5.

4.2 In-field calibration results

<u>General collection results</u>

Twenty-eight photo quads (56 35-mm frames) were collected between 1048 and 1554 EST on 07 Nov 1994. A summary of the collection results is listed in Table 4-1.

The -1st solar elevation collection attempt was intended to duplicate the +1st solar elevation attempt since the two sets would be taken at the same approximate solar elevation, the -1st set taken one hour before solar noon (maximum solar elevation) and the +1st set taken one hour after solar noon. However, the -1st collection experienced several hardware failures with the camera mechanism and was rejected: the resulting images from this collection window were either double-exposed and/or contained the photographer as an undesirable in-scene feature during the attempt to service the mechanism.

The 0th solar elevation collection attempt (circa solar noon) had one additional mechanical failure while imaging the first scene but all subsequent imaging was successful. However, the full 0th collection was also rejected for further processing based on three considerations. First, the collection was incomplete with the absence of the first scene; second, the remaining collections were all captured on one roll of film, eliminating the need for later inter-roll calibration and analysis; and third, the difference in solar elevation between the 0th and 1st datasets was small relative to the elevation differences between the subsequent sets.

Time EST	Solar Elev	Quad Nbr	Frame Nbrs	Scene Nbr	Remarks
			Table 4-1		
			Collection Results Summary		
1048	-1st	1	01/02	1	shutter failure
1050	-1st	2	03/04	1	shutter failure
1052	-1st	3	05/06	2	advance failure
1150	0th	4	07/08	1	shutter failure & advance failure
1153	0th	5	09/10	2	good take
1155	0th	6	11/12	3	good take
1157	0th	7	13/14	4	good take
1159	0th	8	15/16	5	good take
1248	1st	9	17/18	1	good take
1250	1st	10	19/20	2	good take
1252	1st	11	21/22	3	good take
1253	1st	12	23/24	4	good take
1254	1st	13	25/26	5	good take
1348	2nd	14	27/28	1	good take
1349	2nd	15	29/30	2	good take
1351	2nd	16	31/32	3	good take
1353	2nd	17	33/34	4	good take
1354	2nd	18	35/36	5	good take
1448	3rd	19	37/38	1	good take
1449	3rd	21	39/40	2	good take
1451	3rd	22	41/42	3	good take
1453	3rd	23	43/44	4	good take
1454	3rd	24	45/46	5	good take
1548	4th	19	47/48	1	good take
1549	4th	21	49/50	2	good take
1550	4th	22	51/52	3	good take
1552	4th	23	53/54	4	good take
1554	4th	24	55/56	5	good take

In sum, because of the intensive processing requirements, these considerations favored the selection of the remaining four collection sets (20 quads = 40 frames) for follow-on processing and analysis.

All the exposed film from the in-field experiment was turned over to a comercial vendor for standard KODAK film development and direct Photo CD^{TM} processing. Special photo CD processing instructions included requests to turn off the color/contrast balance controls, to scan in the step wedge, and to center the two pairs of images within two standard 35-mm frames. Subsequent analysis will show that the balance controls were not disabled during processing. One of the direct consequences of retaining this processing algorithm was rejection of most of the step wedge images and contrast distortion of the remainder, i.e., secondary characteristic curve calibration was possible only for the in-field imagery.

Upon receipt of the processed CDs, all subsequent digital data processing and analysis proceeded as described in Chapters 3.2 and 3.3.

Secondary characteristic curve calibration

The backup method for providing radiometric calibration of the in-field imagery was to use the in-scene 10-step density wedge that was visible within each image collection. Means and variances of pixel intensity were calculated for 10 x 10 pixel subsets from each of the 10 steps, using the ENVI region statistics capability.

Figure 4.2-2 plots all 20 characteristic curves for the uncalibrated intensity (I) images. This plot demonstrates the effect of contrast optimization that was applied by the photo CD processing algorithm.

86

Scenes 3 and 5 projected less total reflected radiance to the sensor because the mean azimuth of the reflecting panel facets (the predominant scene component) was aligned 45° and 135° from the principal plane
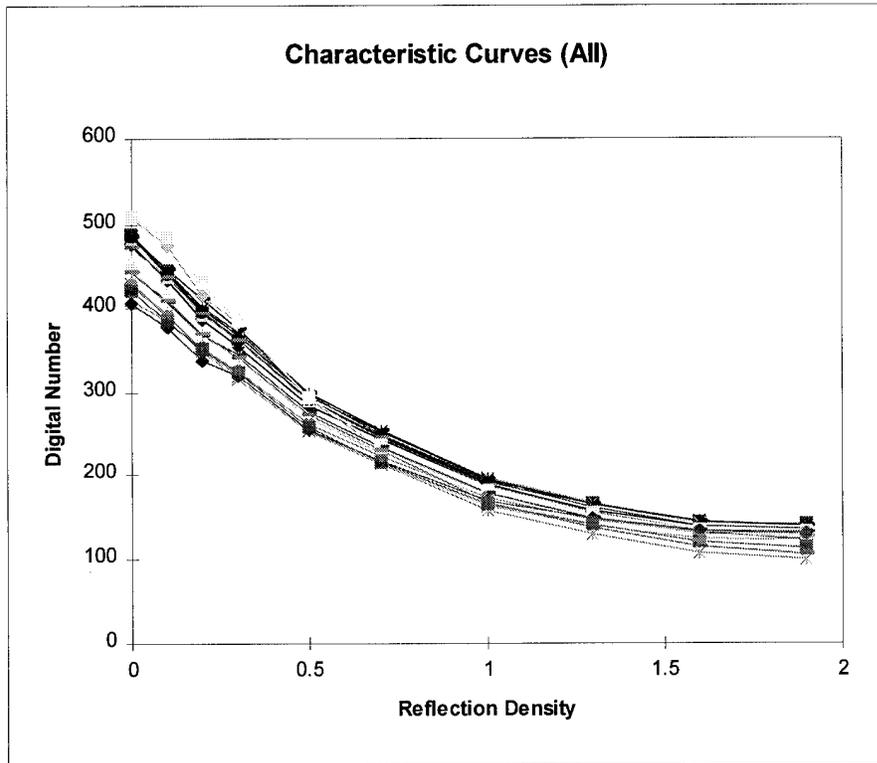
Figure 4.2-2. (Note that the dn range is 0 to +510.)

(containing the sun). The net result was a minimum reflected total radiance among the five scenes, and the photo CD contrast optimization algorithm compensated by applying higher digital numbers to the scanned pixels. The upper curves in Figure 4.2-1 plot the effect of this compensation. Conversely, Scenes 1, 2, and 4 projected more reflected radiance because the mean panel facet azimuths were aligned in parallel with, and perpendicular to, the principal plane, reflecting more sunlight to the sensor. In turn, photo CD contrast optimization applied lower digital numbers (dn) to these images; the lower curves plot the effect of this compensation.

87

Figure 4.2-3 plots the average characteristic curve for the two darker scenes (8 images) as the upper trace; the curve for the three brighter scenes (12 images) as the lower trace; and the total collection average (20 images) as the middle curve.

Characteristic Curves (Averages)
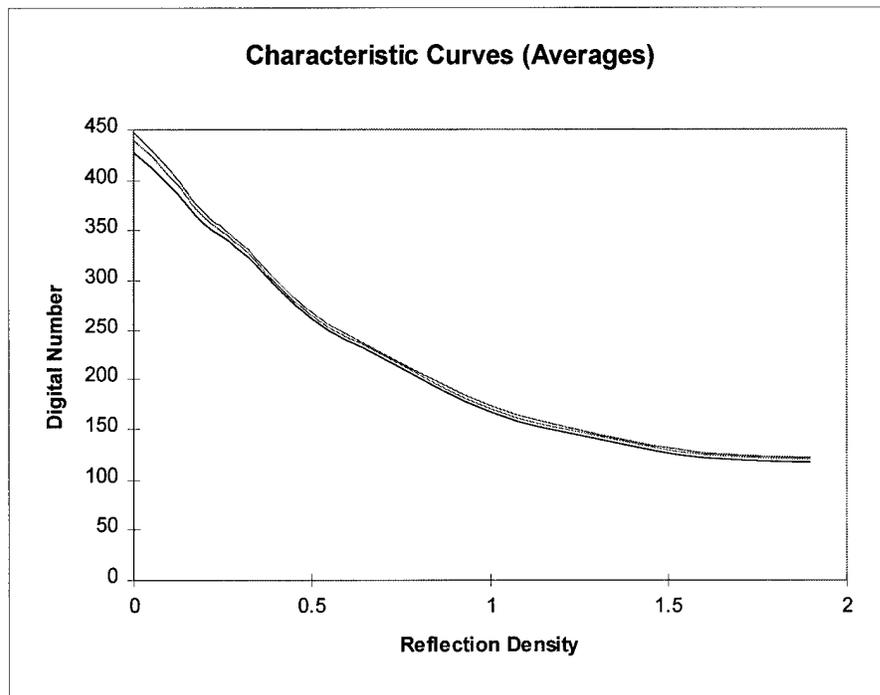
Figure 4.2-3.

There was one significant side benefit of the contrast optimization algorithm: linear stretching of the log(exposure) curve. The algorithm design provides linear optimization of the scanned pixel intensity so that digital number (dn) approximates actual pixel exposure/intensity.

Figure 4.2-4 plots log(digital number) versus reflection density to demonstrate the effect of linear optimization. A representative film characteristic curve would demonstrate an exponentially increasing region as density approaches zero, and an exponentially decreasing region as density aproaches maximum density. Instead, the log curve assumes

near-linearity across the range of measured densities. The one limitation of this plot is the lack of measurement for higher reflected densities, since the lower dn region is not mapped. However, the trend at D = 1.9 does not indicate/predict exponentially decreasing values of log(digital number).
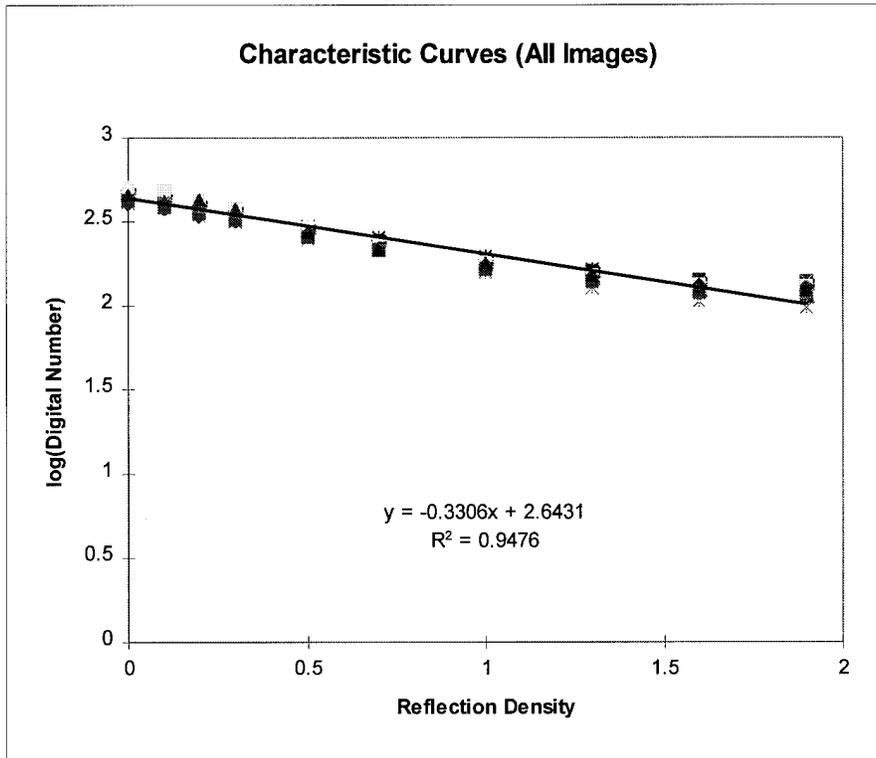
Figure 4.2-4.

A least-squares linear fit was applied to all the uncalibrated data and is plotted on Figure 4.2-4. Since normal characteristic curves plot density as a function of log(exposure), the mean effective system gamma (γ) is the negative reciprocal of the fitted line slope on this plot:

$$\gamma = \frac{\Delta D}{\Delta \log E} = \frac{\Delta (reflection\ density)}{\Delta \log(digital\ number)} = \frac{-1}{-0.3306} \cong 3.0 \qquad \boxed{\text{Equation 4-1}}$$

In lieu of more comprehensive sensitometric data, this least-squares fit line was used as the common baseline for calibrating the image datasets,

i.e., the pixel digital numbers for each image quad were interpolated so that the least-squares D-log(DN) line for each photo pair matched this baseline. Since

$$[\gamma_{cal} \log(DN_{cal}) - bias_{cal}] = D = [\gamma_{uncal} \log(DN_{uncal}) - bias_{uncal}]$$

<div style="text-align: right;">Equation 4-2</div>

then

$$DN_{cal} = 10^{[(\gamma_{uncal} \log(DN_{uncal}) + bias_{cal} - bias_{uncal})/\gamma_{cal}]}$$

<div style="text-align: right;">Equation 4-3</div>

Image analysis of the radiometric calibration

The calibrated image quads were used to create the Stokes vector and Stokes derivative images. However, since the sum of each of the two orthogonally polarized image pairs in the quad represents an estimate of the unpolarized intensity image (I), the statistics of the difference between the two sums can provide a system calibration check since, if the system was perfectly calibrated, the difference image (D) should be everywhere zero. Reprising Equation 3-6,

$$D = I' - I'' = [I(0°) + I(90°)] - [I(45°) + I(135°)] = \sim 0$$

<div style="text-align: right;">Equation 4-4</div>

As a demonstration of calibration performance, post-calibration means and standard deviations were calculated for 66 x 66 pixel regions within the imaged neutral density card visible on all 20 collections. Figure 4.2-5 plots both statistics for the difference (D) subimages.
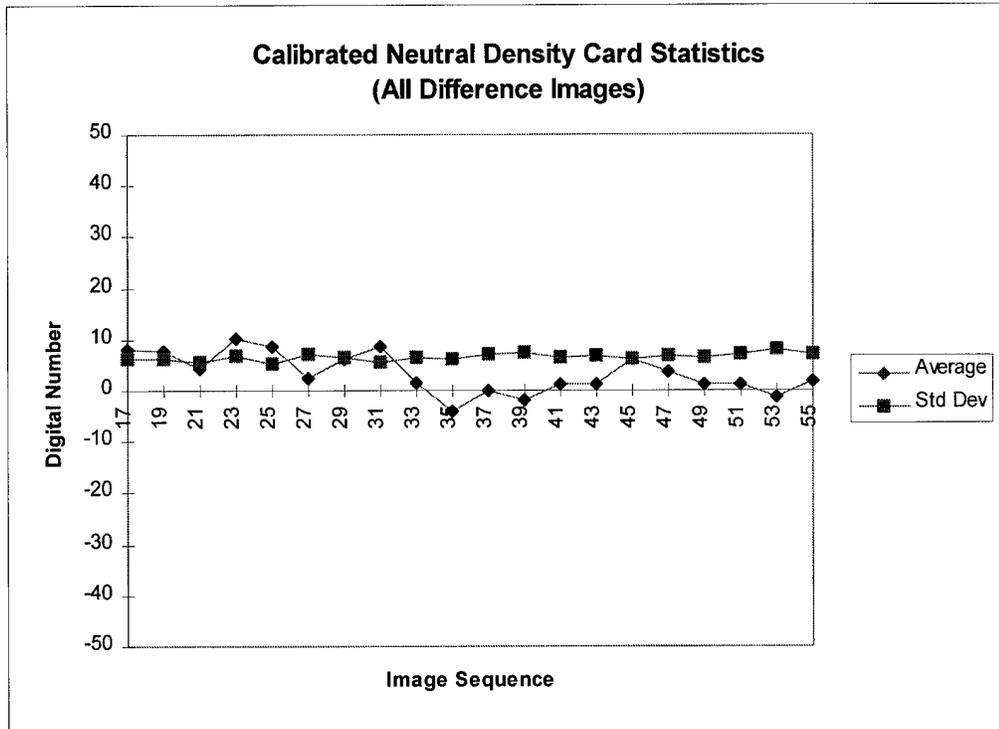
Figure 4.2-5. (Note that the full dn range for difference images is -510 to +510.)

The mean difference for the 20 images is +3.4 dn over a possible range of -510 to +510 dn, translating to a bias of less than +0.7%. The mean intra-image (I'-I") standard deviation for the 20 images shows a fairly constant value of about 6.6 dn, while the mean inter-image standard deviation is about one half that amount, 3.3 dn. Since the characteristic curves within each image quad do not differ as much as they do between independent image collections, this difference suggests that inter-image calibration was successful at reducing variability between images while intra-image (I' vs. I") calibration preserved an inherent system variation.

As a second demonstration, post-calibration means and standard deviations were calculated for the same 10 x 10 pixel subsets from the 10-step wedge visible on all 20 collections. Figures 4.2-6 and 7 plot these two statistics for all 20 difference (D) subimages. Figure 4.2-8 plots the combined statistics for the 20 difference subimages.

91

Calibrated Step Wedge Average
(All Difference Images)
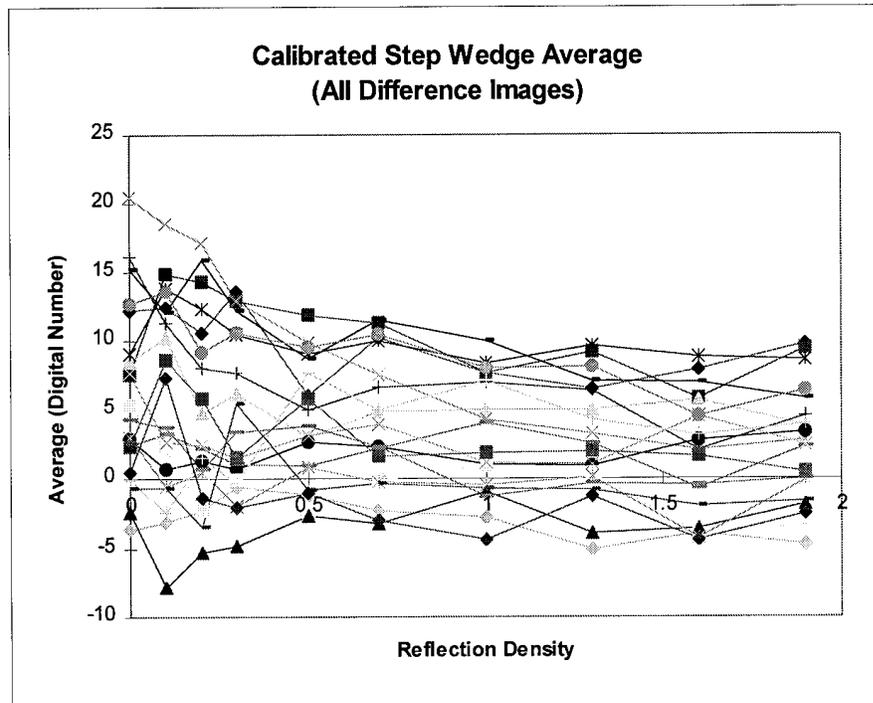
Figure 4.2-6. (Note that the full dn range is -510 to +510.)

The mean differences (Figure 4.2-6) demonstrate the same general
positive bias as was previously shown in the neutral density card data,
with digital numbers generally ranging between -5 and +10 dn and the
combined averages (Figure 4.2-8) showing a trend from +6 dn near D = 0
to +2 dn near D = 1.9.

The intra-image (I' - I") standard deviations (Figure 4.2-7) appear to
correlate with the same trend for intra-image means: the combined
deviation decreasing from 9-10 dn near D = 0 to 5 dn near D =1.9. The
very low deviations at D =0 correspond to intensity values that were close
to saturation (dn = 510) for those image subsets, limiting the upper range
of dn variation.

92
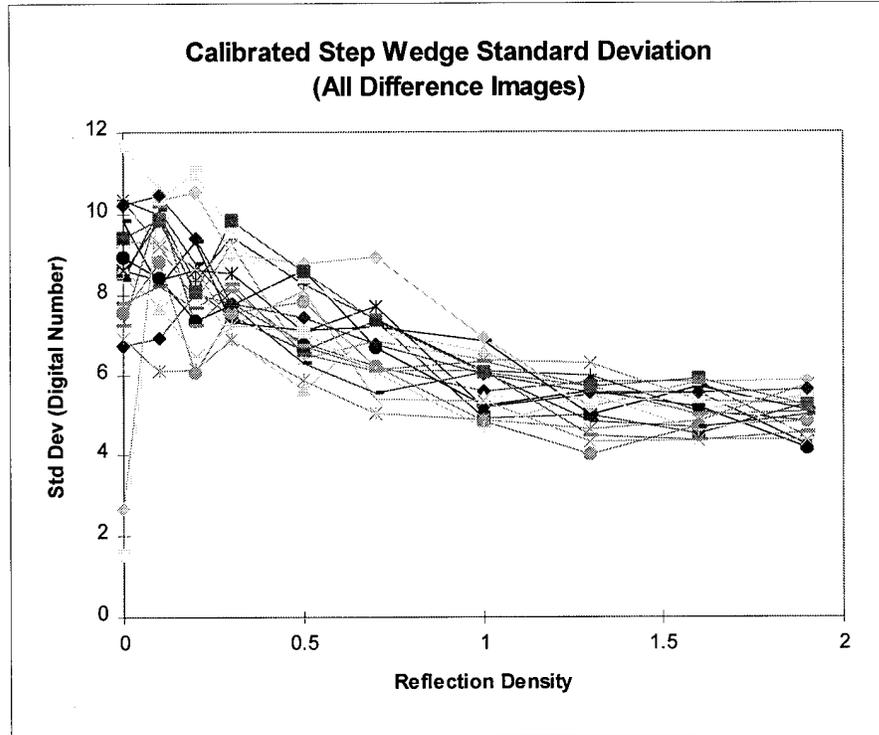
Figure 4.2-7.

Figure 4.2-8.

93
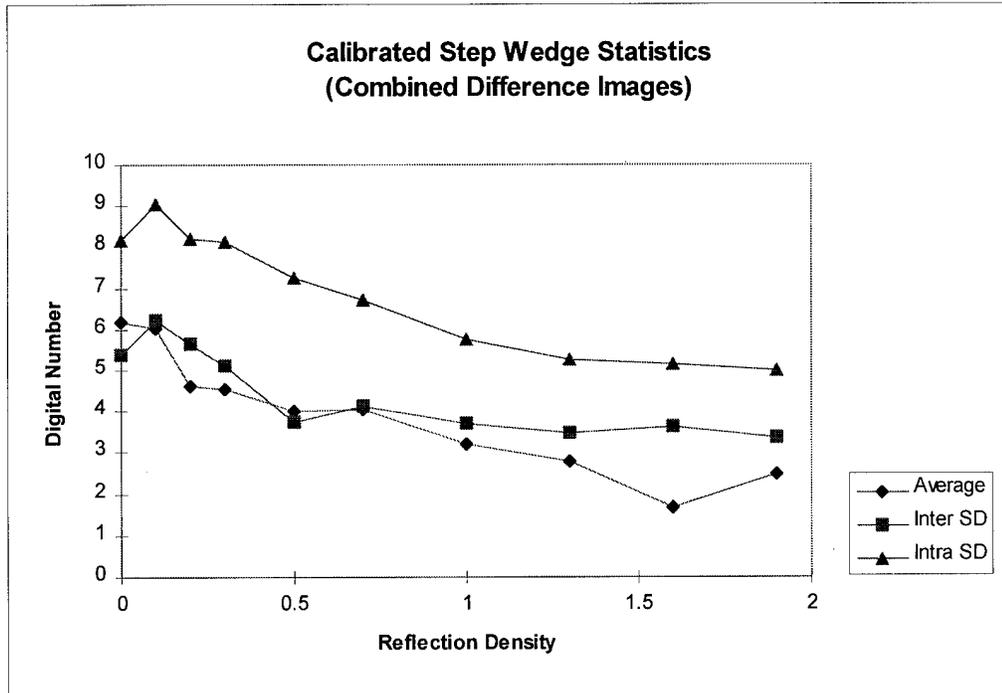
The combined inter-image and intra-image standard deviations (Figure 4.2-8) compare with the values for the neutral density card: the intra-image variation is consistently (1.5 to 2 times) greater than the corresponding inter-image variation at a given value of reflection density.

Since the characteristic curves are now normalized, the residuals from calibration alone will sum to zero bias. One explanation for the consistently positive bias (+3 to +6 dn) between the calibrated I' image pair and the I" image pair is clearly evident in Figure 4.2-9.

Calibrated Step Wedge Average
(Combined Difference Images by Solar Elevation)
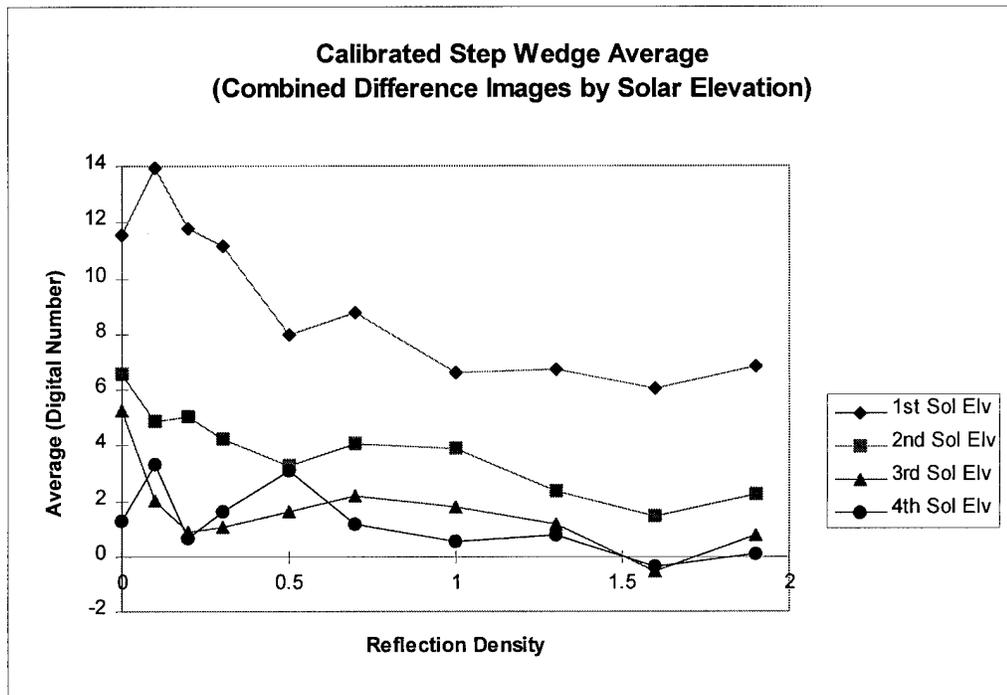
Figure 4.2-9. (Note that the full dn range is -510 to +510.)

The five images collected at each of the four solar elevations were combined to plot their mean difference over reflection density. Since each polarized image pair originally formed one 35-mm frame, the photo CD contrast optimization algorithm operated on the pair as if it were a single image. This is a significant problem for an image pair that has high

94

contrast in one member and low contrast in the other member. In particular, this condition describes the 0°/90° image pair, which maintains alignment with the principal plane in order to optimize differential contrast.

For image quads with reduced illumination, e.g., the 4th solar elevation dataset, the overall contrast difference within the two pairs would be small and contrast optimization would produce very similar characteristic curves. The net result is a difference (I' - I") image which approaches zero, as is seen in Figure 4.2-9.

However, for image quads with increased illumination, e.g., the 1st solar elevation dataset, the overall contrast difference would be larger and contrast optimization would produce dissimilar characteristic curves. Although a normalized characteristic curve is applied individually to each member of the quad, the net result is a difference image which preserves the nonlinearities of the differential contrast optimization created during photo CD processing.

In sum, the overall effect of contrast optimization on the radiometric calibration of the image quads is a balance. However, analysis of the calibration data presented so far suggests that the encountered errors are both reasonable and explainable if not removeable or reducible. The most significant feature of the calibration is the presence of a systematic bias between the estimates of I' and I" that varies between +0.5% and +1.0%.

Polarizer reference alignment analysis

Minor rotations of the exterior orientation parameter kappa (κ) were visible in the imagery. (Refer to Figure 4.1-1.) The mounting frame

for the polarimeter apparently underwent a small amount of operator-induced twisting each time the film advance lever was manipulated. The amount of the rotation is plotted in Figure 4.2-10.
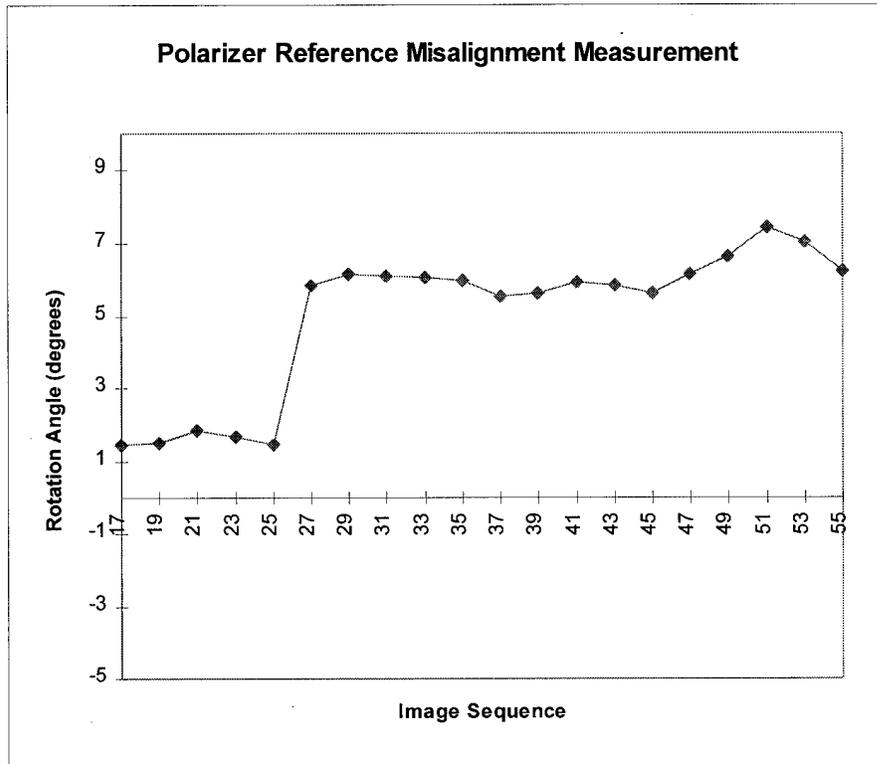
Polarizer Reference Misalignment Measurement

Figure 4.2-10. (Note that the full rotation range is -180° to +180°.)

The procedure for measuring this rotation was to measure the pixel coordinates of the two endpoints of the line segment described by the abutment of the two test panels. Since the panels always maintained relative alignment with the reference plane in increments of 45°, the rotational alignment error of the polarizer relative to the reference plane could be measured for each image:

$$Rotation\ Error = \tan^{-1}\left(\frac{\Delta y}{\Delta x}\right) + n(45^o), \quad n = \{0,1,2,3\}$$

Equation 4-5

The results show that the polarizer was positively rotated over a range between +1.4° and +1.6° during the first solar elevation collection and was significantly increased to a range between +5.5° and +7.4° during subsequent collections.

Analysis of the mirror image subsets will demonstrate both the effect of this rotation error on the visualization of the reflected polarized skydome and the post-processing capability to compensate the Stokes imagery for this alignment error.

Solar elevation measurement analysis

The length of the shadow formed by a small vertical post mounted on the platform was used to calculate the solar elevation angle. The results of this measurement are listed in Table 4-2.

Table 4-2
Solar Elevation Secondary Measurement Results

Dataset Nbr	Solar Elevation	Std Dev
1st	+26.9°	0.2°
2nd	+23.0°	0.06°
3rd	+16.3°	0.04°
4th	+7.9°	0.04°

These values are plotted in Figure 4.2-11 against the calculated solar elevation angle versus local time. Sunrise (0°) was at 0645 EST and sunset (0°) was at 1650 EST.

These measured solar elevation values were used as inputs within the imaging simulation.

Solar Elevation Secondary Measurement

$R^2 = 0.9997$

Figure 4.2-11.
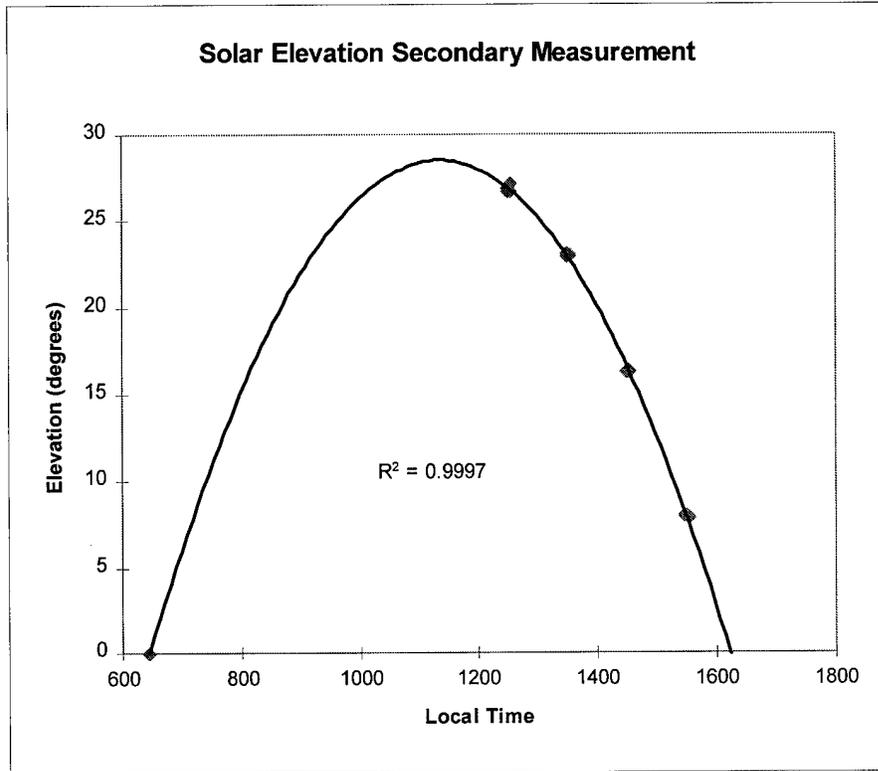
**I Histogram
(All Full Images)**
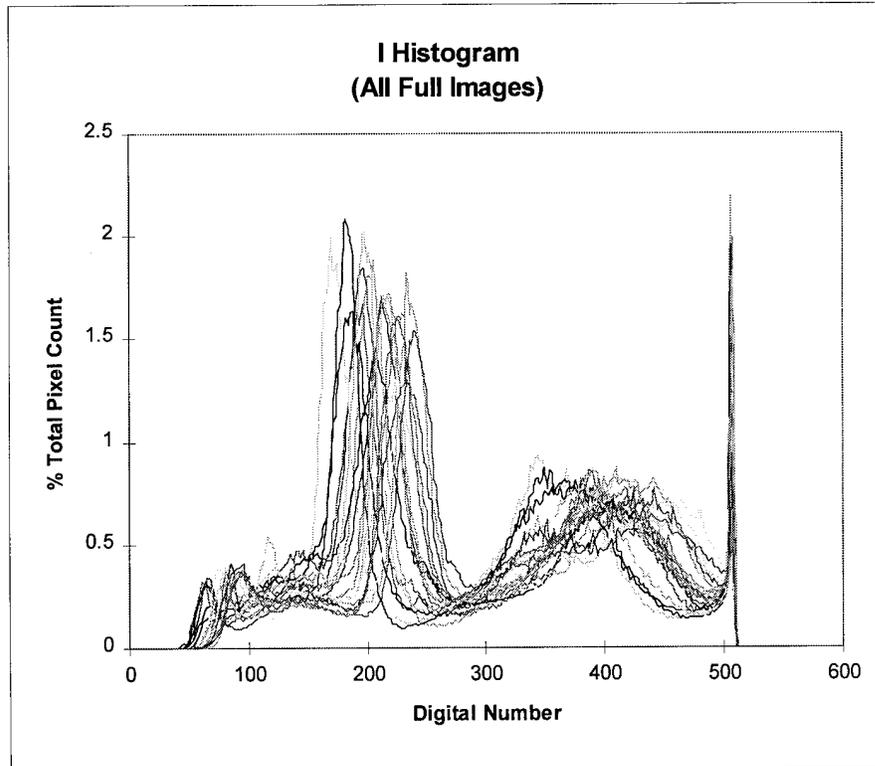
Figure 4.2-12.

Histogram analysis of the intensity (I) full images

Figure 4.2-12 plots all 20 histograms for the calibrated intensity (I) full images. This plot and subsequent plots demonstrate the high variability of intensity (I) relative to the other two Stokes parameters (P and T). This variability is directly attributable to the effects of imaging geometry, as will be shown in Figures 4.2-13 and 14.

There are two general features to note in these figures:

First, the two test panels are highly separable in the I histograms. The aggregate of the dark panel pixels have dn values centered in the neighborhood of dn = 200 and the light panel pixels are aggregated around dn = 400. The dark panel pixel distributions have about one half the variance of the dark panel distributions. (The full statistical comparison of the panels will be treated during sub-image analysis which follows.)

Second, the combined effects of film development and photo CD contrast optimization are apparent at the extrema. Almost no darker pixels are mapped to the lower dn values between 0 and 40. This apparent failure of contrast optimization is instead due to the presence of unexposed film area within the processed 35-mm frame. Because of the smaller exposure area in the Nishika camera, approximately 9% of a standard 35-mm frame is unexposed and the resulting processed pixels have dn values of zero. These dark pixels are considered in the contrast optimization, effectively adding a positive bias of 20 dn to the darkest exposed pixels (40 dn in the I image). The 3-5% of saturated pixels (dn values approaching 510) are the result of actual film saturation, contrast optimization, or both. These saturated pixels have a significant effect in the histogram analysis of the T (polarization ellipse orientation angle) images which follows.

Figure 4.2-13 illustrates the variation of intensity relative to solar elevation angle. In this case, reflected intensity generally increases as the solar elevation angle decreases, down to a minimum that appears to be near the 4th solar elevation. The key effect is due to the net Fresnel reflectivity of the panel facet slope distribution. The small but increasing distribution near dn = 100 are pixels in shadow.

Figure 4.2-14 illustrates the variation of intensity relative to scene geometry. In scenes 1, 2, and 4, the mean azimuth angle of the panel facet distribution is aligned with the principal plane, favoring reflection of direct sunlight. In scenes 3 and 5, the mean azimuth angle is rotated -45° and +45°, respectively, from the principal plane. The main benefit of using textured panels is that the reflection geometry of the scene is both a deterministic and controllable feature of the imaging experiment.

**I Histogram
(Combined Scene Full Images)**

Figure 4.2-13.

**I Histogram
(Combined Solar Elevation Full Images)**
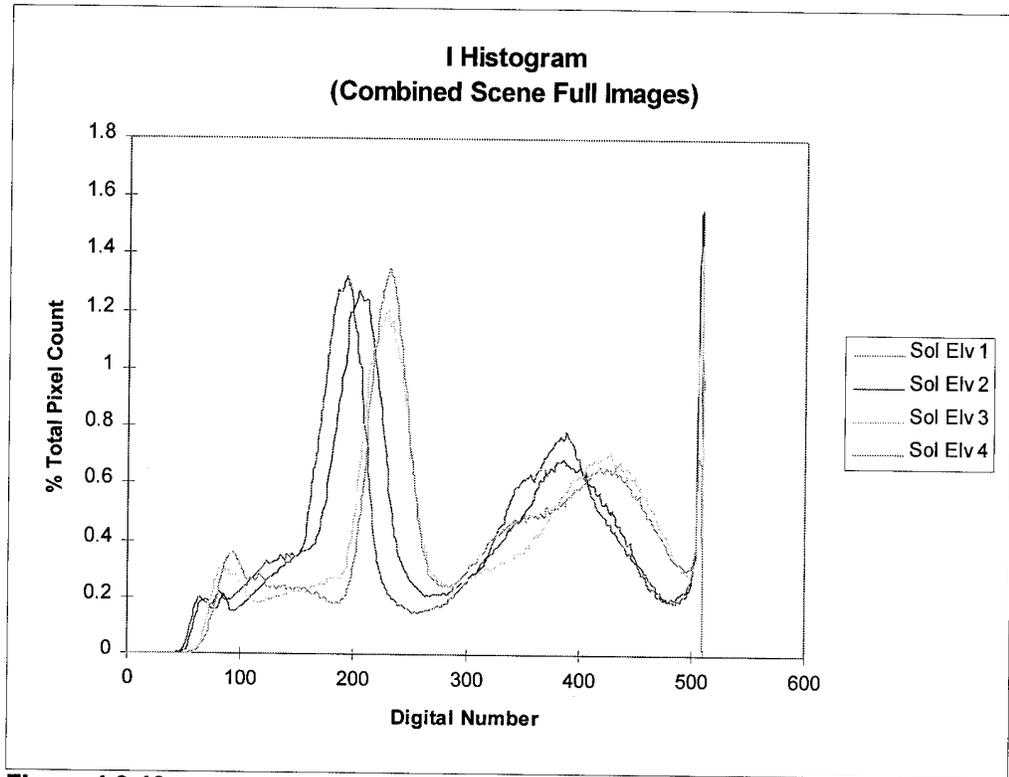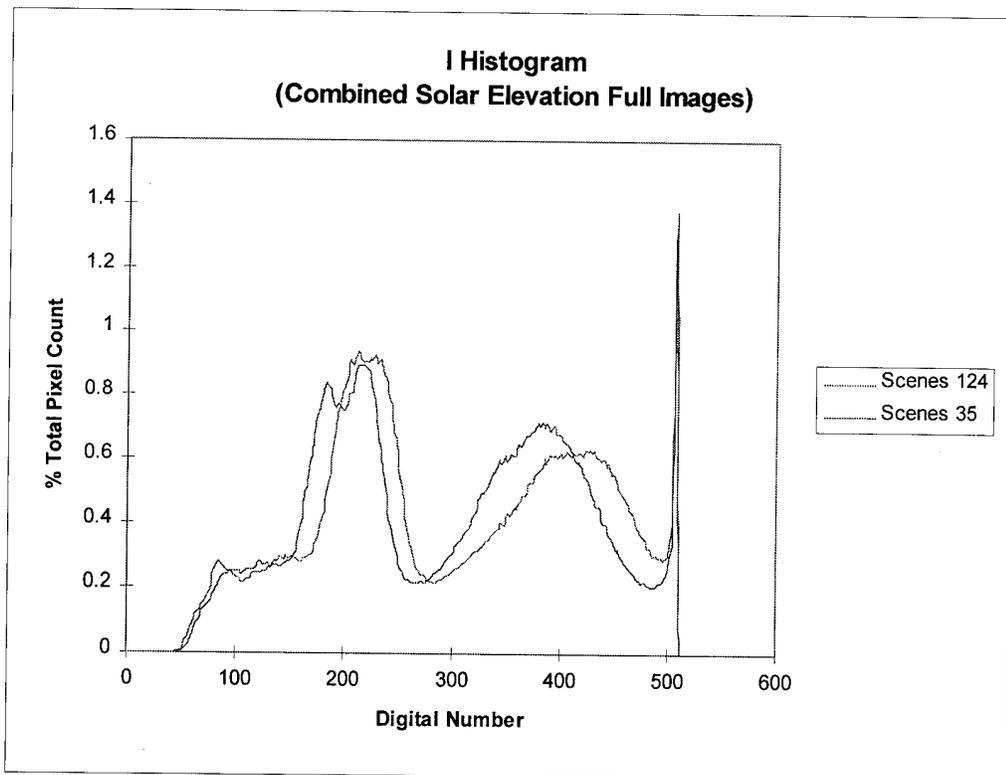
Figure 4.2-14.

Histogram Analysis of the % polarization (P) full images

Figure 4.2-15 plots all 20 histograms for the calibrated %
polarization (P) full images. This plot and subsequent plots demonstrate
both the relatively low variability of % polarization (P) compared with
intensity (I) and its relative independence of imaging geometry.
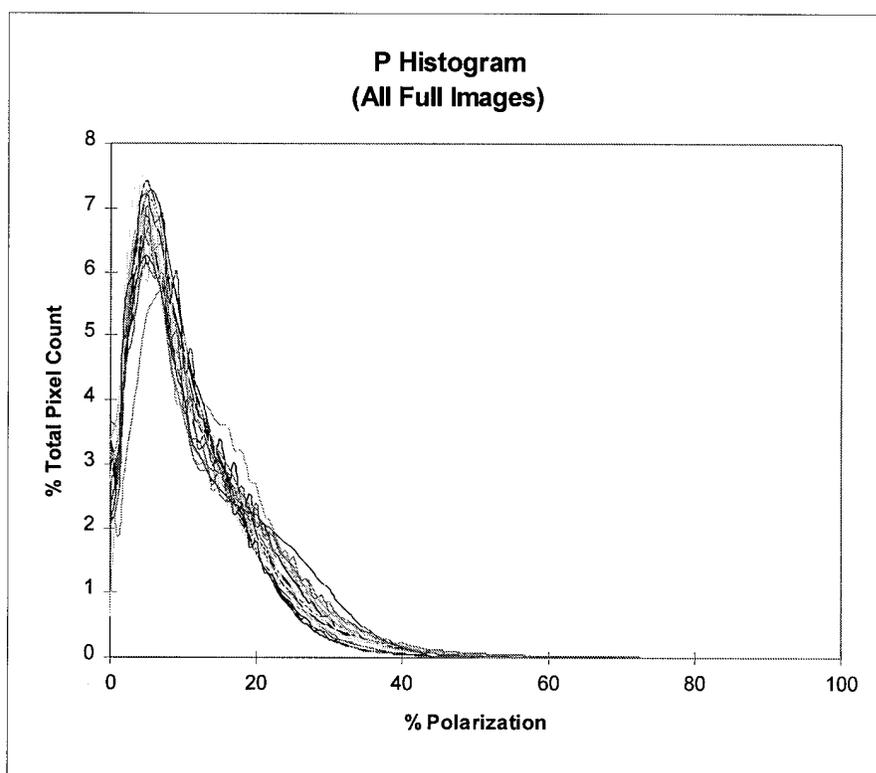
Figure 4.2-15.

The most significant feature of the P histograms is the relative
absence of pixels with polarizations approaching 100%: on average, less
than 0.5% of all the pixels in the 20 images have polarizations above
65%. The mode value averages 11.8% with a standard deviation of 0.9%.
In the absence of an independent system for calibrating the polarization
measurements to an absolute scale, the combined results indicate that
the measurements are statistically consistent over a relative scale. The
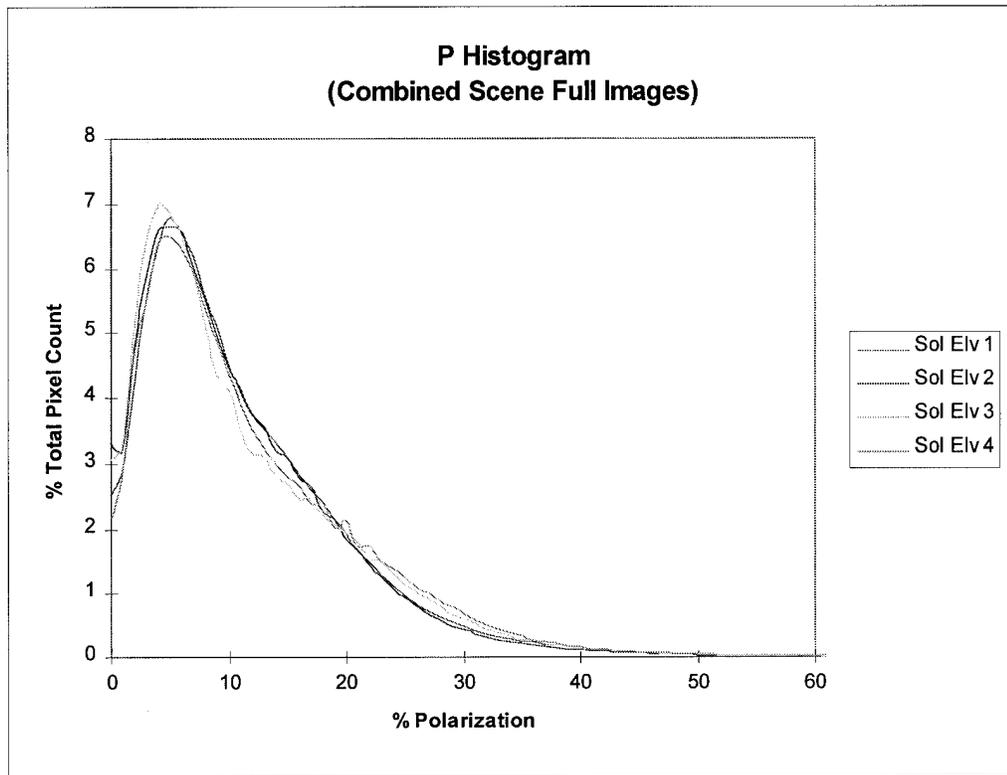
Figure 4.2-16. (Note the reduced scale for % polarization.)

expectation for non-ideal polarimeter performance is to observe some amount of systemic depolarization, primarily due to partial transmission of the orthogonal radiation component through a non-ideal linear polarizer. However, because there are four intensity measurements of radiation passing through the same non-ideal polarizing material, the net observed depolarization should be proportional for each Stokes component. In the calculation of polarization, this depolarization factor appears in both the numerator and denominator (Equation 3-4) and thus cancels out.

Figures 4.2-16 and 17 do not demonstrate any observable polarization trend with respect to solar azimuth or scene geometry. A more detailed analysis of individual features is provided in Chapter 4.5.

**P Histogram
(Combined Solar Elevation Full Images)**
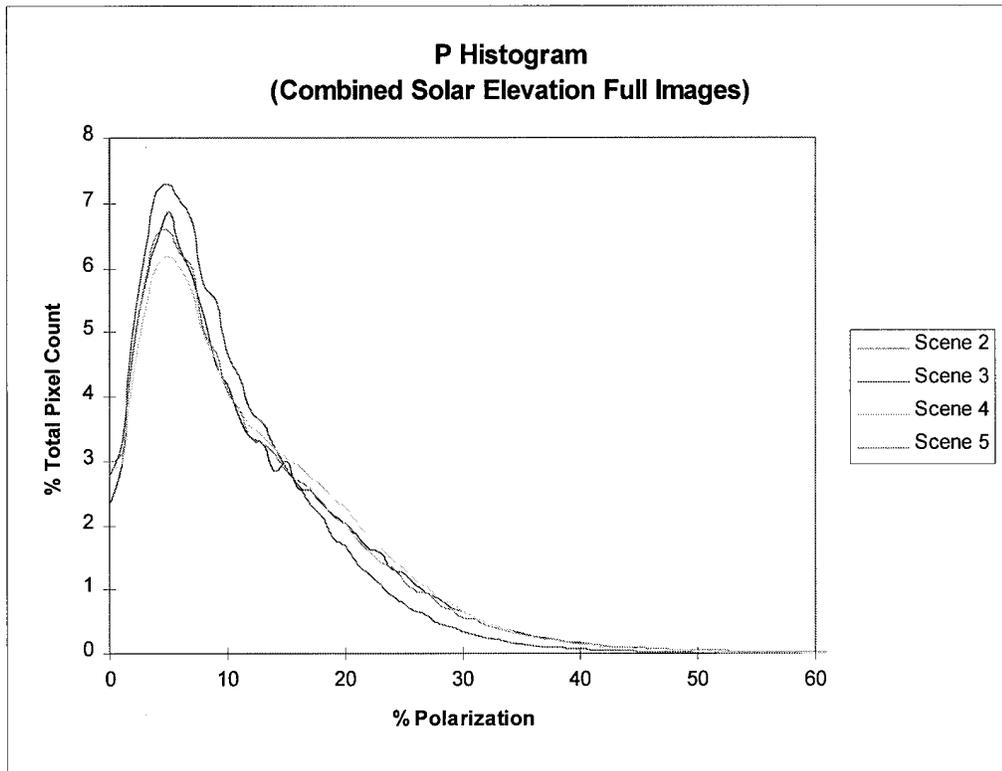
Figure 4.2-17. (Note the reduced scale for % polarization.)

Histogram Analysis of the orientation angle (T) full images

Figure 4.2-18 plots all 20 histograms for the calibrated orientation angle (T) full images. This plot and subsequent plots demonstrate the sensitivity of T to the presence of saturated pixel intensities as well as the rotational variation of kappa (κ). (Refer to Figure 4.1-1.)

The significant spikes at 22.5° intervals are mathematical artifacts created by the presence of one or both image pairs containing pixels with saturated intensity values, i.e., dn = 255. Referring back to Equation 3-5, T is the half-angle of the arctangent of the ratio of U and Q. The high pixel pixel count spikes occur at 2xT values of +/- 0°, 45°, 90°, 135°, and 180°.

104

TC Histogram (All Full Images)
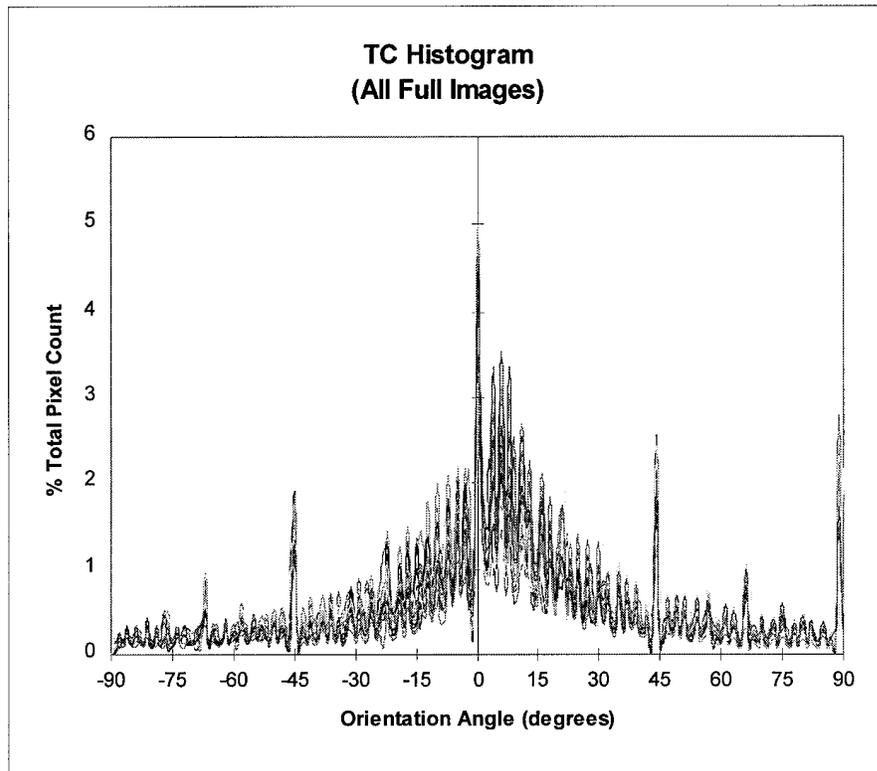
Figure 4.2-18.

The tangent of these angles corresponds to the following possible combinations of U and Q:

Table 4-3
U & Q Combinations

Angle	Tan(Angle)	Possible U & Q values
0°	0	U = 0, Q = {0 ..+510}
+45°	+1	U = Q = {+1..+510}
+90°	+∞	U = {+1..+510}, Q = 0
+135°	-1	-U = Q, U = |Q| = {+1..+510}
±180°	0	U = 0, Q = {-1..-510}
-135°	+1	U = Q = {-1..-510}
-90	-∞	U = {-1..-510}, Q = 0
-45°	-1	U = -Q, U = |Q| = {-1..-510}

TC Histogram
(Combined Solar Elevation 1 Full Images)

Figure 4.2-19.

TC Histogram
(Combined Solar Elevation 2+3+4 Full Images)
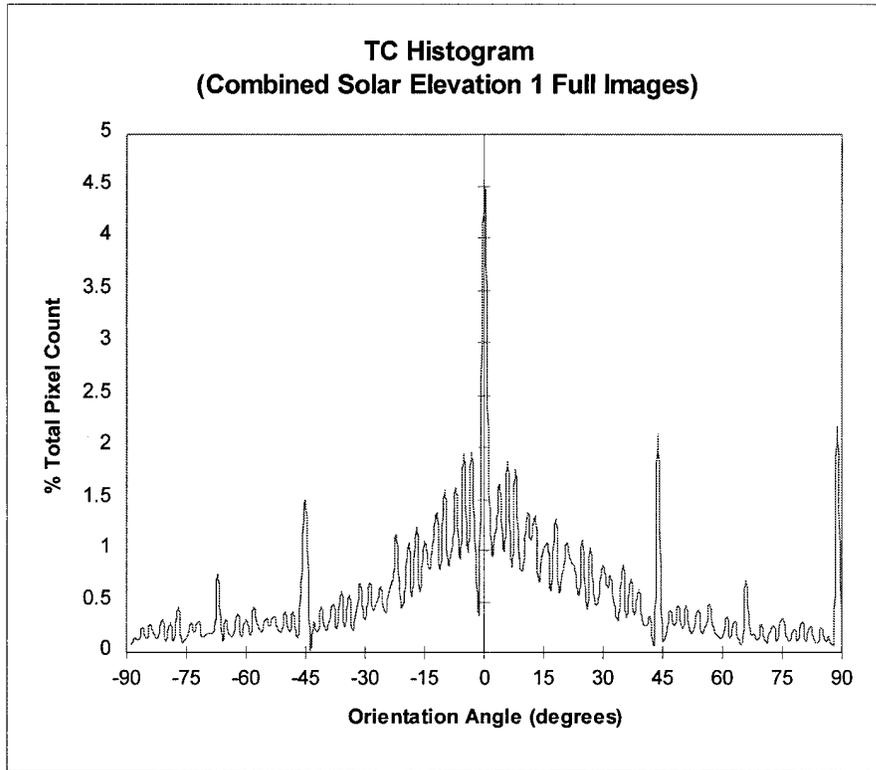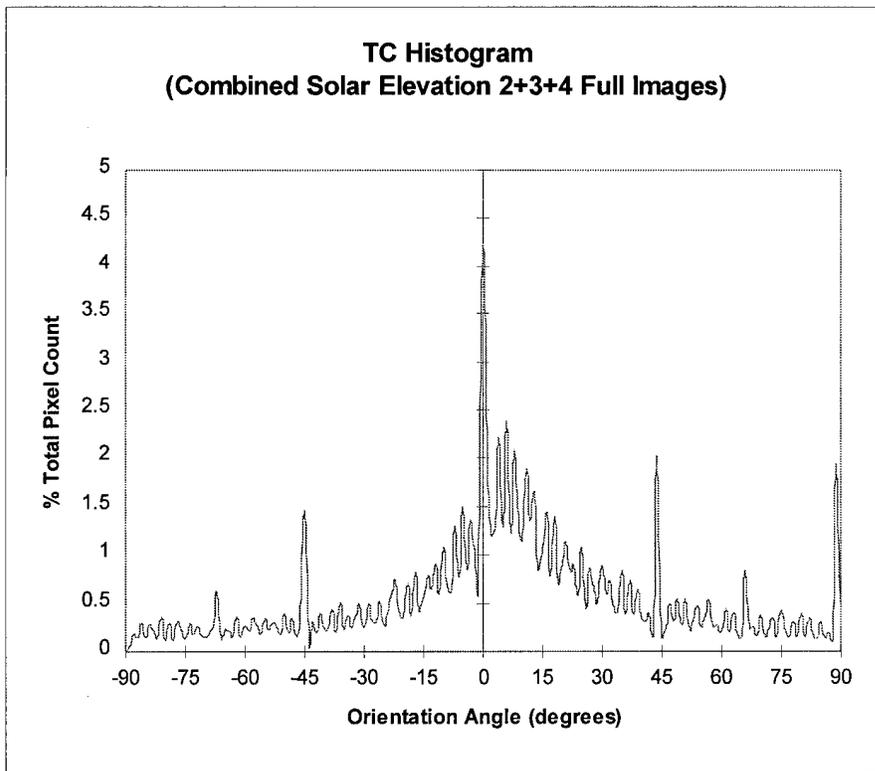
Figure 4.2-20.

The largest spikes occur where either U or Q are 0; the single largest spike occurs when U and Q are both 0. The less prominent spikes occur when U and Q fluctuate between values of -1 and +1. This incidence is observed for near and fully saturated pixel intensities within each polarized pair of an image quad. The same situation would exist near zero intensity. However, this situation was not observed within this experiment because of the large positive dn bias identified in the I image histogram analysis.

If these spikes are disregarded, the remaining distribution of T values provides a unique indicator for the azimuth location of the principal plane relative to the polarimeter reference plane. Figure 4.2-19 illustrates the combined average histogram of the first solar elevation collection, where the polarimeter rotation bias is approximately +1.5°; and Figure 4.2-20 combines the remaining collections, where the bias is in the vicinity of +6.5°. The distribution of T values approach a maximum pixel count at the azimuth location of the principal plane. This distribution correlates with the attenuated reflection of skylight from a surface containing reflecting facets that assume a near-uniform distribution of azimuths and a near-Gaussian distribution of slopes, for example, a waterwave surface. In fact, this same distribution is visible for the water surface T image histogram analyzed in Chapter 4.4.

In sum, the existence of truncated values at either extremum of the intensity scale will produce mathematical artifacts in the generation of the T parameter image, creating biases in the estimate of mean and variance. In the absence of these artifacts, the orientation angle of maximum pixel count can serve as an indicator of the principal plane azimuth in imaged scenes with near-homogeneous surface geometry statistics.

4.3   Image Simulation Results

The intent of this qualitative evaluation is compare the relative spatial distributions of clear sky Stokes parameter measurements from actual images of a reflecting dome mirror with the predictions of an imaging simulation that models the collection geometry. With reference to Chapter 3, no attempt was made to calibrate either the model or the imaging system for specific spectral response or absolute radiometry. The benefit of this qualitative approach is to provide a reasonableness check on the spatial performance of the system and model, consistent with the objectives of this study. Chapter 5 provides several suggestions for further research which would seek to both validate the model and calibrate the system.

With reference to Figures 4.3-1 through 4, the one signficant deviation is the existence of image saturation in the vicinity of the sun and the lack of same in the simulation.

With reference to Figures 4.3-5 through 8, the image and simulation both demonstrate the shifting of the peak polarization band that is orthogonal to the solar point (i.e., the anti-solar point). Again, saturation is evident in the vicinity of the sun. However, the sun, being an fully unpolarized source, would otherwise be represented as dark.

With reference to Figures 4.3-9 through12, the darkest pixels correspond to T values approaching +90°; the lightest pixels correspond to T values approaching -90°. The most significant deviation with these figures is due, unfortunately, to the color and gray scale representations of two different software programs (ENVI^{TM} and MathCAD^{TM}); the color

renderings provide better spatial correlation. However, the model is relatively insensitive to the rotational bias that was also simulated to coincide with the later three solar elevation collections.

With reference to Figures 4.3-13 through16, the abs(T) images clearly demonstrate the sensitivity of the imaging system to rotation error. The first abs(T) image provides an example of the bi-lateral symmetry that is expected for abs(T) values on hemispheres bisected by the principal plane.

The predominant feature in the image that demonstrates this symmetry is the dark (near-0°) areas opposing the hemisphere containing the sun. The presence of the polarimeter supports in the scene provides a source of reference for the detection of symmetry (or lack thereof).

With reference to Figures 4.3-17 through 20, both the images and their simulations have undergone a mathematical rotation with the appropriate bias applied, *via* atan(tan(T-bias)). The signficant feature of this rotation is the approximate restoration of bi-lateral symmetry for all four images.

The dark (near-0°) areas all demonstrate relative symmetry with respect to the polarimeter supports, as would be expected for polarization due to pure Rayleigh scattering under clear sky conditions.
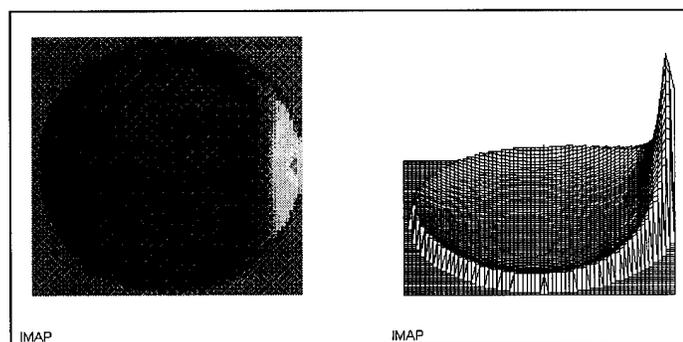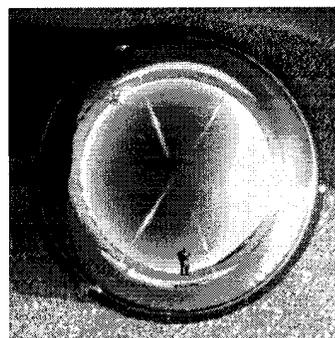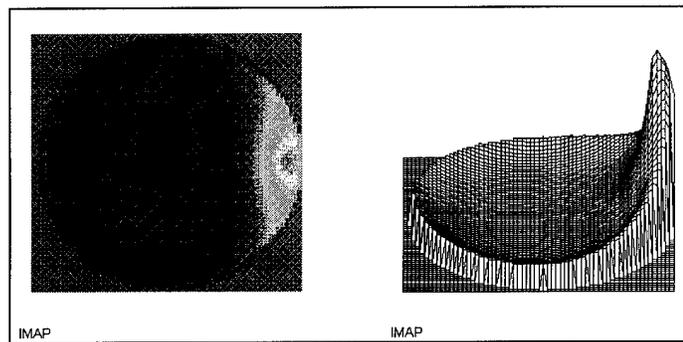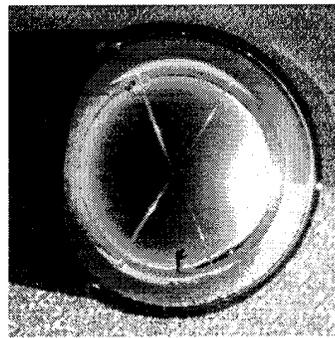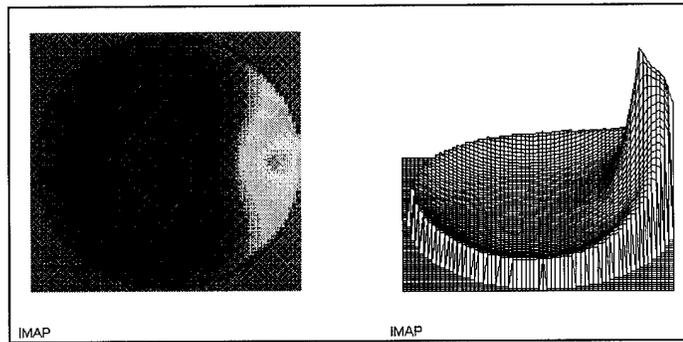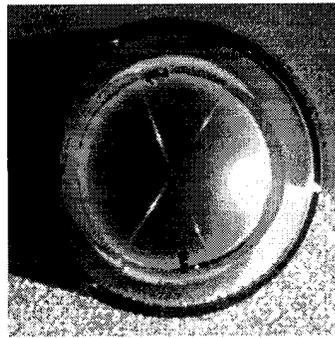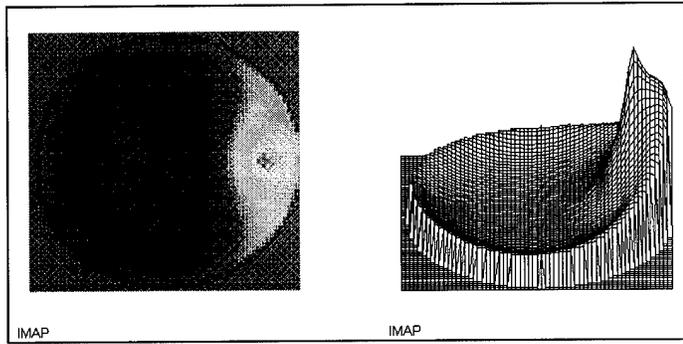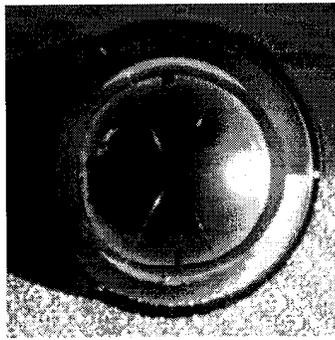
Figures 4.3-1 through 4 (a) and (b). I parameter images and their simulations for solar elevations 26.9°, 23.0°, 16.3°, and 7.9°, respectively.
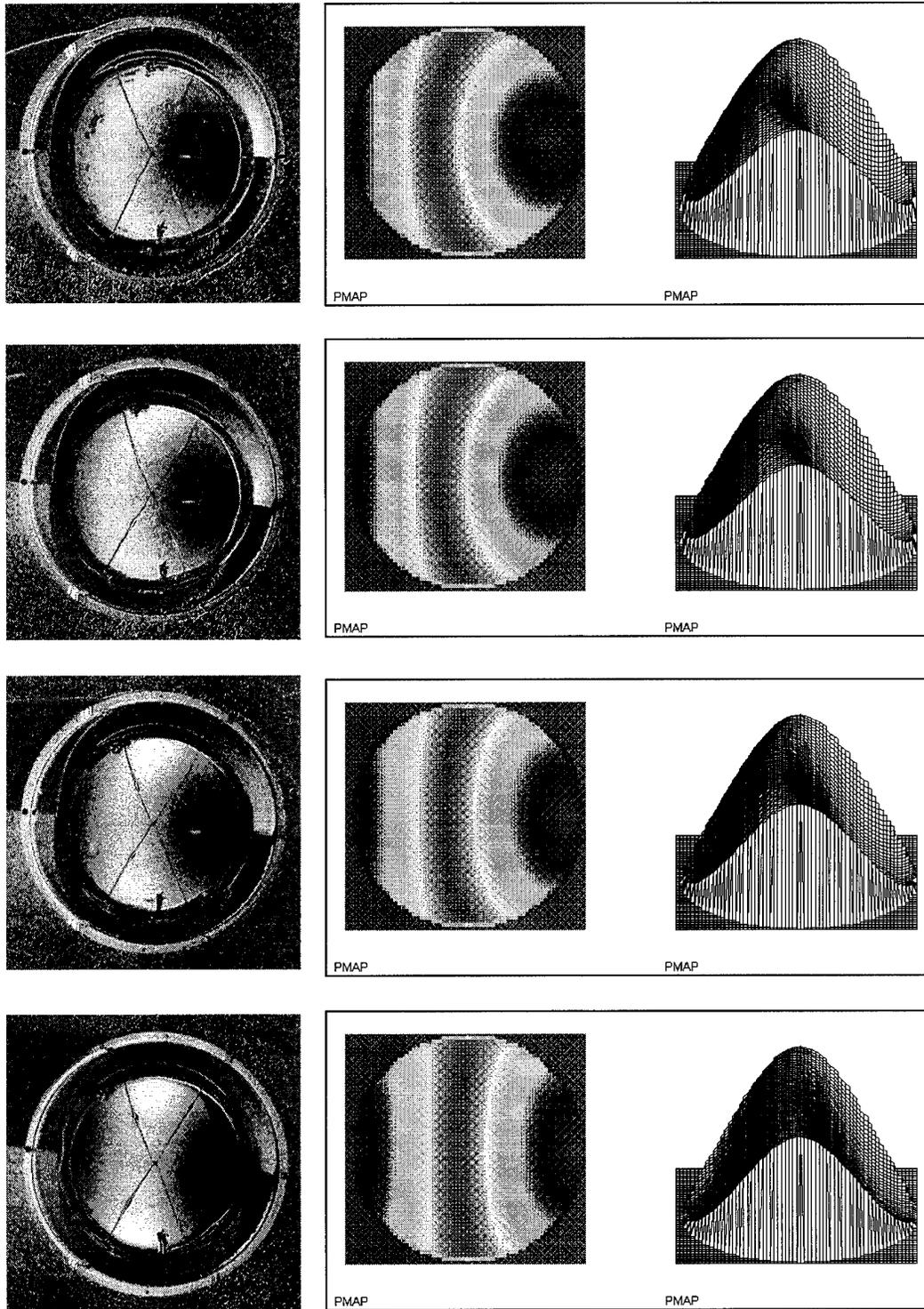
Figures 4.3-5 through 8 (a) and (b). P parameter images and their simulations for solar elevations 26.9°, 23.0°, 16.3°, and 7.9°, respectively.

111
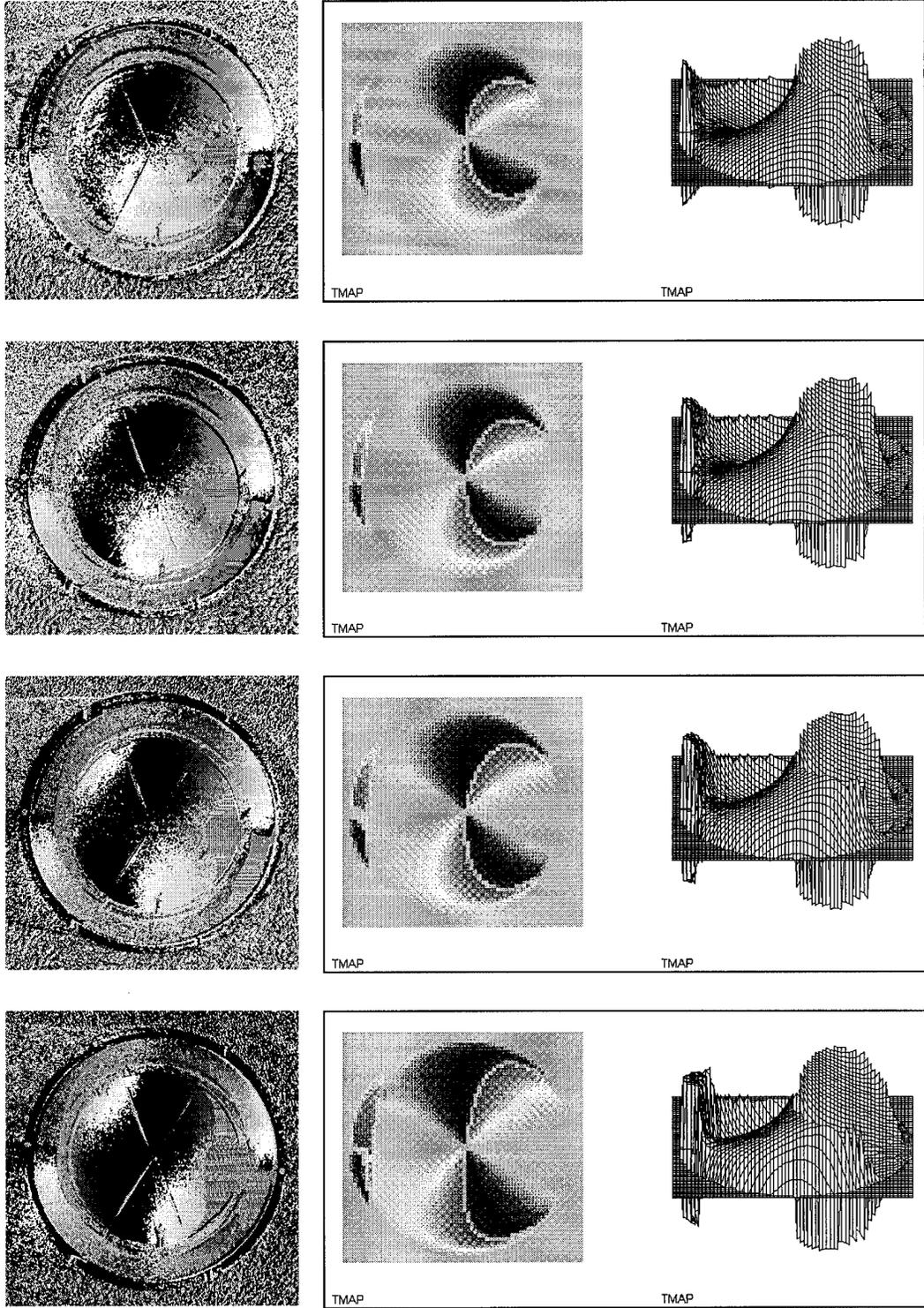
Figures 4.3-9 through 12 (a) and (b). T parameter images and their simulations for solar elevations 26.9°, 23.0°, 16.3°, and 7.9°, respectively.
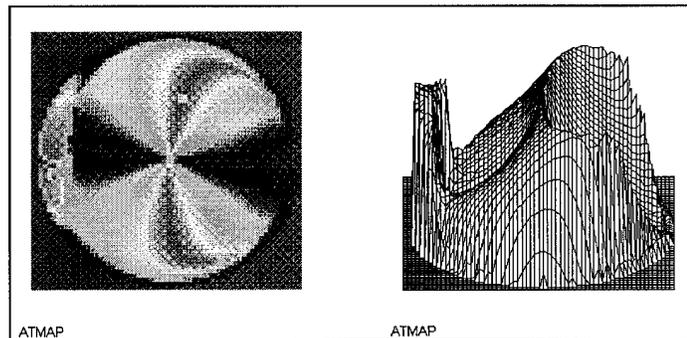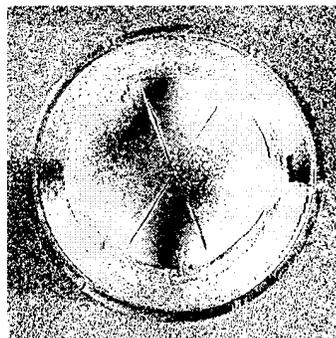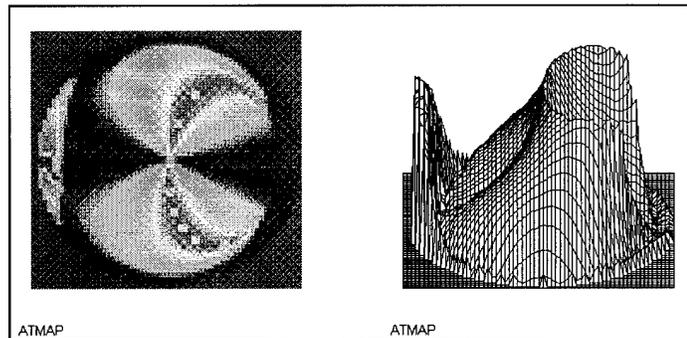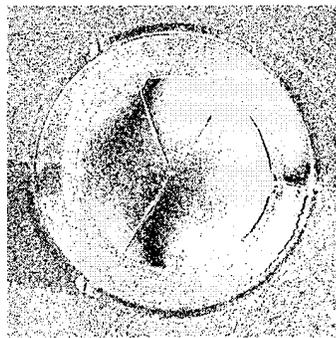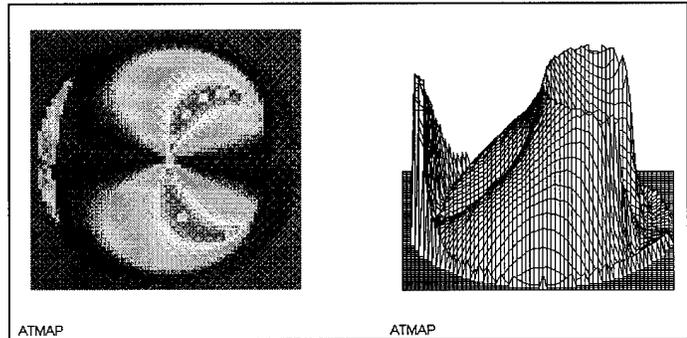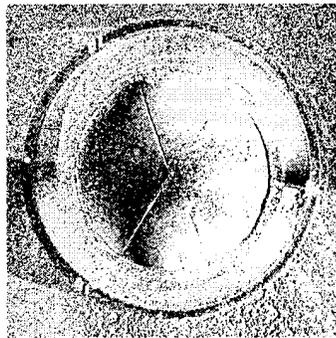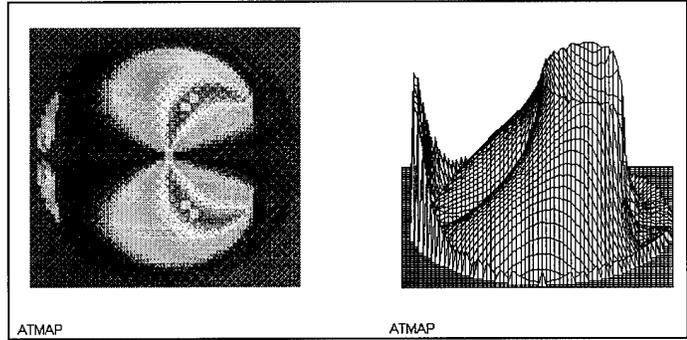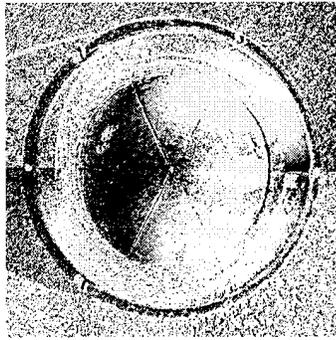
Figures 4.3-13 through 16 (a) and (b). Absolute value of T parameter images and their simulations for solar elevations elevations 26.9°, 23.0°, 16.3°, and 7.9°, respectively. Note the asymmetry of the spatial distributions of T compared with Figures 4.3-17 through 20.

113
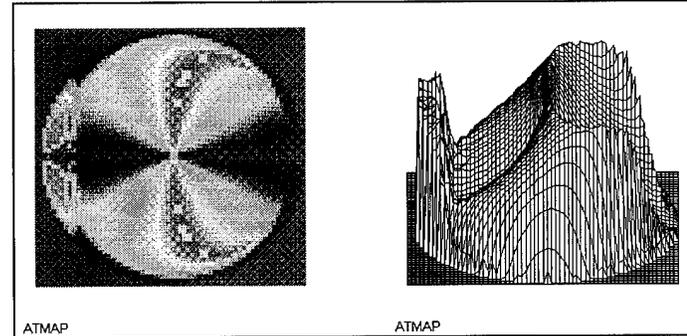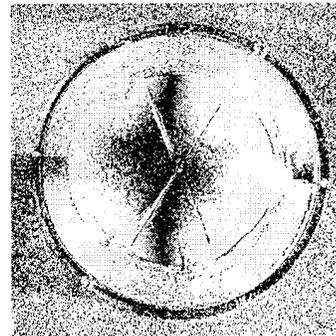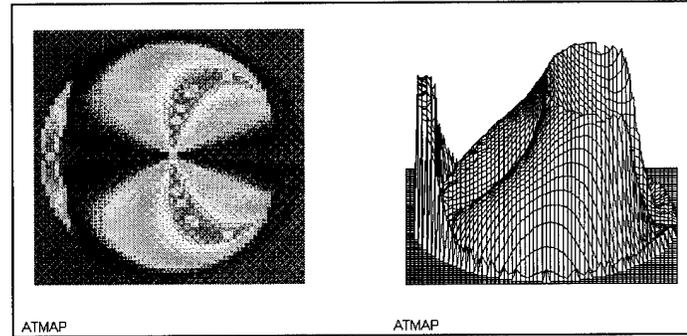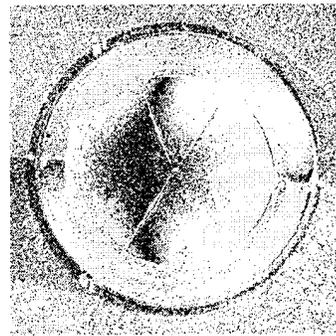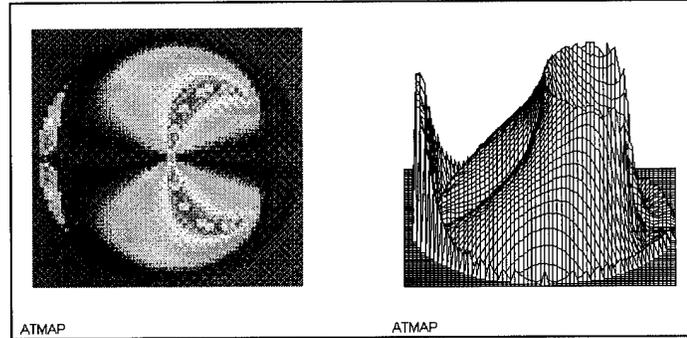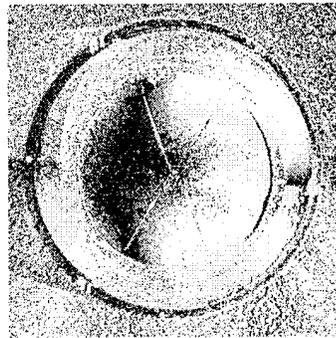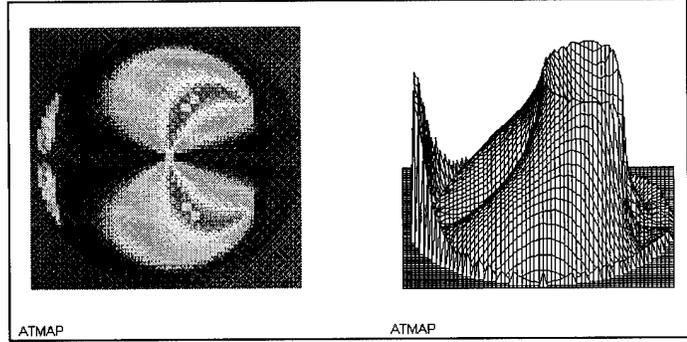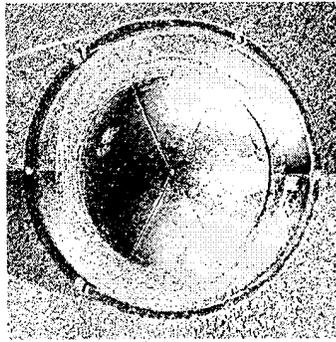
Figures 4.3-17 through 20 (a) and (b). Absolute value of T parameter images and their simulations after having a rotational bias of -1.4°, -5.9°, -5.6°, and -6.2° (respectively) applied to each pixel value, corresponding to the rotation error of the polarimeter relative to the principal plane. Note the symmetry of the spatial distributions of T compared with Figures 4.3-13 through 16.

Although unmodeled by the simulation, the mirror sub-scene difference images are presented as Figures 4.3-21 through 24. Within the context of potential spatial system calibration, these images provide insight into the underlying accuracy of the intensity measurements that were used to calculate the Stokes parameter images and their derivative images.

Although the in-field test scenes were relatively flat compared with the scale of focal distance, one observable instance of misregistration is evident in the D images: the largest deviations in the surface plots correspond to misregistrations of the 10-foot polarimeter supports from parallax effects created by the finite separation of the four apertures (55 mm between the two most distant lens centers). The effect is especially pronounced at the outer edges of the dome mirror where secondary reflection of the polarimeter supports enhanced the dispersion of their reflected images.
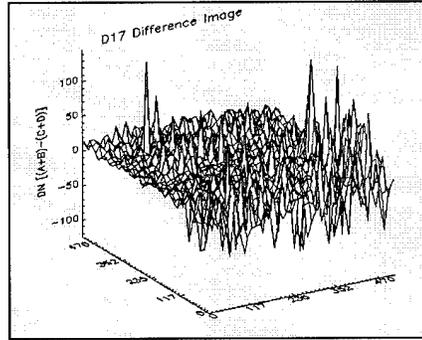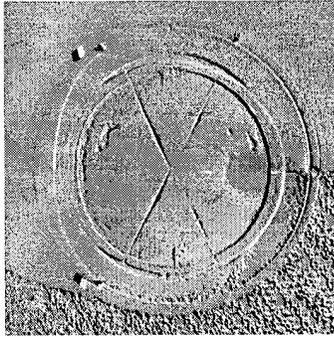
$\bar{x} = +7.8051$
$\sigma = 20.3882$
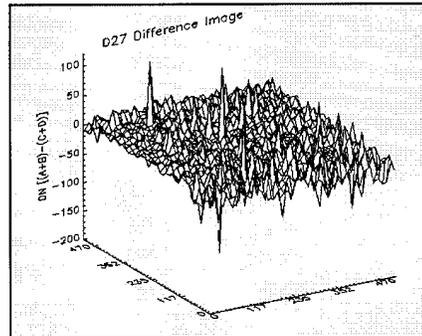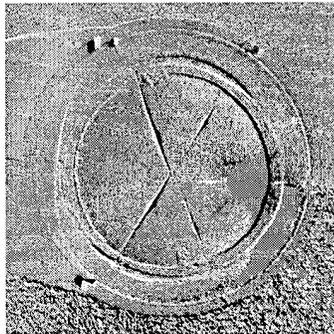
$\bar{x} = +3.7067$
$\sigma = 16.2365$
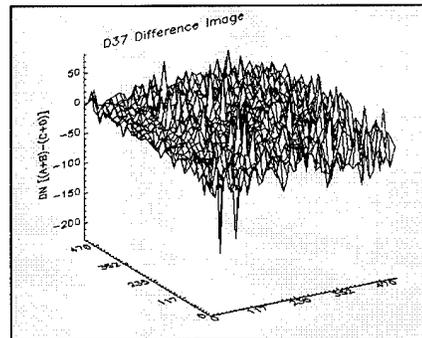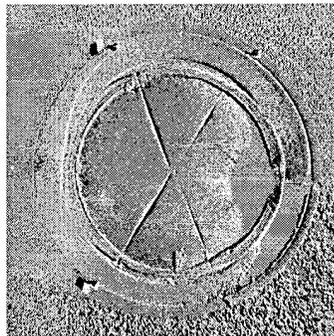
$\bar{x} = -0.5899$
$\sigma = 19.6861$
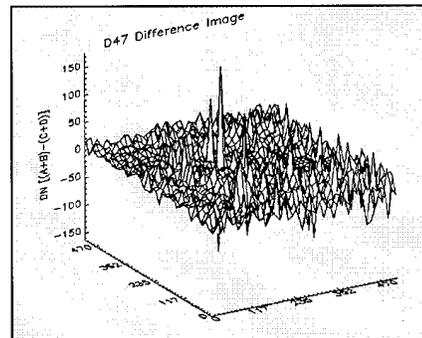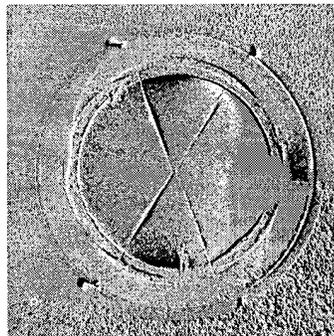
$\bar{x} = +3.3231$
$\sigma = 18.6854$

Figures 4.3-21 through 24 (a) and (b). D parameter images and surface plots. Average digital number and standard deviation is listed on the right. Note that the largest deviations correspond to misregistrations of the polarimeter supports from parallax effects created by the finite separation of the four apertures.

116

4.4 Aerial calibration results

General collection results

Twenty photo quads (40 35-mm frames) were collected between 1312 and 1548 EST on 03 Nov 1994. A summary of the collection and processing results is listed in Table 4-4.

Table 4-4
Collection and Processing Results Summary

Time EST	Ht ft	Az deg	Quad Nbr	Frame Nbrs	Remarks
1312	1000	045	1	16/--	water /*partially processed
1313	1000	045	2	-- /17	water /*partially processed
1314	500	090	3	18/--	water /*partially processed
1314	500	090	4	-- /--	water / unprocessed
1315	150	270	5	-- /--	water / unprocessed
1315	150	270	6	-- /--	water / unprocessed
1319	1000	unk	7	19/20	target of opportunity
1320	1000	unk	8	21/22	target of opportunity
1323	1000	unk	9	23/24	target of opportunity
1327	1000	unk	10	25/26	target of opportunity
1530	1000	045	11	-- /--	water / unprocessed
1530	1000	045	12	-- /--	water / unprocessed
1531	500	090	13	27/28	water / **processsed**
1532	500	090	14	-- /--	water / unprocessed
1533	150	270	15	-- /--	water / unprocessed
1533	150	270	16	-- /--	water / unprocessed
1536	1000	unk	17	30/31	target of opportunity
1538	1000	unk	18	32/33	target of opportunity
1545	1000	unk	19	34/35	target of opportunity
1548	1000	unk	20	36/37	target of opportunity

* Photo CD processing accepted one quad frame but rejected the other.

As previously mentioned in Chapter 4.1, the aerial collection experienced two failures as a direct result of photo CD processing. Because the contrast optimization algorithm was not disabled during

photo CD processing, the sensitometric step wedge was both distorted and incomplete, resulting in the loss of sensitometric calibration. Also, all but one of the 12 Hinckley reservoir collections were partially or totally rejected by the optimization algorithm for failure to meet a minimum threshhold for input contrast. The one quad that was fully processed exceeded the threshhold only because it contained a small amount of brighter land area with the otherwise dark waterwave surface in the scene, providing a range of contrast that was acceptable to the processing algorithm.

Due to the overall failure of the overwater collections, the one fully processed quad was used as a demonstration of feasibility for further aerial polarimetric imaging activities based upon its general agreement with the results of the in-field experiment. The most significant loss to this demonstration is the absence of sensitometric calibration.

However, there are several unique aspects of the one aerial collection that can still be evaluated. In particular, the relative homogeneity of the waterwave surface provides a basis for comparison of the spatial information content between contiguous sub-scenes. In this feasibility demonstration, one large (512 x 512 pixel) sub-image of the waterwave surface was subdivided into four 256 x 256 pixel contiguous patches. The sub-image statistics could then be compared under the assumption that the four sub-scenes represent four correlated realizations of the same underlying process, i.e., wind-driven waterwave generation.

Figures 4.4-1 through 4 depict the 512 x 512 pixel Stokes derivative sub-images. Again I is the unpolarized intensity image, P is the % polarization image, T is the image depicting the orientation angle of the polarization ellipse, and D is the difference image, representing I' - I".
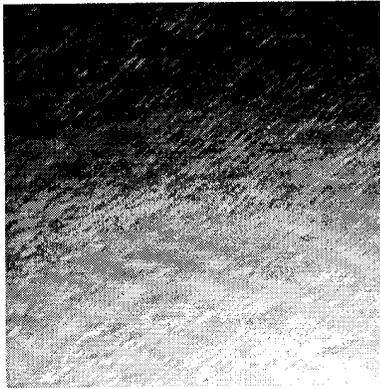
Figure 4.4-1. I sub-image.
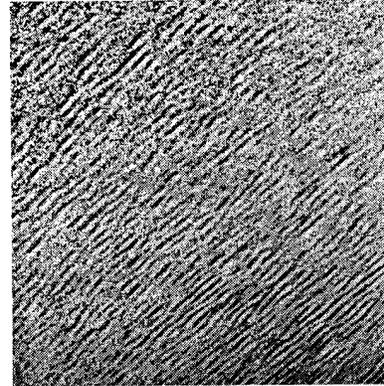
Figure 4.4-2. P sub-image.
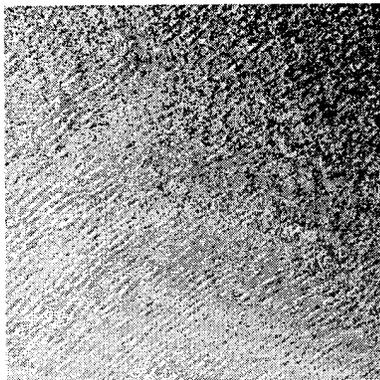
Figure 4.4-3. T sub-image.
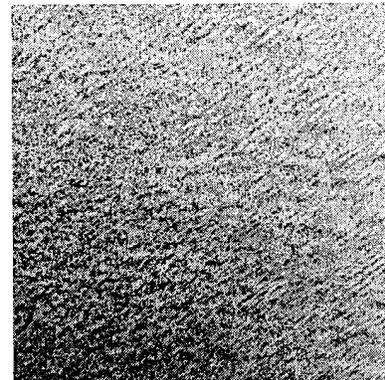
Figure 4.4-4. D sub-image.

Figure 4.4-5 illustrates the segmentation of the one 512 x 512 sub-image into four contiguous 256 x 256 pixel image patches.

```
Patch A        | Patch C
(256 x 256     | (256 x 256
pixels)        | pixels)
---------------|-----------------
Patch B        | Patch D
(256 x 256     | (256 x 256
pixels)        | pixels)
------------------------------------
Figure 4.4-5.
```

Histogram analysis of the difference (D) image

Figure 4.4-6 plots the four histograms for the uncalibrated difference (D) image patches.

119

D Histogram
(4 contiguous patches)
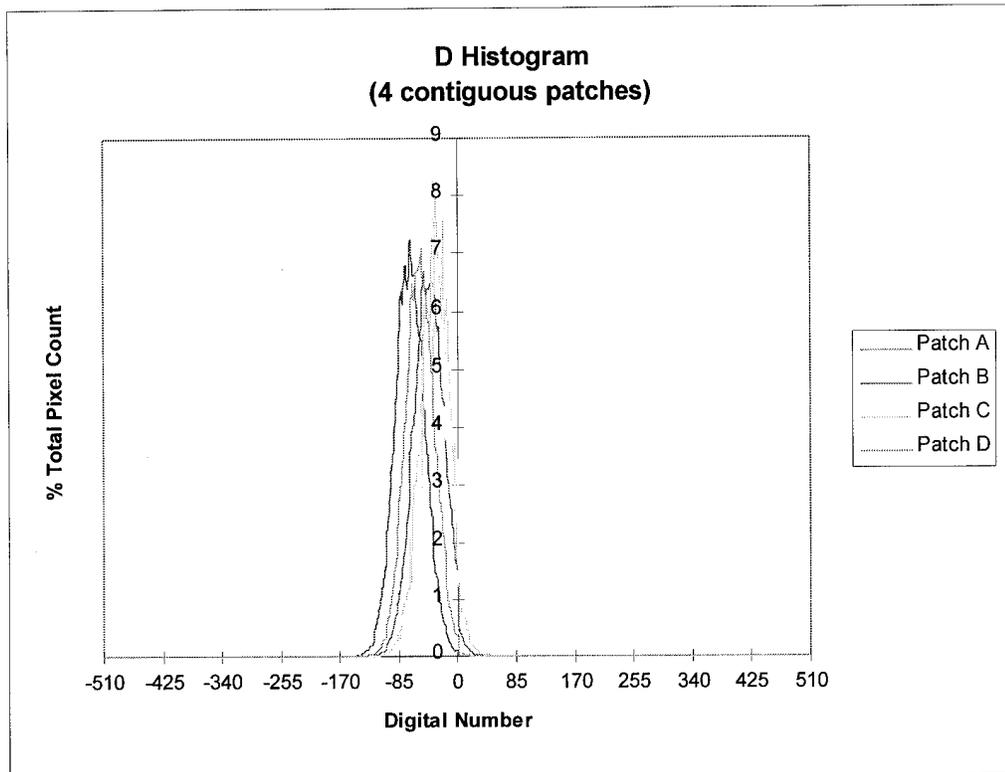
Figure 4.4-6.

In lieu of sensitometric calibration, this plot provides an indication of the magnitude of error that exists in the calculation of the Stokes parameters and Stokes derivatives.

The underlying statistics of the photo quad for the 512 x 512 sub-image and four 256 x 256 patches are presented in Table 4-5.

Table 4-5. Statistics Report				
Parameter	Min	Max	Mean	Std Dev
I (0°) (Subimage)	81.0	255.0	179.4123	38.7929
I (90°) (Subimage)	5.0	246.0	88.3622	25.6739
I (45°) (Subimage)	22.0	248.0	130.0861	35.9600
I (135°) (Subimage)	83.0	255.0	186.7682	38.5032
D (Subimage)	-173.0	124.0	-49.0798	26.3835
D (Patch A)	-147.0	55.0	-41.6093	22.7740
D (Patch B)	-173.0	25.0	-69.1875	21.8237
D (Patch C)	-148.0	124.0	-30.9919	22.8967
D (Patch D)	-146.0	34.0	-54.5306	21.1701

The most significant feature of the uncalibrated difference image patches is the strong negative bias, between -30 and -70 digital numbers (dn). These differences are systematic errors created by the absence of sensitometric calibration and the presence of photo CD contrast optimization. As will be seen in the T image data, the reference azimuth is in the vicinity of the principal plane. The high contrast between the I (0°) and I (90°) image patches bear out this fact.

However, the dn values for the I (45°) and I (135°) sub-images appear to be artificially elevated compared with the other cross-polarized pair and their expected conformance with the law of Malus: the mean for the I (45°) sub-image has an expected dn value of 109 and the mean for the I (135°) has an expected dn value of 158. But because this polarized pair has overall lower exposure intensity, contrast optimization applied a significant positive dn bias of +16% to the pair within the image frame and created a difference (D = I' - I") of 49 dn between the two cross-polarized pairs.

Another analytic feature of this uncalibrated data is the variation of the patch differences. Figure 4.4-4 illustrates the spatial distribution of

differences values across the four patches in the sub-image. Because the patch differences are all the product of a single contrast optimization application, they are created by differential contrast optimization applied to the pair within each frame. The effect of this non-linear optimization also modifies the calculation of Q and U, creating subsequent errors in the calculation of P and T.

In sum, the uncalibrated image has a systematic error of -9.6%. While this bias is over ten times the magnitude of the calibrated images, the only alternative is to reject this one remaining image from the aerial collection for lack of collateral sensitometric calibration data. A future option for consideration is to utilize known characteristic curves for similar histogram content and execute an iterative least squares correction of the photo quads on a pixel by pixel basis until the resulting difference image achieves an acceptable minimum. This type of correction is currently outside the range of ENVI processing capabilities; however, the merits of this option will be addressed in Chapter 5.

Histogram analysis of the unpolarized intensity (I) image

Figure 4.4-7 plots the four histograms for the uncalibrated intensity (I) image patches. In lieu of sensitometric calibration, this plot provides only an indication of relative intensities, with a known systematic error of between +15 and +35 dn in the I parameter calculation.

The underlying statistics of the uncalibrated 512 x 512 sub-image and four 256 x 256 patches are presented in Table 4-6.

I Histogram (uncalibrated)
(4 contiguous patches)

Figure 4.4-7.
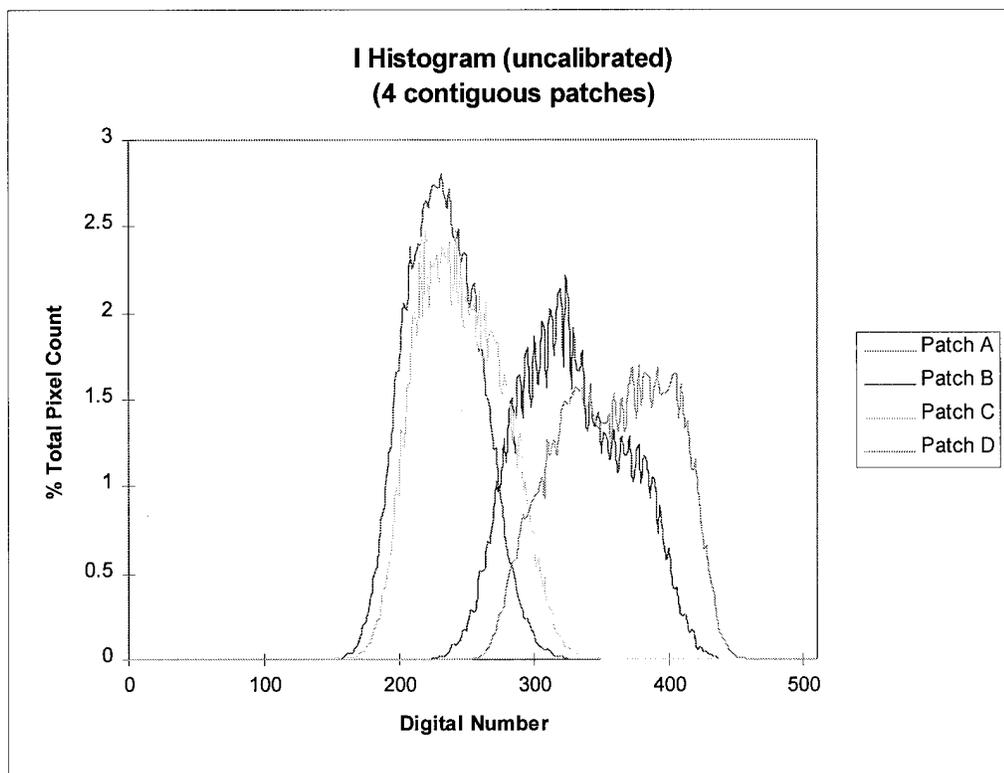
		Table 4-6.			
		Statistics Report			
Parameter	Min	Max	Mean	Exp. Mean	Std Dev
I (Subimage)	139.0	457.0	292.3145	267.7746	64.2228
I (Patch A)	143.0	335.0	233.2161	212.4115	27.0159
I (Patch B)	210.5	445.5	329.4756	294.8819	39.4741
I (Patch C)	139.0	368.0	246.4961	231.0002	30.8259
I (Patch D)	248.0	457.5	360.0700	332.8047	41.1861

The figure and table again illustrate the large variation of I relative to P and T; in this example, the inter-patch standard deviation is about 62 dn, comparable to the full subimage standard deviation. If the expected

means are used as estimates of the calibrated I means, the inter-patch standard deviation decreases by only 6 dn, to 56 dn.

Figure 4.4-1 illustrates the presence of strong solar reflection in Patches B and D, providing strong contrasts to Patches A and C and also providing an explanation for the non-systematic inter-patch variation. While the strong reflection of sunlight is an inadvertant byproduct of yet another camera orientation error, deviations from a non-level platform (errors in omega or phi, refer to Figure 4.1-1), it provides a more dramatic comparison with the relative stability of the P and T images and their spatial spectra.

Histogram analysis of the % polarization (P) image

Figure 4.4-8 plots the four histograms for the uncalibrated % polarization (P) image patches. In lieu of sensitometric calibration, this plot provides only an indication of approximate polarizations, with an unknown systematic error in the P parameter calculation due to the non-linearity of differential contrast optimization.

The underlying statistics of the uncalibrated 512 x 512 sub-image and four 256 x 256 patches are presented in Table 4-7.

The figure and table illustrate the small variation of P relative to I; in this example, the inter-patch standard deviation is 2.43 %, less than one third of the subimage standard deviation. Also, the intra-patch standard deviations are comparable with the subimage standard deviation. However, the P data exhibits the same spatial trend visible in the mirror-reflected skydome image, consistent with the observation that the water

P Histogram (uncalibrated)
(4 contiguous patches)
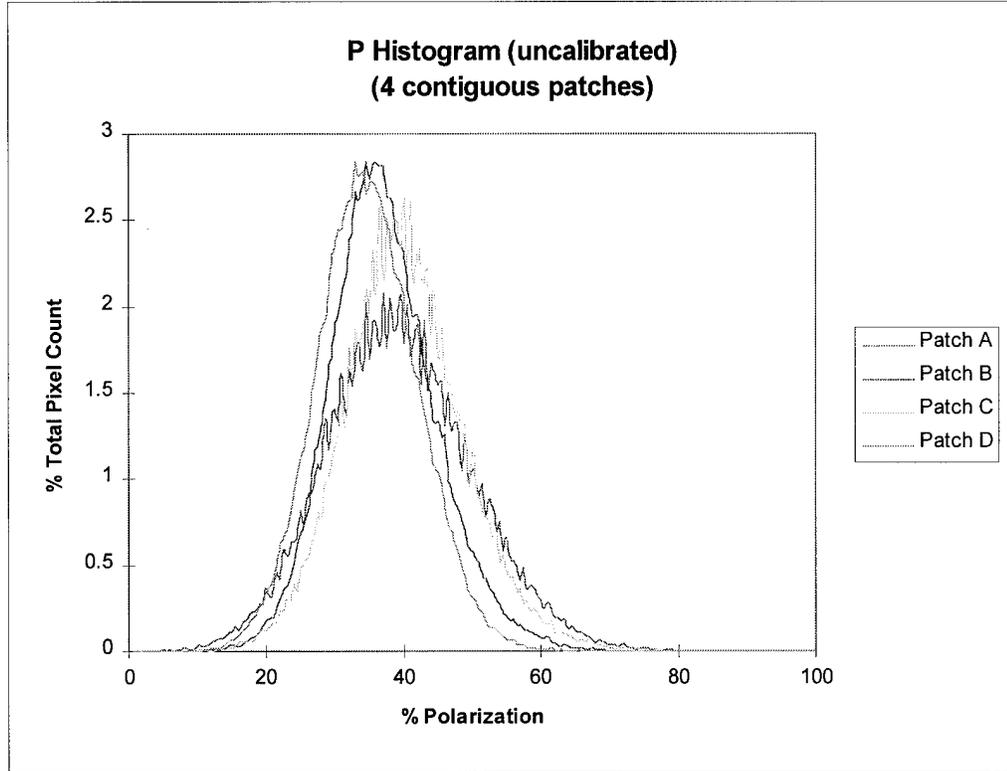
Figure 4.4-8.

| | Table 4-7. | | | |
| | Statistics Report | | | |
Parameter	Min	Max	Mean	Std Dev
P (Subimage)	1.99	92.32	37.99	8.92
P (Patch A)	1.99	92.14	39.54	10.57
P (Patch B)	6.17	74.33	37.26	7.72
P (Patch C)	3.93	92.32	40.27	8.72
P (Patch D)	6.98	69.94	34.90	7.32

surface represents a quasi-Gaussian distribution of reflecting surface facets that reflect a smaller solid angle portion of the skydome relative to the full coverage of the dome mirror.

Figure 4.4-2 illustrates the spatial distribution of P with the presence of lower values in the vicinity of the solarization area in Patches B and D and higher values in Patches A and C away from the area of solar reflection.

125

Consistent with the skydome reflection results and the simulation model results of Chapter 4.3, reflected P values are minimum at the point of direct sun reflection and maximum in the area of antisolar point reflection.

Histogram analysis of the orientation angle (T) image

Figure 4.4-9 plots the four histograms for the uncalibrated orientation angle (T) image patches. In lieu of sensitometric calibration, this plot provides only an indication of approximate angles, with an unknown systematic error in the T parameter calculation again, as with P, due to the non-linearity of differential contrast optimization.
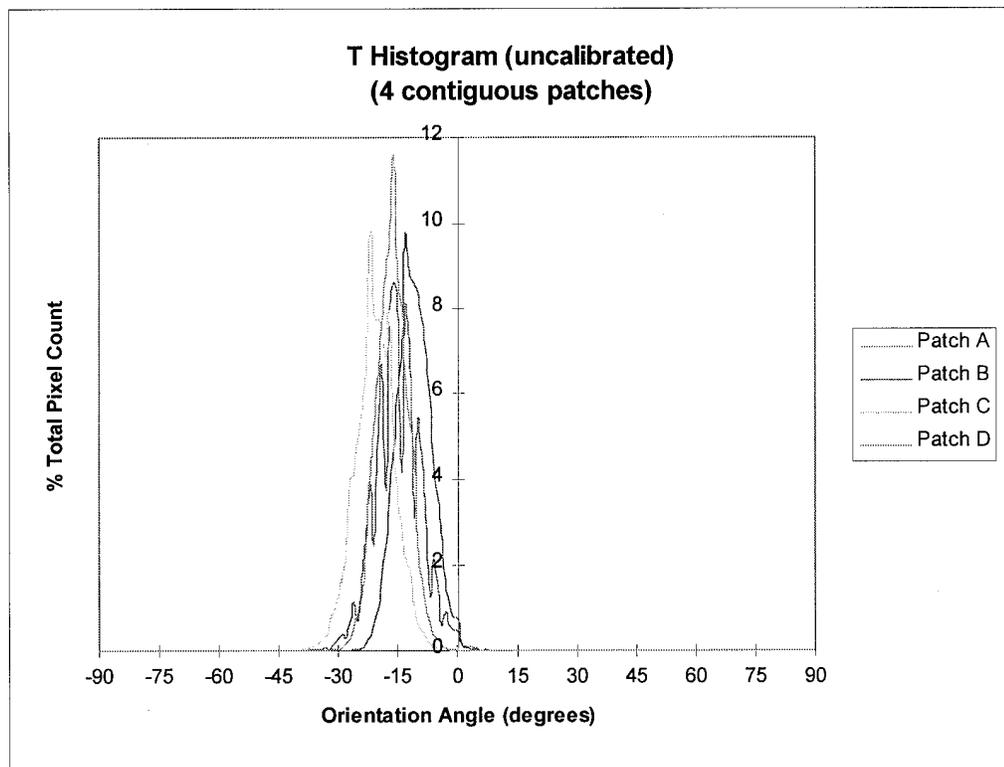
Figure 4.4-9.

The underlying statistics of the uncalibrated 512 x 512 sub-image and four 256 x 256 patches are presented in Table 4-8.

| Table 4-8. Statistics Report				
Parameter	Min	Max	Mean	Std Dev
T (Subimage)	-82.62	65.99	-16.06	6.00
T (Patch A)	-82.62	65.99	-15.12	5.84
T (Patch B)	-32.97	16.94	-11.33	4.46
T (Patch C)	-61.43	18.31	-21.02	5.02
T (Patch D)	-39.06	10.28	-16.77	4.06

The figure and table illustrate, as with P, the small variation of T relative to I; in this example, the inter-patch standard deviation is 4.02°, less than two thirds the subimage standard deviation. Also, the intra-patch standard deviations are again comparable with the subimage standard deviation. However, the T data exhibits the same spatial trend visible in the mirror-reflected skydome image, consistent with the observation that the water surface represents a quasi-Gaussian distribution of reflecting surface facets that reflect a smaller solid angle portion of the skydome.

Figure 4.4-3 illustrates the spatial distribution of T. The flight azimuth and hence polarizer reference for this collection was approximately 90° (due East). The apparent position of the water-reflected sun in the image is approximately WSW. Therefore, the polarizer reference plane is oriented from the principal plane by the approximate azimuth angle of -16° as calculated from the mean of the T subimage. This value compares closely with the T calculation using the photo quad means in Table 4-5:

$$\bar{T} = 0.5\tan^{-1}\frac{\bar{U}}{\bar{Q}} = 0.5\tan^{-1}\left[\frac{(130.0861 - 186.7682)}{(179.4123 - 88.3622)}\right] = -15.95° \qquad \boxed{\text{Equation 4-5}}$$

Patch D is closest to the location of the solar reflection point and, as a result, contains the more even distribution of positive and negative T

values: the principal plane roughly bisects the patch from the bottom right corner of the patch and runs through the top right corner of Patch A. T values in Patch B are more positive than the mean, consistent with water surface facets reflecting the polarized skydome from one side of the principal plane; conversely, values in Patch C are more negative than the mean, consistent with water surface facets reflecting the polarized skydome from the other side of the principal plane. Patch A is slightly less positive than Patch B since the principal plane traverses it.

Consistent with the polarizer orientation error correction applied in Chapter 4.3, the -16° bias can also be removed from this image through the same process. Figure 4.4-10 and Table 4-9 show the effects of this mathematical rotation of the orientation angle of the polarization ellipse. In particular, the means and distributions of Patches D and A are nearly centered on zero while the means and distributions of Patches B and C are biased positive and negative by roughly equal amounts, respectively.

One additional observation in Figures 4.4-9 and 10 is the absence of artifact spikes in the T histograms: saturated dn values do exist in small numbers but, from Table 4-5, it is apparent that they do not occur together in either polarized pair. Therefore, the values of Q or U that are zero and near-zero occur in proportion with the rest of the histogram distribution.

T Histogram (corrected)
(4 contiguous patches)

Legend:
- Patch A
- Patch B
- Patch C
- Patch D

Y-axis: % Total Pixel Count
X-axis: Orientation Angle + 16.1 (degrees)
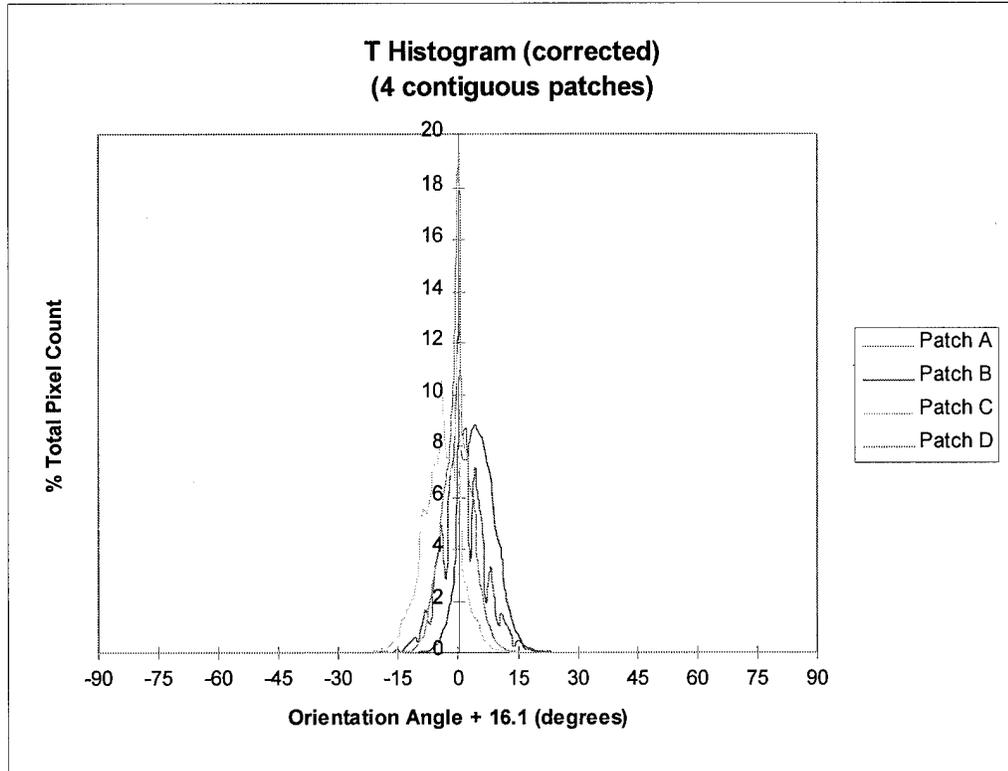
Figure 4.4-10.

Parameter	Min	Max	Mean	Std Dev
Table 4-8. Statistics Report				
T (Subimage)	-65.86	82.76	+0.71	6.00
T (Patch A)	-65.86	82.76	+1.65	5.84
T (Patch B)	-16.20	33.71	+5.44	4.46
T (Patch C)	-44.66	35.08	-4.25	5.02
T (Patch D)	-22.29	27.05	+0.00	4.06
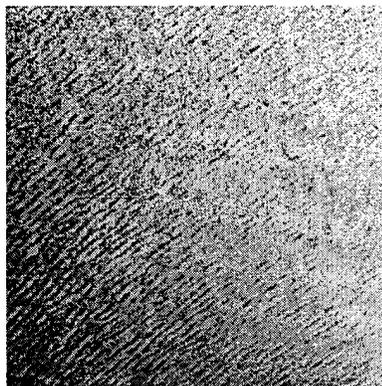
Figure 4.4-12. Abs(T) image.
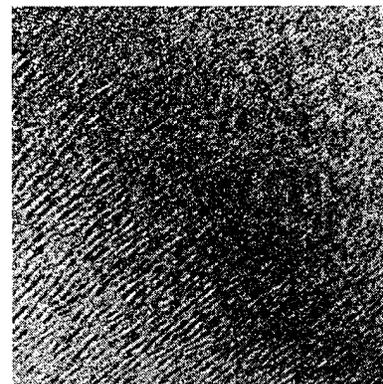
Figure 4.4-11. Abs(T + bias) image.

129

As in Chapter 4.3, Figures 4.4-11 and 12 illustrate the absolute value of T before and after the addition of the bias correction. Again, the dark pixels correspond to surface facets with azimuths oriented so that light is reflected from the principal plane where T is near 0°; and lighter pixels correspond to surface facets with azimuths increasingly oriented away from the principal plane. The rotated image of Figure 4.4-12 correlates favorably with the sun glint pattern in Figure 4.4-1, providing a secondary indication of the reflected principal plane.

In the absence of multiple and calibrated waterwave images, the remainder of the analysis of the one uncalibrated image falls within the description of a feasibility demonstration. In Chapter 4.5, the power spectral densities (PSDs) of the four patches were evaluated for their stability and compared with the results of the in-field experiment. While the in-field PSD stability analysis evaluates the imaging geometry effects on a fully deterministic surface, the aerial PSD stability analysis evaluates four contiguous spatial realizations of a surface that is nondeterministic but has underlying spatial structure that can be correlated.

4.5 Spatial analysis results

Introduction

A key motivation for examining the spatial attributes of polarimetric imagery was to compare the relative spatial spectral stabilities of polarimetric imagery with unpolarized imagery, recognizing that the stable estimation of spatial spectra is important to the full characterization of the surface texture and reflection geometry underlying the spatial radiance distributions reaching a sensor. Chapter 2.3 described several earlier studies that evaluated the spatial spectra from unpolarized imagery of correlated scenes. These results describe the stablity of those unpolarized spatial spectral estimates in comparison with polarimetric estimates.

In-field results

The spatial spectral stabilities of the three polarimetric components, I (unpolarized intensity), P (% polarization), and T (orientation angle), were analyzed with respect to a limited parametric surface exploration of imaging geometry: the four scene azimuths and four solar elevations.

The calibration analysis of the test panels in Chapter 4.2 indicated that the lighter of the two panels suffered a significant amount of digital number (dn) saturation, creating artifacts in the T histogram that also distorted the calculation of the T variances; the saturation would also artificially lower P values since Q and U are near zero. Since the power spectral density (PSD) analysis is effectively an evaluation of the spatial frequency distribution of variance, further PSD analysis of the lighter panels was rejected in favor of the darker panels. The histograms of the

darker panels were centered within the linear dn range and the resulting statistical analysis was not affected by dn saturation.

Figures 4.5-1 through 6 illustrate the sequence of spectral analysis as described in Chapter 3.4.

The polarimetric component images in Figures 4.5-1 through 3 (a) are rotated, fast Fourier transformed (FFT), and the FFT squared to produce power spectral densities (PSDs) (in Figures 1-3 (b)) having the same azimuth orientation relative to Scene 3.

The PSDs are combined for each imaging geometry parameter (scene azimuth and solar elevation) to calculate the average PSD (Figures 4.5-4 through 6 (a)) for each imaging geometry combination. The absolute differences between the average PSD and the individual PSDs that formed the average are themselves averaged and then normalized with respect to the average PSD variance. This spatial spectrum is the averaged difference PSD (ADP). The advantage of ADP analysis is that the spatial frequency components sum to a value that represents a percentage of the total variance of the average PSD. This value, the integrated difference variance (IDV), is a single statistic that indicates the amount by which a group of PSDs differ from each other; it can exceed 100%. The ADP normalization allows direct comparison of spectra with variances expressed in dissimilar units, in this case, dn units for I, % polarization for P, and degrees for T. The variances of a group of images may exhibit a large amount of intra-group variation but exhibit small IDVs since it is the spatial frequency distribution of relative variation (effectively the shape of the PSDs) that is being measured and not absolute variation. IDV, in sum, is an unbiased estimator of PSD stability.
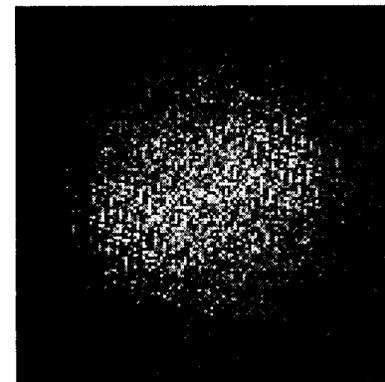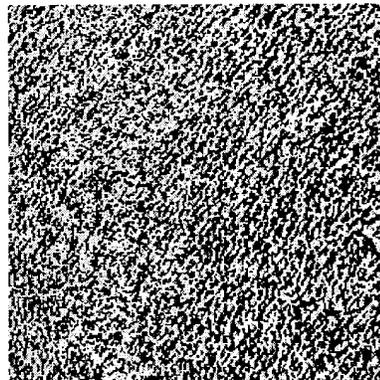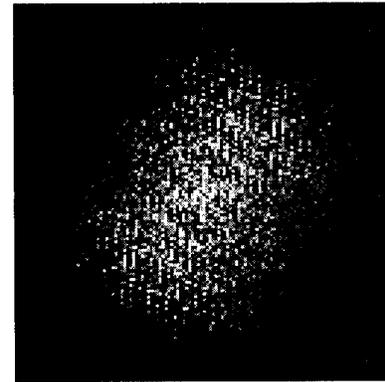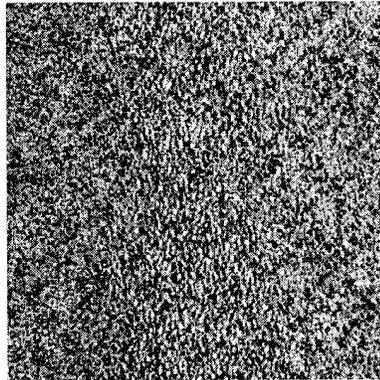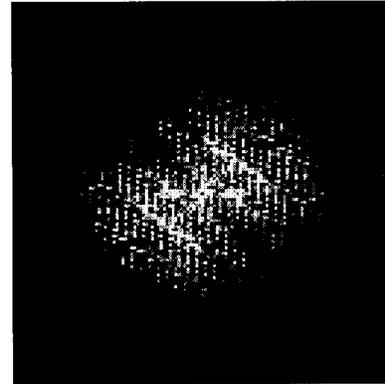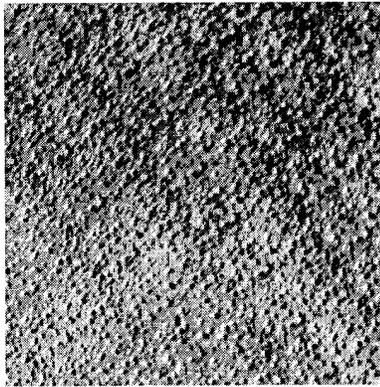
Figures 4.5-1 through 3 (a) and (b). I, P, and T component images and their power spectral densities (PSDs) for Scene 5 & Elevation 4. Note that the PSDs have been rotated (in this case by +45°) so that the PSDs for each scene can be analyzed with respect to a normalized orientation. Also note that the underlying spectral components of the 'cracked ice' texture are clearly visible in all three PSDs even though the texture is apparently lost in the P and T component images.
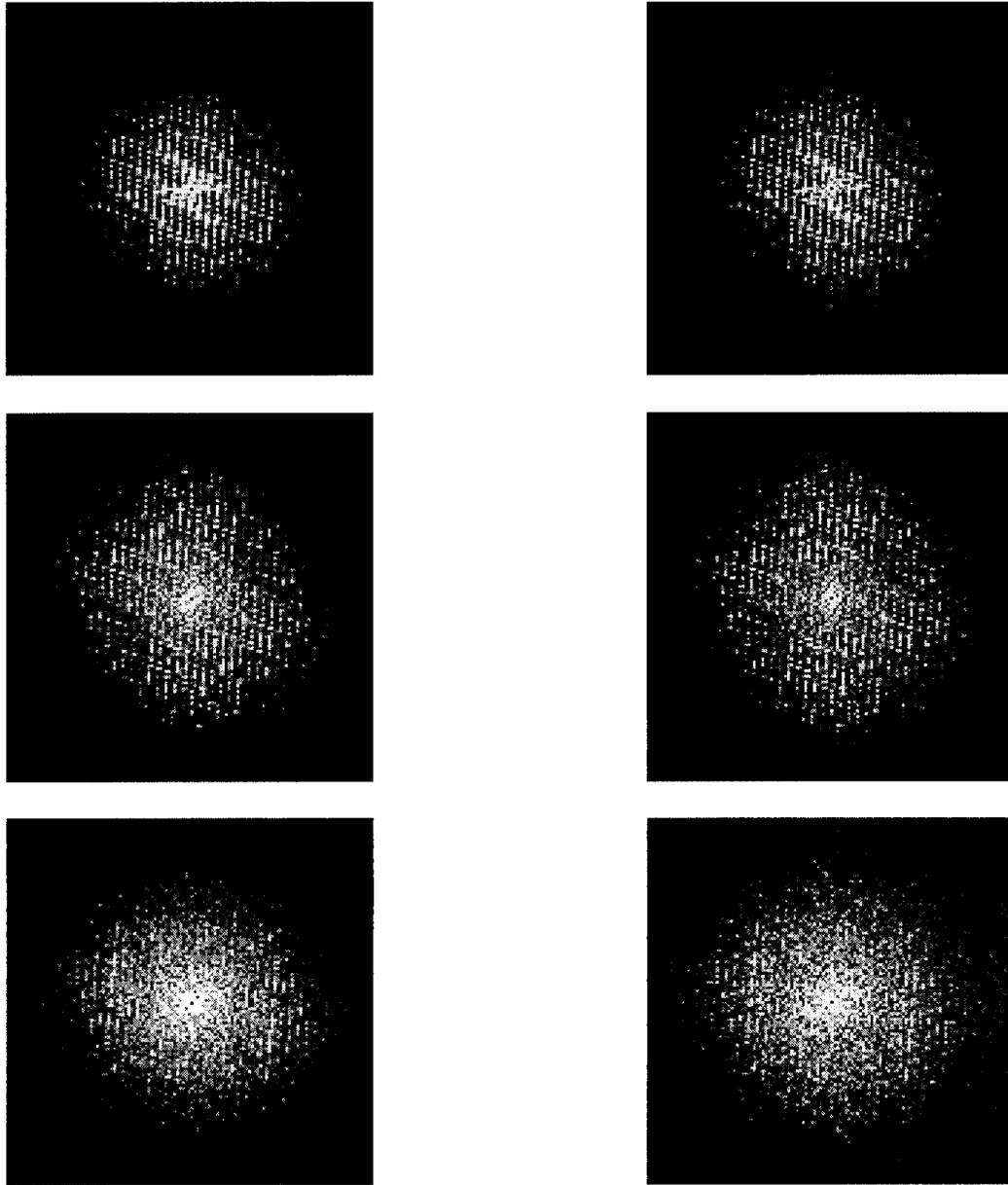
Figures 4.5-4 through 6 (a) and (b). I, P, and T component average PSDs and their average difference PSDs (ADPs) for Solar Elevation 1. The ADPs are normalized to the integrated variance of the average PSD and represent the fractional difference variance relative to the average PSD at each spatial frequency. The ADP representations here were rescaled in order to preserve contrast in the figures.

Because of several limitations in the analytic capabilities of ENVI (discussed in Chapter 3.4), fractional IDVs were calculated using the ADP histograms. The most significant limitation was the quantization (binning) of the difference variances during histogram generation and consequent aggregation of the smallest (but most numerous) difference variances in the lowest bin. The information loss due to aggregation can be mitigated by setting the integration threshhold above the lowest bin (containing the largest expected error) but the calculated fractional IDV is still only approximate because of the remaining quantization errors. For this reason, several threshholds for difference variance (dVar) were used in the calculation of fractional IDV in order to provide at least a qualitative assessment of the validity of this approach.

Figures 4.5-7 through 9 plot the fractional IDVs for different scene azimuths at dVar threshholds of 0.10%, 0.05%, and 0.02%.

Figures 4.5-10 through 12 plot the fractional IDVs for different solar elevations at dVar thresholds of 0.10%, 0.05%, and 0.02%.

The IDV values used in the plots are tabulated in Table 4-10.

The most general observation is that the fractional IDV values appear to preserve relative trends in the comparison of the three dVar threshholds but, particularly, in the comparison of the two lowest dVar threshholds. This observation provides some validation for the fractional IDV approach, in that the presence of increasing quantization errors would otherwise accumulate during progressive integrations and disturb the relative trends.

With reference to Figures 4.5-7 through 9, the IDVs for the three polarimetric components I, P, and T demonstrate a very clear distinction of the relative stabilities of their PSDs on the order of factors 2 to 3: the IDVs for P are approximately one half the IDVs of I, and the IDVs for T are between one third and one half the IDVs of P. This result is remarkable in consideration of the fact that P and T images are the product of ratios that would, and do, exhibit increased high spatial frequency content, similar to random noise, and increase the expected IDV. However, if this content is below the threshhold for dVar, it is effectively filtered out in this fractional IDV calculation. But, more robust spectral analysis techniques to calculate IDV would otherwise set an upper spatial frequency threshhold and treat the excluded high frequency variance as noise. The net result appears to be the same. A more robust IDV measurement technique is proposed in Chapter 5.

With reference to Figure 4.5-9 alone, the IDVs for both P and T are within 1% to 2%, indicating that their PSDs are relatively insensitive to changes in scene azimuth. While the 2-4% variation in IDVs for I may not be statistically significant, the apparent trend does correlate with the prediction results of both Chapman and Irani [1981] and North [1989]: Scene 3 represents the case where the dominant spectral components are in parallel with the principal plane, resulting in maximum errors for spatial spectrum estimation; Scene 5 has the dominant spectral components orthogonal to the principal plane, resulting in minimum errors for spectrum estimation; and Scenes 2 and 4 are have the dominant components both 45° to either side of the principal plane, resulting in errors that are approximately equal and midway between the maximum and minimum errors.
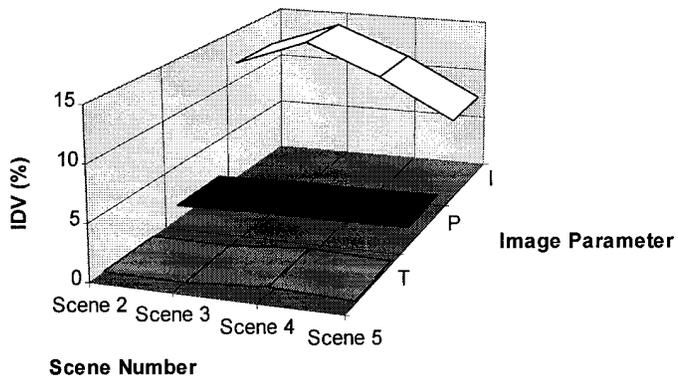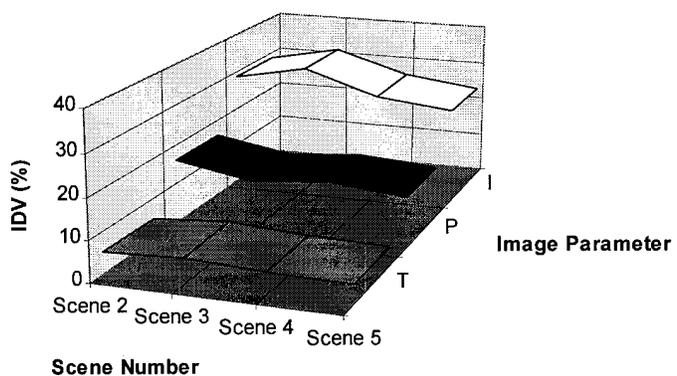
Figure 4.5-7 through 9. Integrated Difference Variance (IDV) plots by scene azimuth for difference variance (dVar) threshholds of 0.10%, 0.05%, and 0.02%.

137
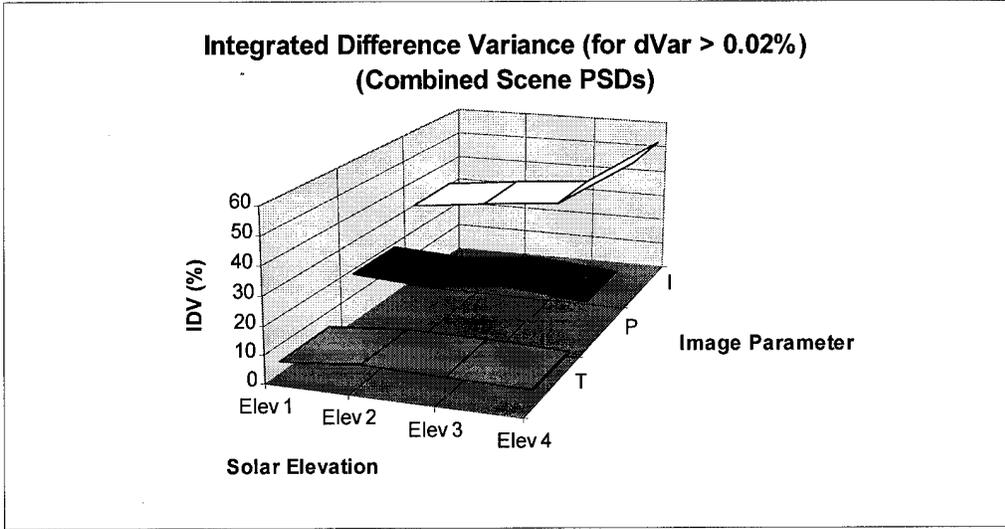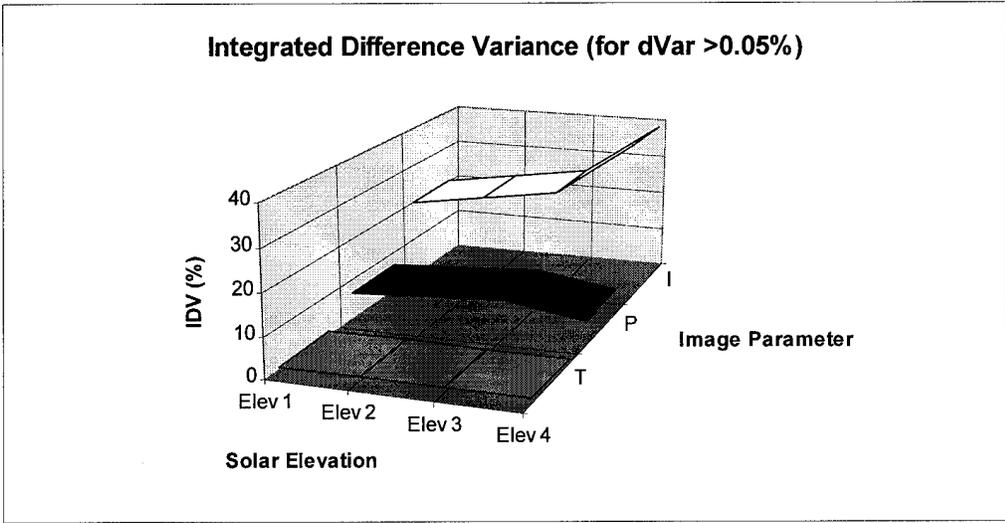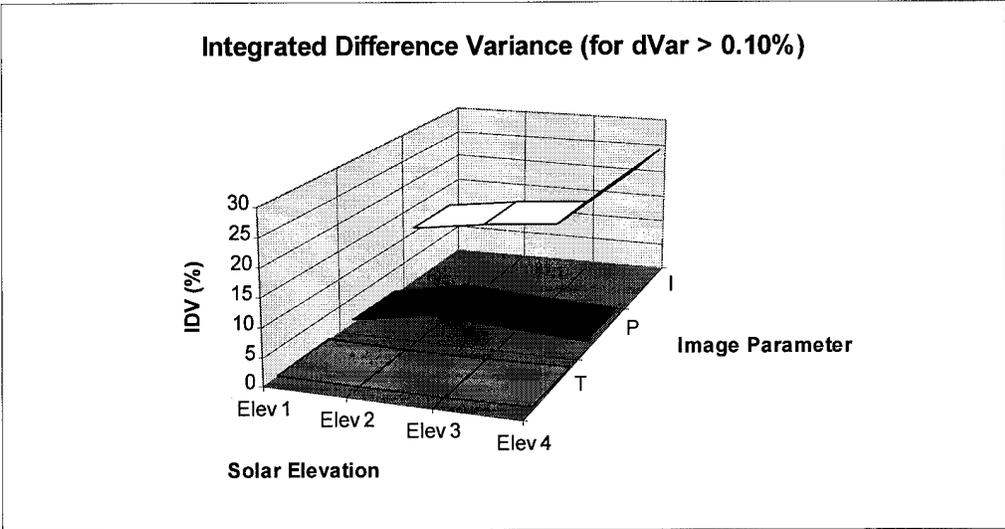
Figure 4.5-10 through 12. Integrated Difference Variance (IDV) plots by solar elevation for difference variance (dVar) threshholds of 0.10%, 0.05%, and 0.02%.

With reference to Figures 4.5-10 through 12, the IDVs for the three polarimetric components I, P, and T again demonstrate the same clear distinction of relative stabilities of their PSDs. The IDVs for both P and T again show relative insensitivity, this time to changes in solar elevation. However, for increasing solar elevation, the I parameter IDVs clearly demonstrate a trend toward increasing instability in PSD estimation. The predominant effect in the imagery is the presence of significant shadowing that increases image contrast by emphasizing low spatial frequency changes in panel elevation and obscuring high spatial frequency content. However, the reflected radiance from the same shadowed areas is more polarized than the directly illuminated areas since the source of incident radiance comes from the vicinity of the antisolar area of the skydome, which is the most highly polarized part of the clear sky. In this situation, the higher spatial frequency content is preserved in the P and T images, resulting in stabler estimates of their PSDs relative to the I component.

Aerial results

The spatial spectral stabilities of the three polarimetric components, I, P, and T, were analyzed with respect to a composite of four spatially contiguous realizations (subimage patches) of a waterwave scene contained within a single image.

As with the in-field analysis described above, Figures 4.5-13 through 16 illustrate the sequence of spectral analysis as described in Chapter 3.4 for the aerial imagery. Figure 4.5-17 plots the fractional IDVs at dVar thresholds of 0.10%, 0.05%, and 0.02%. The IDV values used in this plot are tabulated in Table 4-10.
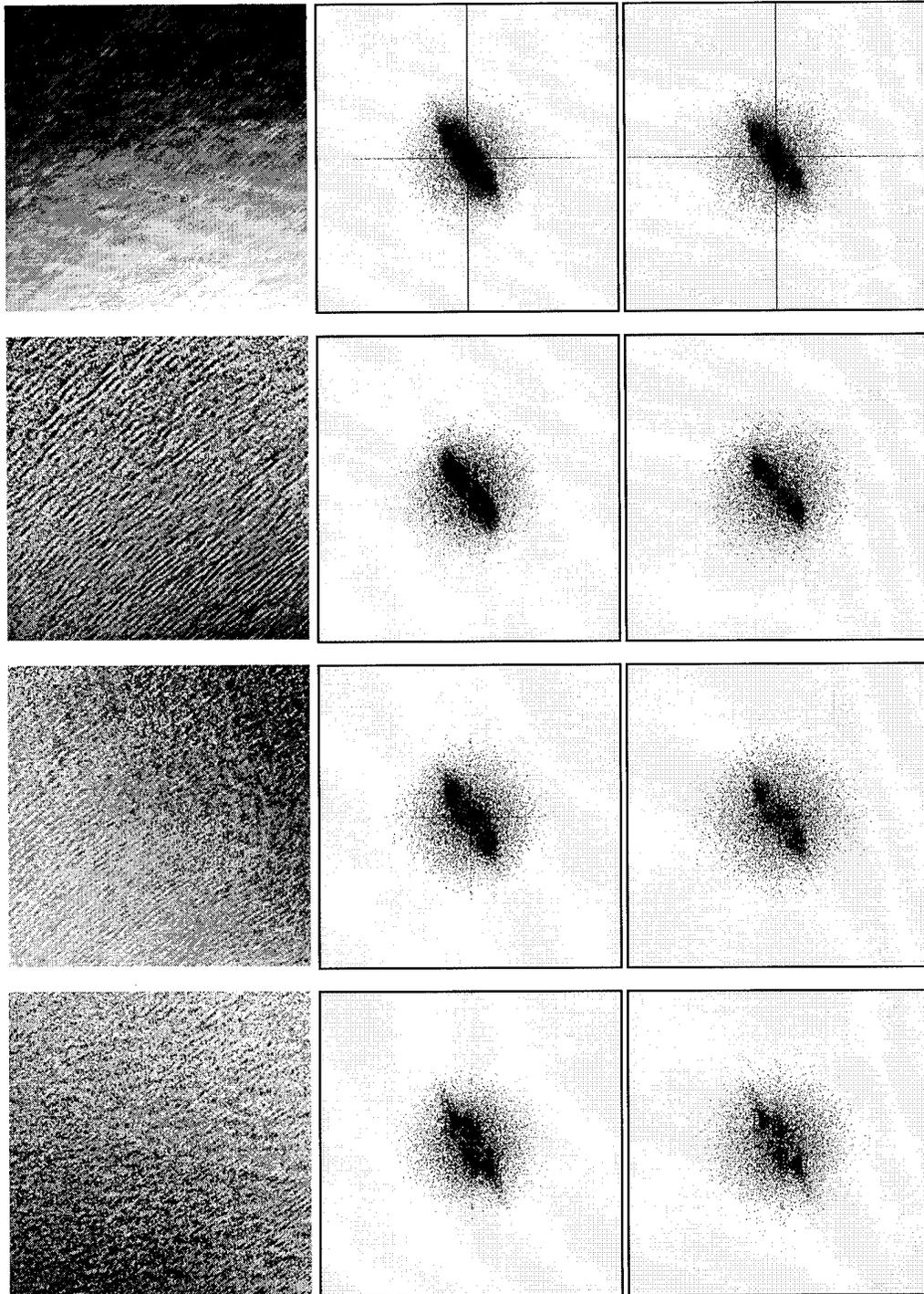
Figures 4.5-13 through 16 (a), (b), and (c). I, P, T, and D component subimages (a) containing the four subimage patches, the average PSDs of the patches (b), and their ADPs (c). Again, the ADPs are normalized to the integrated variance of the average PSD and represent the fractional difference variance relative to the average PSD at each spatial frequency. The ADP representations here were rescaled in order to preserve contrast in the figures. Also, both spectral scales were inverted this time so that the larger magnitudes are represented by darker pixels and smaller magnitudes by lighter pixels.

140

**Integrated Difference Variance
(Aerial Waterwave Image)**
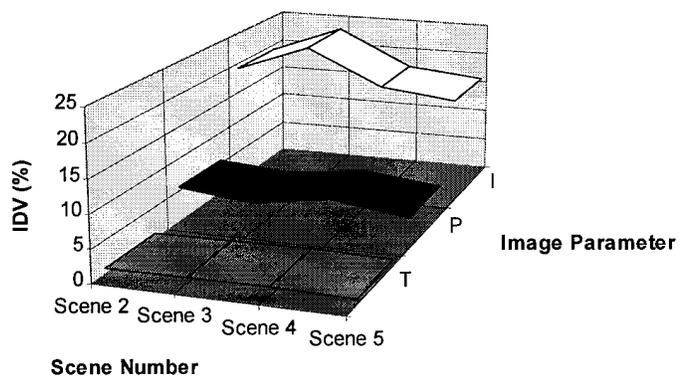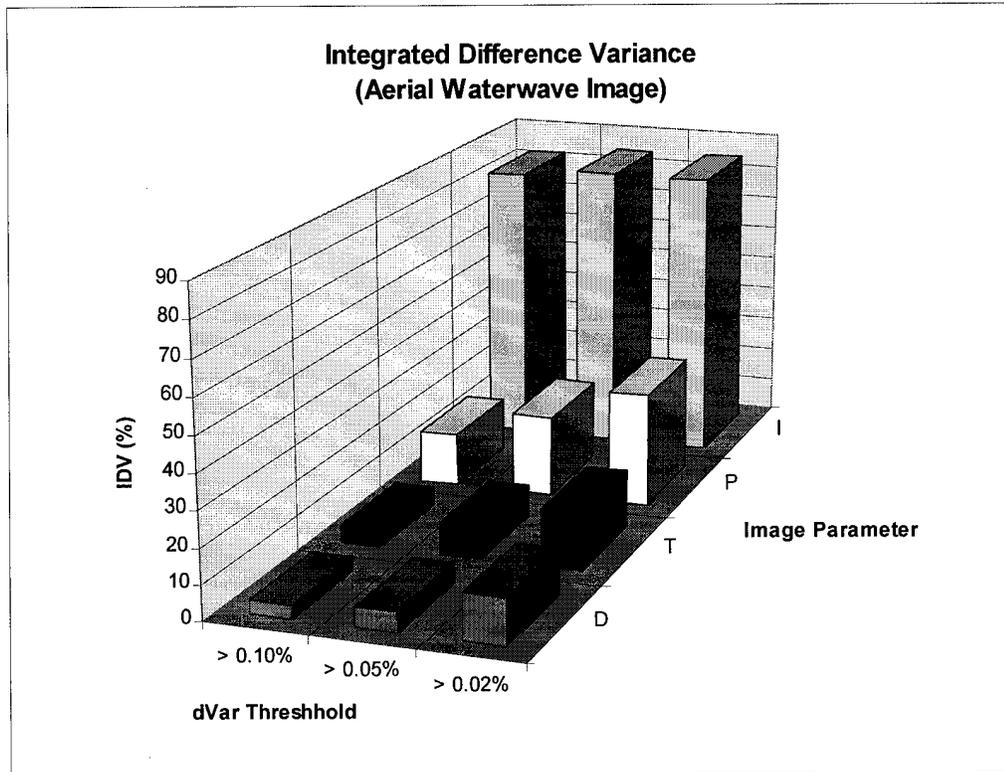
Figure 4.5-17.

With reference to Figure 4.5-17, the IDVs for the three polarimetric components I, P, and T consistently demonstrate the same clear distinction of the relative stabilities of their PSDs that was observed for the in-field experiment: here the IDVs for P are between one third and one half the IDVs of I, and the IDVs for T are between one third and one half the IDVs of P.

As noted in Chapter 4.4, the I image (refer again to Figure 4.5-13(a)) contained significant direct solar reflection in the lower portions of Patches B and D that rapidly diminishes in intensity for pixel values moving toward the top of Patches A and C; and the high contrast would provide a more dramatic comparison of I with the relative stability of the P and T spatial spectra. The high IDV value for I, in this case, is due to the four patches each containing, within their PSDs, a single large

141

fundamental spatial frequency component that represents the 1-cycle spatial modulation from high intensity at the bottom of each patch to low intensity at the top. The differential variance for the four PSDs for this one spectral component represents 23.13% of the IDV in the calculation for dVar > 0.02%. Subtraction of this single component reduces the fractional IDV for I by almost one third to 61.22%, providing the same proportional scale of I, P , and T stability for the aerial image as is observed for the in-field images.

The ADP was also calculated for the difference (D) subimage patches to give an indication of the spatial spectral stability of the systematic error in the uncalibrated image. While D is highly correlated with the other three spectra, it also has the highest relative stability of the four ADPs, both factors suggesting that the increased aerial IDV values for I, P, and T relative to the corresponding in-field IDV values are due to the calibration errors associated with D. The relative stability of D also suggests that the increase in the aerial IDV values created by the non-zero presence of D is in relatively constant proportion to the calibrated in-field IDV values. This appears to be the case: the uncalibrated aerial IDV values are larger than their corresponding calibrated in-field IDV values by a constant factor of about two. The inverse of this statement is that, based on the limited results here, sensitometric calibration of this image data appears to roughly double the stability of the spectral estimates compared with uncalibrated image data. Enhanced quantitative analysis and validation of these limited observations is recommended in Chapter 5.

Table 4-10
IDV Summary Report

In-field results by scene (for dVar > 0.10%)

Parameter	Scene 2	Scene 3	Scene 4	Scene 5
I	11.81	14.32	11.50	7.76
P	1.35	1.58	1.65	1.80
T	0.00	0.00	0.56	0.25
(for dVar > 0.05%)				
I	18.94	23.42	17.68	16.46
P	5.50	4.47	6.18	4.71
T	0.73	1.01	1.17	0.92
(for dVar > 0.02%)				
I	28.85	32.56	26.51	24.17
P	16.10	12.96	14.45	12.77
T	5.27	6.33	5.33	5.01

In-field results by solar elevation (for dVar > 0.10%)

Parameter	Sol Elev 1	Sol Elev 2	Sol Elev 3	Sol Elev 4
I	10.70	12.78	14.04	25.36
P	0.69	3.25	2.51	1.83
T	0.30	0.00	0.00	0.44
(for dVar > 0.05%)				
I	20.05	22.97	25.86	39.65
P	6.76	8.03	8.95	6.06
T	1.00	1.28	0.92	1.24
(for dVar > 0.02%)				
I	30.24	33.06	35.93	54.21
P	18.24	16.53	19.70	17.03
T	4.72	7.59	6.59	5.90

Aerial results by dVar

Parameter	> 0.10%	> 0.05%	> 0.02%
I	82.18	84.35	84.35
P	15.20	23.55	33.01
T	5.11	9.08	16.29
D	3.76	5.75	13.14

143

5.0 Conclusions and recommendations

Conclusions

The results of this study have produced five main conclusions:

1) Sensitometric co-calibration of the characteristic curves for the input images (i.e., the photo quads) is important for the accurate calculation of the Stokes parameters and derivatives. In particular, the non-linear transformation of intensity is shown to distort the calculation of T and its variance for the extreme case of saturation. Saturation at the extrema should be avoided; linear transformation over a wide range of intensity should be sought.

2) The polarimetric difference image (D) provides a direct measurement of sensitometric co-calibration error and a potential tool for mitigating systematic error.

3) For the reflecting surfaces that were imaged under clear sky conditions, the histogram distributions of T provide an indirect measure of the azimuthal difference between the polarizer reference plane and the principal plane containing the sun. This indirect measurement provides the potential capability to calculate the the azimuth of either plane when only one is known, or to calibrate the system when the azimuths of both are known. The measurements acquired within the current study indicate that the calibrated polarimeter values of T were in good agreement with independent calculations.

4) The calibrated polarimetric components P and T provide a more stable estimate of spatial PSD distribution in relation to I. Within the limited exploration of parameters, P demonstrates PSDs that have twice the stability of I; and T demonstrates PSDs that have two to three times the stability of P.

5) Within the limited exploration of parameters, the stability of the PSDs of the calibrated polarimetric components P and T demonstrate a relative insensitivity to imaging geometry compared with I.

In sum, the results of this study indicate that the calibrated polarimetric image set (I, P, T) has the potential to provide a significant advantage over the unpolarized image component (I) alone in the detection, discrimination, and classification of spatial content through the relative stability and geometric invariance in the estimation of spatial power spectral density.

Recommendations

The list of recommendations follows the sequential analysis of the full polarimetric imaging chain, beginning with the illumination source and ending with interpretation of the final image products.

Illumination source / radiation path analysis

1) Further imaging studies should provide detailed insight into the full range of natural polarized radiance conditions that can illuminate both natural and artificial terrestrial scene contents. In particular, optimizing

illumination conditions for polarimetric remote sensing should be explored. A full parametric surface exploration of imaging geometry combinations under various natural polarized radiance conditions is recommended.

Polarized target characterization

2) Enhanced imaging studies should emphasize the characterization of polarized bidirectional reflectance distributions (BRDF) for terrestrial features under natural polarized radiance conditions. In particular, the polarized spatial content analysis of large spatially correlated and uncorrelated natural features should be investigated for optimizing imaging geometries.

3) The eight targets of opportunity that were imaged during the aerial collection exist as a point of departure for an initial color remote sensing assessment.

Polarimetric imaging sensor enhancements

4) Other linear polarizers, for example Polaroid HN38S, should be evaluated for potentially improved remote sensing performance in the visible spectrum; an investigation of infrared and multispectral polarimetric imaging strategies should also be considered, for instance, in a ganged, multi-camera, multi-lens camera system that could emulate the POLDER instrument but with simultaneous, rather than sequential, image collection.

5) If a different camera can be employed, high quality lenses should be incorporated in a multi-lens, mapping camera type system. The system should, as a minimum, include positive shutter control and motorized film advance (features that are lacking in the current system).

6) Combinations of f-stop, exposure time, film speed, and polarizing filter density should be evaluated for their ability to provide the largest linear range of exposure (i.e., exposure latitude) for polarimetric remote sensing in support of the calibrated transformation of exposure to intensity.

7) If possible, detector arrays should be considered as a replacement for film at the four focal planes. The most significant benefit of current solid state charge-coupled device (CCD) arrays is their excellent linearity in output over a very large range of input intensity. This benefit obviates the requirement for sensitometric procedures except for initial system calibration and absolute calibration maintainance. The many other benefits include direct digitization, contrast control, direct radiometric co-calibration control, and direct co-registration control. The ultimate advantage of this replacement is the potential for near-real-time creation of the polarimetric image set since the arrays could port their image data directly into a digital computer and Stokes parameter processing could automatically initiate upon receipt of quad image data.

Polarimetric image processing enhancements

8) Additional film digitization techniques should be evaluated for their ability to provide faithful reproduction of digital number values that linearly and directly correlate with relative intensity values. For instance, a dedicated film scanner would provide the researcher with full control over the digitization process, in particular, control of contrast and color balance. Several 35-mm slide scanners exist in the market that have excellent illumination and thermal stability because they use light emitting diode (LED) technology; one unit also has high spatial resolution (9.4-micron spot size) and fits within a standard 5.25-inch computer drive bay. The

flexibility of these scanning systems also allows consideration of color reversal film (e.g., slide transparencies)

9) One significant improvement for future Stokes vector processing would be the incorporation of a fully automated or semi-automated co-registration capability using cross-correlation. This enhancement would remove the operator as a source of registration error through elimination of the operator's tedious and subjective selection of registration points that are common within the four image quads. For example, co-registration within the current study involved the selection of eight common points for each of the four quads, or 32 total points for each Stokes image set.

Figure 5.0-1 illustrates an example of cross-correlation. Image (b) is translated relative to image (a), the product of their pixel values are summed for each translation, and the sum reported as the pixel value of image (c).
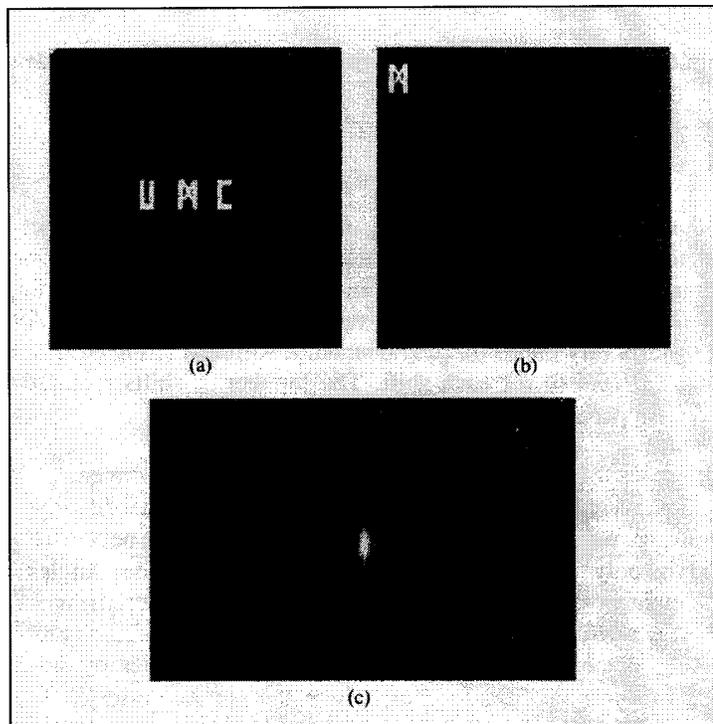
Figure 5.0-1 (a), (b), and (c). Example of cross-correlation [from Gonzalez & Wintz, 1987].

The enhancement would involve the cross-correlation of small (e.g., 20 x 20 pixel) unregistered subimages, both containing the same approximate in-scene features, to detect the common centroid coordinates as the

highest peak in the cross-correlation through the calculation of the normalized cross-correlation coefficient:

$$C(X,Y) = \frac{\iint f(x,y)g(x+X,y+Y)dX\,dY}{\sqrt{\iint [f(x,y)]^2\,dx\,dy \iint [g(x,y)]^2\,dx\,dy}}$$

Equation 5-1

where f(x,y) and g(x,y) are the two subimages. C(X,Y) attains a maximum value when the two subimages match each other, as illustrated in Figure 5.0-1 (c).

The main simplifying assumption is that the co-registration of the image quads is predominantly a translation of coordinates rather than a rotation or scale change, since the four optic axes and four focal plane axes are all fixed approximately in parallel with each other; therefore, the cross-correlation effectively evaluates all translation combinations of subimage coordinates until the spatial distributions of the two subimages achieve a match. Multiple centroid coordinates can be automatically generated until the number is sufficient for the polynominal fit of the desired registration.

An evaluation of this co-registration approach is recommended.

10) A second significant improvement for future Stokes vector processing would be the incorporation of a fully automated or semi-automated sensitometric cross-calibration capability. This capability would take advantage of the ready availability of the difference (D) image as a derivative analytic product for co-calibration refinement. The key simplifying assumption is that the recorded exposures of the four image quads correlate with intensity through a single characteristic curve (an assumption that should have held but did not hold for the current study).

The residual error in the D image should then, for the most part, represent the effect of non-linearity in the characteristic curve at the extrema and, to a lesser degree, represent the effect of other system errors such as pixel mis-registrations from parallax, lens and filter vignetting, and *etc.*

This enhancement would essentially involve a pixel-by-pixel analysis of the four quad images and the difference (D) image with the intent of minimizing D by equalizing the sum of the two polarized pairs, i.e., making I' equal to I". The simplest case for the analysis logic would first evaluate the two polarized pairs to determine which of the quads have dn values that are nearest the extrema of the characteristic curve and suffer most from nonlinearity in transformation. If three of the four dn values fall within the linear region, the value of D would be applied to the fourth value so that I' = I" and D = 0. A more sophisticated approach would be to estimate the amount of nonlinearity that each pixel value in each quad may suffer, calculate the histogram distribution of these estimates, and then use an iterative least squares optimization approach to distribute a weighted fraction of D to each of the quads until the difference and the histogram both approach acceptable minima.

An evaluation of this calibration approach is recommended.

Polarimetric image analysis enhancements

11) Enhanced imaging studies should consider more robust PSD stability measurements, using a full parametric surface exploration of imaging geometries for terrestrial features under natural polarized radiance conditions. In particular, PSD stability analysis of large spatially correlated and uncorrelated natural features should be investigated for

optimizing imaging geometries. This effort should hopefully provide an independent validation of the limited IDV results in this study.

Enhanced PSD and PSD stability measurements would include the capability to execute the double integration of the two-dimensional ADP surface, instead of the approximate histogram method employed in this study. The most significant benefit of this capability is the option to selectively calculate IDV as a function of one variable, spatial frequency or azimuth (through a partial integration over the other variable), and then evaluate the stability of the PSD with respect to these spatial parameters:

$$S(k) = \sum_{\theta=0}^{\pi} S_\theta(k)$$

Equation 5-2

$$S(\theta) = \sum_{k=0}^{k_{max}} S_k(\theta)$$

Equation 5-3

Figure 5.0-2 illustrates examples of the one-dimensional spatial spectra in comparison with the original image and its two-dimensional spectrum.

An evaluation of this spatial analysis enhancement is recommended.

12) Finally, a calibrated polarimetric imaging model should be validated with respect to the performance of a calibrated imaging polarimeter. The results of Chapter 4.3 provide some qualitative insight into the spatial performance of a limited model imaging a specific feature within a limited range of imaging geometries under clear sky conditions; but a robust model needs to provide the quantitative correlation that can predict system performance for the more general case of polarimetric remote sensing of various terrestrial features collected over a broad range
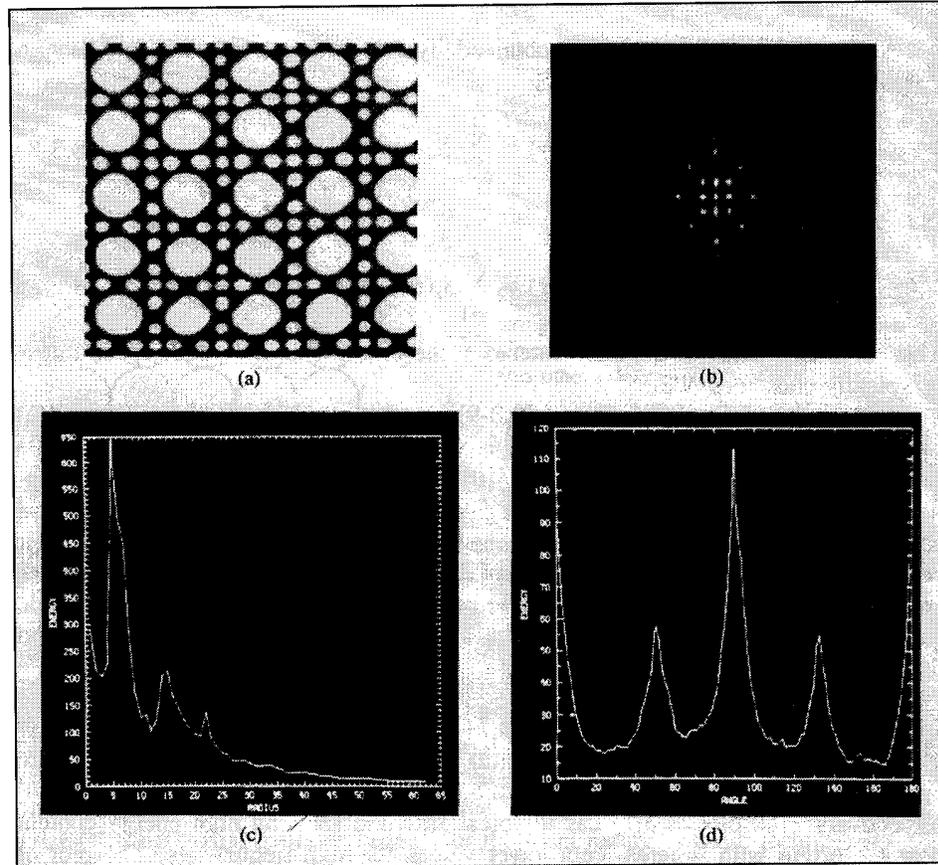
Figure 5.0-2 (a), (b), (c), and (d). Image (a), its two-dimensional spatial spectrum S(spatial frequency, azimuth) (b), its one-dimensional spectrum S(spatial frequency) (c), and its one-dimensional spectrum S(azimuth) (d) [from Gonzalez & Wintz, 1987].

of imaging geometries and illumination conditions, many of which may not be ideal.

6.0 References

Abshire, J.B. & J.F. McGarry, "Two-color short-pulse laser altimeter measurements of ocean surface backscatter", in Applied Optics, 26(7), pp 1304-1310, 1987.

Andrews, C.L., Optics Of The Electromagnetic Spectrum, Prentice-Hall, Englewood Cliffs NJ, 1960.

Azzam, R.M.A. & N.M. Bashara, Ellipsometry And Polarized Light, North-Holland, Amsterdam, 1977.

Barber, N.F., "A diffraction analysis of a photograph of the sea", in Nature, 164(4168), pp 485, 1949.

Barber, N.F., "Finding the direction of travel of sea waves", in Nature, 174(4440), pp 1048-1050, 1954.

Breon, F.M. & P.Y. Deschamps, "Optical and physical parameter retrieval from POLDER measurements over the ocean using an analytical model", in Remote Sensing of the Environment, 43(1), pp 97-114, 1993.

Carlson, G.E., "Estimation of ocean wave wavenumber and propagation direction from limited synthetic aperture radar data", in IEEE Transactions on Geoscience and Remote Sensing, GE-22(6), pp 609-614, 1984.

Cartwright, D.E. & M.S. Longuet-Higgins, "The statistical distribution of the maxima of a random function", in Proceedings of the Royal Society, A237(1209), pp 212-232, 1956.

Chapman, R.D. & G.B. Irani, "Errors in estimating slope spectra from wave images", in Applied Optics, 20(20), pp 3645-3652, 1981.

CIE Technical Committee 4.2, "Standardization of luminance distribution on clear skies", in CIE Publication #22, Comission International de l'Eclairaze, Paris, 1973.

Clarke, D. & J.F. Grainger, <u>Polarized Light and Optical Measurement</u>, Pergamon Press, Oxford, 1971.

Cote, L.J., J.O Davies, W. Marks, R.J. McCough, E. Mehr, W.J. Pierson, J.F. Ropek, G. Stephenson & R.C. Vetter, "The directional spectrum of a wind-generated sea as determined from data obtained by the stereo wave observation project", in Meteorological Papers, NYU College of Engineering, 2(6), 1960.

Coulson, K.L., <u>Solar and Terrestrial Radiation</u>, Academic Press, New York, 1975.

Coulson, K.L., V.S. Whitehead & C. Campbell, "Polarized views of the earth from orbital altitude", in Proceedings of the Society of Photo-Optical Instrumentation Engineers, 637, pp 35-41, 1986.

Cox, C.S. & W.H. Munk, "Measurement of the roughness of the sea surface from photographs of the sun's glitter", in Journal of the Optical Society of America, 44(11), pp 838-850, 1954a.

Cox, C.S. & W.H. Munk, "Statistics of the sea surface derived from sun glitter", in Journal of Marine Research, 13(2), pp 198-227, 1954b.

Curran, P.J., "A photographic method for the recording of polarized visible light for soil surface moisture indications", in Remote Sensing of the Environment, 7, pp 305-322, 1978.

Curran, P.J., "The use of polarized panchromatic and false-color infrared film in the monitoring of soil surface moisture", in Remote Sensing of the Environment, 8, pp 249-266, 1979.

Curran, P.J., "Remote sensing: the use of polarised visible light to estimate surface soil moisture", in Applied Geography, 1 pp 41-53, 1981a.

Curran, P.J., "The relationship between polarized visible light and vegetation amount", in Remote Sensing of the Environment, 11, pp 87-92, 1981b.

Curran, P.J., "Polarized visible light as an aid to vegetation classification", in Remote Sensing of the Environment, 12, pp 491-499, 1982.

Deschamps, P.Y., F.M. Breon, M. Leroy, A. Podaire, A. Bricaud, J.C. Buriez & G. Seze, "The POLDER mission: instrument characteristics and scientific objectives", in IEEE Transactions on Geoscience and Remote Sensing, 32(3), pp 598-615, 1994.

Deuze, J.L., F.M. Breon, J.L. Roujean, P.Y. Deschamps, C. Devaux, M. Herman & A. Podaire, "Analysis of the POLDER airborne instrument observations of land surfaces", in Remote Sensing of the Environment, 45, pp 137-154, 1993.

Duggin, M.J., S.A. Israel, V.S. Whitehead, J.S. Myers & D.R. Robertson, "Use of polarization methods in earth resources investigations", in Proceedings of the Society of Photo-Optical Instrumentation Engineers, 1166, pp 11-22, 1989.

Egan, W.G., Photometry and Polarization in Remote Sensing, Elsevier Science Publishing, New York, 1985.

Egan, W.G., "Proposed design of an imaging spectropolarimeter / photometer for remote sensing of earth resources", in Optical Engineering, 25, pp 1155-1159, 1986.

Egan, W.G., S.A. Israel & W.R. Johnson, "Terrestrial polarization imagery obtained from the space shuttle: characterization and interpretation", in Applied Optics, 30, pp 435-442, 1991.

Egan, W.G., S.A. Israel & W.R. Johnson, "High-resolution space-shuttle polarimetry for farm crop classification", in Applied Optics, 31, pp 1542-1548, 1992.

Fisher, M.G., Oceanographic Analysis of Sun Glint Images Taken on Space Shuttle Mission STS 41-G, M.S. Thesis, Naval Postgraduate School, 1986.

Gonzalez, R.C. & P. Wintz, <u>Digital Image Processing</u>, Addison-Wesley, Reading MA, 1987.

Gotwols, B.L. & G.B. Irani, "Optical determination of the phase velocity of short gravity waves", in Journal of Geophysical Research, 85(C7), pp 3964-3970, 1980.

Hasselmann, D.E., M. Dunckel & J.A. Ewing, "Directional wave spectra observed during JONSWAP 1973", in Journal of Physical Oceanography, 10, pp 1264-1280, 1980.

Hecht, E. & A. Zajac, <u>Optics</u>, Addison-Wesley, Reading MA, 1987.

Holthuijsen, L.H., "Observations of the directional distribution of ocean-wave energy in fetch limited conditions", in Journal of Physical Oceanography, 13(2), pp 191-207, 1983a.

Holthuijsen, L.H., "Stereophotography of ocean waves", in Applied Ocean Research, 5(4), pp 204-209, 1983b.

Hulburt, E.O., "The polarization of light at sea", in Journal of the Optical Society of America, 24, pp 35-42, 1934.

Israel, S.A., <u>Analysis of Space Shuttle and Video Polarization Imagery</u>, M.S. Thesis, SUNY College of Environmental Science and Forestry, Syracuse NY, 1991.

Jenkins, F.A. & H.E. White, <u>Fundamentals of Optics</u>, McGraw-Hill, New York, 1976.

Kasevich, R.S., C.H. Tang & S.W. Henriksen, "Energy spectra of sea waves for photographic interpretation", in Proceedings of the Seventh International Symposium on Remote Sensing of the Environment, pp 607-624, University of Michigan, Ann Arbor, 1971.

Kasevich, R.S., C.H. Tang & S.W. Henriksen, "Analysis and optical processing of sea photographs for energy spectra", in IEEE

Transactions on Geoscience and Electronics, GE-10(1), pp 51-58, 1972.

Kasevich, R.S., "Directional wave spectra from daylight scattering", in Journal of Geophysical Research, 80(33), pp 4535-4541, 1975.

Kay, S.M., <u>Modern Spectral Estimation: Theory and Application</u>, Prentice-Hall, Englewood Cliffs NJ, 1988.

Keller, W.C. & B.L. Gotwols, "Two-dimensional optical measurement of wave slope", in Applied Optics, 22(22), pp 3476-3478, 1983.

Kinsman, B., <u>Wind Waves: their generation and propagation on the ocean surface</u>, Prentice Hall, Englewood Cliffs NJ, 1965.

Konnen, G.P., <u>Polarized Light in Nature</u>, Cambridge University Press, Cambridge England, 1985.

Longuet-Higgins, M.S., "On the statistical distribution of the heights of sea waves", in Journal of Marine Research, 11(3), pp 245-266, 1952.

Longuet-Higgins, M.S., "Statistical properties of a moving wave-form", in Proceedings of the Cambridge Philosophical Society, 52(2), pp 234-245, 1956.

Longuet-Higgins, M.S., "The statistical analysis of a random moving surface", in Philosophical Transactions of the Royal Society, A249(966), pp 321-387, 1957.

Longuet-Higgins, M.S., "On the interval between successive zeros of a random function", in Proceedings of the Royal Society, A246, pp 99-118, 1958.

Longuet-Higgins, M.S., "Reflection and refraction at a random moving specular point", Parts I, II & III in Journal of the Optical Society of America, 50(9), pp 838-856, 1960.

Longuet-Higgins, M.S., "The directional spectrum of ocean waves, and processes of wave generation", in Proceedings of the Royal Society, A265(1322), pp 286-315, 1962.

Lybanon, M., "Ocean wave slope statistics from automated analysis of sun glitter photographs", NORDA Report 103, 1985.

Marks, W. & F.C. Ronne, "Aerial stereo-photography and ocean waves", in Photogrammetric Engineering & Remote Sensing, 21, pp 107-110, 1955.

Maul, G.A., Introduction to Satellite Oceanography, Martinus Nijhoff Publishers, Dordrecht Netherlands, 1985.

McLeish, W., "Spatial spectra of ocean surface temperature", in Journal of Geophysical Research, 75(33), pp 6872-6877, 1970.

Moffitt, F.H. and E.M. Mikhail, Photogrammetry, Harper & Row, New York, 1980.

Monaldo, F.M. & R.S. Kasevich, "Optical determination of short-wave modulation by long ocean gravity waves", in IEEE Transactions on Geoscience and Remote Sensing, GE-20(3), pp 254-259, 1982.

Monaldo, F.M. & D.R. Lyzenga, "On the estimation of wave slope-and height-variance spectra from SAR imagery", in IEEE Transactions on Geoscience and Remote Sensing, GE-24(4), pp 543-551, 1986.

North, J.A., Fourier Image Synthesis and Slope Spectrum Analysis of Deepwater, Wind-wave Scenes Viewed at Brewster's Angle, M.S. Thesis, Rochester Institute of Technology NY, 1989.

Palm, C.S., R.C. Anderson & A.M. Reece, "Laser probe for measuring 2-D wave slope slpectra of ocean wave capillary waves", in Applied Optics, 16(4), pp 1074-1081, 1977.

Partington, J.R., <u>An Advanced Treatise on Physical Chemistry</u>, Vol IV, Physico-Chemical Optics, Longman, Green & Co., Ltd., London, 1953.

Pierson, W.J., Jr. & W. Marks, "The power spectrum analysis of ocean wave records", in Transactions of the American Geophysical Union, 33(6), pp 834-844, 1952.

Pierson, W.J., Jr. & R.A. Stacy, "The elevation, slope, and curvature spectra of a wind roughened sea surface", NASA Contractor Report 2247, 1973.

Pos, J.D., L.P. Adams & F.A. Kilner, "Synoptic wave height and pattern measurements in laboratory wave basins using close-range photogrammetry", in Photogrammetric Engineering and Remote Sensing, 54(12), pp 1749-1756, 1988.

Prosch, T., D. Hennings & E. Raschke, "Video polarimetry: a new technique in atmospheric science", in Applied Optics, 22(9), pp 1360-1363, 1983.

Research Systems, Inc., <u>ENVI^{TM} User' Guide: The Environment for Visualizing Images, Version 1.1</u>, BSC Limited Liability Company, Boulder CO,1994.

Robinson, I.S., <u>Satellite Oceanography, an introduction for oceanographers and remote-sensing scientists</u>, Ellis Horwood Limited, West Sussex England, 1985.

Saunders, P.M., "Shadowing on the ocean and the existence of the horizon", in Journal of Geophysical Research, 72(18), pp 4643-4649, 1967.

Saunders, P.M., "Radiance of sea and sky in the infrared window 800-1200 cm^{-1}", in Journal of the Optical Society of America, 58(5), pp 645-652, 1968.

Sawyer, D.W., "Preliminary report on the determination of water surface profiles", U.S. Naval Photographic Interpretation Center Report 103-49, 1949.

Schau, H.C., "Measurement of capillary wave slopes on the ocean" in Applied Optics, 17(1), pp 15-17, 1978.

Schooley, A.H., "A simple method for measuring the statistical distribution of water wave surfaces", in Journal of the Optical Society of America, 44(1), pp 37-40, 1954.

Sheres, D., Remote Synoptic Surface Flow Measurements in Small Bodies of Water, Ph.D. Dissertation, University of California, San Diego CA, 1980.

Sheres, D., "Remote and synoptic water-wave measurements by aerial photography: a model, experimental results, and an application", in IEEE Journal of Oceanic Engineering, OE-6(2), pp 63-69, 1981.

Shurcliff, W.A., Polarized Light, Harvard University Press, Cambridge MA, 1962.

Sidran, M., "Broadband reflectance and emissivity of specular and rough water surfaces", in Applied Optics, 20(18), pp 3176-3183, 1981.

Stewart, R.H., Methods of Satellite Oceanography, University of California Press, Berkeley & Los Angeles CA, 1985.

Stilwell, D., Jr., "Directional energy spectra of the sea from photographs", in Journal of Geophysical Research, 74(8), pp 1974-1986, 1969.

Stilwell, D., Jr. & R.O. Pilon, "Directional spectra of surface waves from photographs", in Journal of Geophysical Research, 79(9), pp 1277-1284, 1974.

Talmadge, D.A. & P.J. Curran, "Remote sensing using polarized light", in International Journal of Remote Sensing, 7, pp 47-64, 1986.

Travis, L.D., "Remote sensing of aerosols with the earth observing scanning polarimeter", in Conference Proceedings of the Society of Photo-Optical Instrumentation Engineers, San Diego CA, July 1992.

Walraven, R., "Polarization Imagery", in Proceedings of the Society of Photo-Optical Instrumentation Engineers, 112, pp 164-167, 1977.

Walraven, R., "Polarization Imagery", in Optical Engineering, 20(1), pp 14-18, 1981.

Weinman, J.A., "Derivation of atmospheric extinction profiles and wind speed over the ocean from a satellite-borne lidar", in Applied Optics, 27(19), pp 3994-4001, 1988.

Whitehead, V.S., & W.G. Egan, "Analysis of terrestrial polarization imagery obtained from the space shuttle", in Transactions of the American Geophysical Union, 70, p 301, 1989.

```
            PROGRAM SKYIMAGE
*
* Creates synthetic polarized reflected skydome intensity images as functions
* of variables Beta & Alpha (dome mirror slope angles) & fixed constants Theta
* (sensor declination), Phi (sensor azimuth: fixed at 180 deg), Thet0 (sun
* declination) & Phi0 (sun azimuth). Other program constants:
*
*     FD (focal distance from mirror)
*     MRD (radius of dome mirror)
*     DSD (pixel detector sampling distance)
*     Nreal & Nimag (complex surface reflection coefficients of mirror)
*     K_1 & K_2 (transmission coefficients for non-ideal linear polarizer)
*     Depol (depolarization coefficient for non-ideal linear polarizer)
*     Gamma & Bias (effective sensor exposure gamma & offset)
*     DN_max (maximum digital number for pixel intensity)
*
* [Intensity arrays span Beta angle values <= 45 degrees, to correspond with
* the upper bound for surface slope that reflects modeled skydome radiance]
*
* Creates derivative Stokes parameter images from the synthetic polarized
* reflected skydome intensity images.
*
            IMPLICIT NONE
            INTEGER I,J,N,P,Q
            PARAMETER (N=64,P=-N/2,Q=N/2-1)
            REAL ISRF [FAR](P:Q,P:Q),QSRF [FAR](P:Q,P:Q),USRF [FAR](P:Q,P:Q)
            REAL PSRF [FAR](P:Q,P:Q),TSRF [FAR](P:Q,P:Q)
            REAL I000 [FAR](P:Q,P:Q),I045 [FAR](P:Q,P:Q),I090 [FAR](P:Q,P:Q)
            REAL I135 [FAR](P:Q,P:Q)
            REAL DSD,FD,FL,MRD,PHI0,PI,THETA,THET0,NREAL,NIMAG,N_MAG
            REAL PARM(1:4,1:4),K_1,K_2,POL_MAX,DEPOL,GAMMA,BIAS,DN_MAX
            CHARACTER*24 FNAME,FNAME1,FNAME2,FNAME3,FNAME4,FNAME5
            CHARACTER*24 FNAME6,FNAME7,FNAME8,FNAME9
*
* Define constants
*
            PI = 3.141593
*
* Input parameters from external file
*
            WRITE(*,*) ' Enter filename of input parameters '
            READ(*,300) FNAME
            WRITE (*,*) ' Reading parameter file .....'
            OPEN(1,FILE=FNAME,ERR=5)
            DO I=1,4
                        READ(1,*) (PARM(I,J),J=1,4)
            ENDDO
            CLOSE(1)
*
            WRITE(*,*) ' '
            DO I=1,4
                        WRITE(*,*) (PARM(I,J),J=1,4)
            ENDDO
            PAUSE
*
* Assign variable names to input parmaters
*
            FD = PARM(1,1)
            FL = PARM(1,2)
            MRD = PARM(1,3)
            DSD = PARM(1,4)
            POL_MAX = PARM(2,1)
            DEPOL = PARM(2,2)
```

```fortran
      GAMMA = PARM(2,3)
      BIAS = PARM(2,4)
      THETA = PARM(3,1)
      PHI0 = PARM(3,2)
      THET0 = PARM(3,3)
      DN_MAX = PARM(3,4)
      NREAL = PARM(4,1)
      NIMAG = PARM(4,2)
      K_1 = PARM(4,3)
      K_2 = PARM(4,4)
*

      THETA = THETA*(PI/180.0)
      PHI0 = PHI0*(PI/180.0)
      THET0 = THET0*(PI/180.0)
      N_MAG = SQRT(NREAL**2.0 + NIMAG**2.0)
*
* Call subroutine SKYSURF
*
      CALL SKYSURF (PHI0,THET0,THETA,N_MAG,FD,FL,MRD,DSD,POL_MAX,DEPOL,
     +      GAMMA,BIAS,DN_MAX,K_1,K_2,P,Q,ISRF,QSRF,USRF,
     +      PSRF,TSRF,I000,I045,I090,I135)
*
      WRITE(*,*) ' '
      WRITE(*,*) ' SKYSURF completed successfully'
*
      WRITE(*,*) ' '
      WRITE(*,*) ' Enter filename w/ drive letter & directory for ',
     +      ' ISRF data'
*     READ(*,300) FNAME1
      FNAME1 = 'ISRF.DAT'
      WRITE(*,*) ' '
      WRITE(*,*) ' Enter filename w/ drive letter & directory for ',
     +      ' QSRF data'
*     READ(*,300) FNAME2
      FNAME2 = 'QSRF.DAT'
      WRITE(*,*) ' '
      WRITE(*,*) ' Enter filename w/ drive letter & directory for ',
     +      ' USRF data'
*     READ(*,300) FNAME3
      FNAME3 = 'USRF.DAT'
      WRITE(*,*) ' '
      WRITE(*,*) ' Enter filename w/ drive letter & directory for ',
     +      ' PSRF data'
*     READ(*,300) FNAME4
      FNAME4 = 'PSRF.DAT'
      WRITE(*,*) ' '
      WRITE(*,*) ' Enter filename w/ drive letter & directory for ',
     +      ' TSRF data'
*     READ(*,300) FNAME5
      FNAME5 = 'TSRF.DAT'
      WRITE(*,*) ' '
      WRITE(*,*) ' Enter filename w/ drive letter & directory for ',
     +      ' I000 data'
*     READ(*,300) FNAME6
      FNAME6 = 'I000.DAT'
      WRITE(*,*) ' '
      WRITE(*,*) ' Enter filename w/ drive letter & directory for ',
     +      ' I045 data'
*     READ(*,300) FNAME7
      FNAME7 = 'I045.DAT'
      WRITE(*,*) ' '
      WRITE(*,*) ' Enter filename w/ drive letter & directory for ',
     +      ' I090 data'
*     READ(*,300) FNAME8
      FNAME8 = 'I090.DAT'
      WRITE(*,*) ' '
      WRITE(*,*) ' Enter filename w/ drive letter & directory for ',
```

```
     +        ' I135 data'
*   READ(*,300) FNAME9
          FNAME9 = 'I135.DAT'
          WRITE(*,*) ' '
*
          OPEN(2,FILE=FNAME1,FORM='FORMATTED',ERR=5)
          DO I=P,Q
            WRITE(2,*) (ISRF(I,J),J=P,Q)
          ENDDO
          CLOSE(2)
          WRITE(*,*) ' ',FNAME1,' has been output'
*
          OPEN(2,FILE=FNAME2,FORM='FORMATTED',ERR=5)
          DO I=P,Q
            WRITE(2,*) (QSRF(I,J),J=P,Q)
          ENDDO
          CLOSE(2)
          WRITE(*,*) ' ',FNAME2,' has been output'
*
          OPEN(2,FILE=FNAME3,FORM='FORMATTED',ERR=5)
          DO I=P,Q
            WRITE(2,*) (USRF(I,J),J=P,Q)
          ENDDO
          CLOSE(2)
          WRITE(*,*) ' ',FNAME3,' has been output'
*
          OPEN(2,FILE=FNAME4,FORM='FORMATTED',ERR=5)
          DO I=P,Q
            WRITE(2,*) (PSRF(I,J),J=P,Q)
          ENDDO
          CLOSE(2)
          WRITE(*,*) ' ',FNAME4,' has been output'
*
          OPEN(2,FILE=FNAME5,FORM='FORMATTED',ERR=5)
          DO I=P,Q
            WRITE(2,*) (TSRF(I,J),J=P,Q)
          ENDDO
          CLOSE(2)
          WRITE(*,*) ' ',FNAME5,' has been output'
*
          OPEN(2,FILE=FNAME6,FORM='FORMATTED',ERR=5)
          DO I=P,Q
            WRITE(2,*) (I000(I,J),J=P,Q)
          ENDDO
          CLOSE(2)
          WRITE(*,*) ' ',FNAME6,' has been output'
*
          OPEN(2,FILE=FNAME7,FORM='FORMATTED',ERR=5)
          DO I=P,Q
            WRITE(2,*) (I045(I,J),J=P,Q)
          ENDDO
          CLOSE(2)
          WRITE(*,*) ' ',FNAME7,' has been output'
*
          OPEN(2,FILE=FNAME8,FORM='FORMATTED',ERR=5)
          DO I=P,Q
            WRITE(2,*) (I090(I,J),J=P,Q)
          ENDDO
          CLOSE(2)
          WRITE(*,*) ' ',FNAME8,' has been output'
*
          OPEN(2,FILE=FNAME9,FORM='FORMATTED',ERR=5)
          DO I=P,Q
            WRITE(2,*) (I135(I,J),J=P,Q)
          ENDDO
          CLOSE(2)
          WRITE(*,*) ' ',FNAME9,' has been output'
```

```
*
            GOTO 1
5           WRITE(*,*) 'Bad file opening'
300         FORMAT (A)
1           END
*
            SUBROUTINE SKYSURF (PHI0,THET0,THETA,N_MAG,FD,FL,MRD,DSD,POL_MAX,
    +           DEPOL,GAMMA,BIAS,DN_MAX,K_1,K_2,P,Q,
    +           ISRF,QSRF,USRF,PSRF,TSRF,I000,I045,I090,I135)
*
            IMPLICIT NONE
            INTEGER I,J,P,Q
            REAL ALPH,BETA,COSOMEGA,DEGC,THET,THETA,HALFPI,PI,QTRPI
            REAL ITMP,IX,IY,IZ,MAGI,NX,NY,NZ,OMEGA,QTMP,RX,RY,RZ,UTMP
            REAL ISRF [FAR](P:Q,P:Q),QSRF [FAR](P:Q,P:Q),USRF [FAR](P:Q,P:Q)
            REAL PSRF [FAR](P:Q,P:Q),TSRF [FAR](P:Q,P:Q)
            REAL I000 [FAR](P:Q,P:Q),I045 [FAR](P:Q,P:Q),I090 [FAR](P:Q,P:Q)
            REAL I135 [FAR](P:Q,P:Q)
            REAL A,B,BIAS,C,COSMU,COSMU2,COSNU,DEPOL,GAMMA,L,LREF,M,MU,NU,PHI
            REAL PHI0,POL_MAX,PSI,PX,PY,PZ,QX,QY,QZ,SX,SY,SZ,THET0
            REAL ATT,MDIAG,MDIAQ,MOFFD,N_MAG,RHO,RPAR,RPRP,TTMP
            REAL DN_MAX,DSD,FD,FL,IMAX1,IMAX2,K_1,K_2,IRAD,MHT,MRD,MRAD
*
* Define constants
*
            PI = 3.141593
            DEGC = PI/180.0
            HALFPI = PI/2.0
            QTRPI = PI/4.0
*
* Initiate variables
*
            IMAX1 = 0.0
            IMAX2 = 0.0
*
* Calculate LREF (zenith radiance value) relative to direct sun radiance
* (set at 100.0) based on CIE sky radiance model (after Hopkinson)
*
            COSMU = 1.0
            MU = 0.0
            A = 0.91+10.0*EXP(-3.0*MU)+0.45*(COSMU**2.0)
*
            IF (THET0.LT.HALFPI) THEN
              B = 1.0-EXP(-0.32/COS(THET0))
            ELSEIF (THET0.EQ.HALFPI) THEN
              B = 1.0
            ELSE
              WRITE(*,*) ' '
              WRITE(*,*) 'Solar declination indicates sun is below horizon'
            ENDIF
*
            C = 0.274*(0.91+10.0*EXP(-3.0*THET0)+0.45*(COS(THET0)**2.0))
*
            LREF = (100.0*C)/(A*B)
*
* Analyze reflected radiance unit vector R into xyz components
*
            RX = SIN(THETA)*COS(PI)
            RY = SIN(THETA)*SIN(PI)
            RZ = COS(THETA)
*
* Initiate double loop to generate 2-D image arrays
*
            DO I = P+1,Q
            DO J = P+1,Q
*
* Calculate pixel coordinates
```

```
* [Row I/L specifies Y-magnitude; Column J/M specifies X-magnitude]
*
            L = FLOAT(I)*DSD
            M = FLOAT(J)*DSD
*
* Calculate slope angle (BETA) and azimuth angle (ALPH) of mirror facet
* imaged by pixel (I,J)
*
* [Calculate radius of mirror image in image coordinates]
* [Calculate radius of mirror in cartesian (xy) coordinates: x/X = fl/FD]
* [Calculate height of mirror facet in cartesian (z) coordinates]
*
            IRAD = SQRT((L**2.0)+(M**2.0))
            MRAD = (FD*IRAD)/FL
            MHT = SQRT(MRD**2.0 - MRAD**2.0)
*
* [Calculate BETA]
*
            IF (MHT.GT.0.0) THEN
                        BETA = ATAN(MRAD/MHT)
            ELSE
                        BETA = 0.0
            ENDIF
*
* Set image arrays to zero if incident vector arrives from below the horizon
* [i.e., if 2*OMEGA > 90 deg; or if THET > 90 deg]
*
            IF (BETA.GT.QTRPI) THEN
                        ISRF(I,J) = 0.0
                        QSRF(I,J) = 0.0
                        USRF(I,J) = 0.0
                        PSRF(I,J) = 0.0
                        TSRF(I,J) = 0.0
                        I000(I,J) = 0.0
                        I045(I,J) = 0.0
                        I090(I,J) = 0.0
                        I135(I,J) = 0.0
                        GOTO 4
            ENDIF
*
* [Calculate ALPH]
*
            IF (BETA.GT.0.0) THEN
                        ALPH = ATAN2(L,M)
            ELSE
                        ALPH = 0.0
            ENDIF
*
* Analyze surface normal unit vector N into xyz components
*
            NX = SIN(BETA)*COS(ALPH)
            NY = SIN(BETA)*SIN(ALPH)
            NZ = COS(BETA)
*
* Dot product of R & N = |R||N|cos(omega) = (1.0) cos(omega)
*
            COSOMEGA = RX*NX + RY*NY + RZ*NZ
            OMEGA = ACOS(COSOMEGA)
*
* Specify xyz components of I, the incident skydome radiance vector
*
            IX = (NX*2.0*COSOMEGA) - RX
            IY = (NY*2.0*COSOMEGA) - RY
            IZ = (NZ*2.0*COSOMEGA) - RZ
*
* Normalize I -> |I| = 1.0
*
```

```
          MAGI = SQRT(IX**2.0 + IY**2.0 + IZ**2.0)
          IX = IX/MAGI
          IY = IY/MAGI
          IZ = IZ/MAGI
*
* Calculate incident skydome angles THET & PHI
*
          THET = ACOS(IZ)
*
* Set image arrays to zero if incident vector arrives from below the horizon
* [i.e., if 2*OMEGA > 90 deg; or if THET > 90 deg]
*
          IF (THET.GT.HALFPI) THEN
                  ISRF(I,J) = 0.0
                  QSRF(I,J) = 0.0
                  USRF(I,J) = 0.0
                  PSRF(I,J) = 0.0
                  TSRF(I,J) = 0.0
                  I000(I,J) = 0.0
                  I045(I,J) = 0.0
                  I090(I,J) = 0.0
                  I135(I,J) = 0.0
                  GOTO 4
          ENDIF
*
          IF (THET.GT.0.0) THEN
                  PHI = ATAN2(IY,IX)
          ELSE
                  PHI = 0.0
          ENDIF
*
* Calculate radiance magnitude of incident skydome vector I
* [CIE sky radiance model (after Hopkinson)]
*
1    COSMU = COS(THET0)*COS(THET)+SIN(THET0)*SIN(THET)*COS(PHI0-PHI)
     MU = ACOS(COSMU)
     A = 0.91+10.0*EXP(-3.0*MU)+0.45*(COSMU**2.0)
*
          IF (THET.LT.HALFPI) THEN
                  B = 1.0-EXP(-0.32/COS(THET))
          ELSE
                  B = 1.0
          ENDIF
*
2         IF (MU.EQ.0.0) THEN
                  PSI = 0.0
                  COSNU = 1.0
                  NU = 0.0
          ELSE
                  COSMU2 = COSMU**2.0
                  PSI = POL_MAX*((1.0-COSMU2)/(1.0+COSMU2))
*
* P = Polarization Vector (vector orientation of the polarization ellipse
*   = cross product of Sun Vector & Sky Element Vector = S x Q
*
* Analyze unit vector Q & S into xyz components
* [Q = |I|]
*
                  QX = SIN(THET)*COS(PHI)
                  QY = SIN(THET)*SIN(PHI)
                  QZ = COS(THET)
*
                   = SIN(THET0)*COS(PHI0)
                  SY = SIN(THET0)*SIN(PHI0)
                  SZ = COS(THET0)
*
* Calculate the cross product, P = S x Q
```

167

```
*
                PX = SY*QZ - SZ*QY
                PY = SZ*QX - SX*QZ
                PZ = SX*QY - SY*QX
*
* Calculate orientation angle NU of the polarization ellipse
* Rem: Y-axis runs + to - for quadrant I & II calculations
*
                IF (ABS(PY).GT.0.0) THEN
                        NU = ATAN(PX/PY)
                ELSE
                        NU = 0.0
                ENDIF
*
        COSNU = COS(NU) .
        ENDIF
*
        ISRF(I,J) = LREF*A*B/C
        QSRF(I,J) = ISRF(I,J)*PSI*COS(2.0*NU)
        USRF(I,J) = ISRF(I,J)*PSI*SIN(2.0*NU)
        PSRF(I,J) = PSI
        TSRF(I,J) = NU
*
* Rotate Stokes vector to reference plane of reflecting facet
*
        QTMP = COS(-ALPH)*QSRF(I,J)+SIN(-ALPH)*USRF(I,J)
        UTMP = -SIN(-ALPH)*QSRF(I,J)+COS(-ALPH)*USRF(I,J)
        QSRF(I,J) = QTMP
        USRF(I,J) = UTMP
*
* Calculate perpendicular & parallel reflection coefficients for
* incident angle OMEGA, refraction angle RHO, & refractive index N_MAG
*
        IF (ABS(OMEGA).EQ.0.0) OMEGA = 0.00000001
*
        RHO = ASIN(SIN(OMEGA)/N_MAG)
        RPAR = -TAN(OMEGA-RHO)/TAN(OMEGA+RHO)
        RPRP = -SIN(OMEGA-RHO)/SIN(OMEGA+RHO)
*
* Specify Mueller matrix for reflecting dielectric surface
* [MDIAG = M11 = M22, MOFFD = M12 = M21, MDIAQ = M33]
*
        MDIAG = 0.5*(RPRP**2.0 + RPAR**2.0)
        MOFFD = 0.5*(RPRP**2.0 - RPAR**2.0)
        MDIAQ = -RPRP*RPAR
*
* Multiply reflection Mueller matrix by Stokes vector
*
        ITMP = MDIAG*ISRF(I,J) + MOFFD*QSRF(I,J)
        QTMP = MOFFD*ISRF(I,J) + MDIAG*QSRF(I,J)
        UTMP = MDIAQ*USRF(I,J)
*
* Specify Mueller matrix for depolarizing interface
* [MDIAG = M22 = M33, M11 = 1.0]
*
        MDIAG = DEPOL
*
* Multiply depolarization Mueller matrix by Stokes vector
*
        ISRF(I,J) = ITMP
        QSRF(I,J) = MDIAG*QTMP
        USRF(I,J) = MDIAG*UTMP
*
* Rotate Stokes vector back to reference plane of polarizer
*
        QTMP = COS(ALPH)*QSRF(I,J)+SIN(ALPH)*USRF(I,J)
        UTMP = -SIN(ALPH)*QSRF(I,J)+COS(ALPH)*USRF(I,J)
```

```
            QSRF(I,J) = QTMP
            USRF(I,J) = UTMP

*
* Calculate reflected surface intensity from reflected radiance via finite surface
* facet attenuation and projection to sensor:
* ATT(omega,beta) = cos(omega)*sec(beta) = cos(omega)/cos(beta)
*
            IF (BETA.LT.HALFPI) THEN
                    ATT = COSOMEGA/COS(BETA)
            ELSE
                    WRITE(*,*) 'Beta > 90 deg: surface is non-analytic'
                    WRITE(*,*) 'setting radiance attenuation coefficient to 0'
                    ATT = 0.0
            ENDIF
*
            ISRF(I,J) = ISRF(I,J)*ATT
            QSRF(I,J) = QSRF(I,J)*ATT
            USRF(I,J) = USRF(I,J)*ATT
*
            PSRF(I,J) = SQRT(QSRF(I,J)**2.0 + USRF(I,J)**2.0)/ISRF(I,J)
            TSRF(I,J) = 0.5*ATAN2(USRF(I,J),QSRF(I,J))
*
* Multiply non-ideal linear polarizer Mueller matrices by Stokes vector
* for four polarizing angles: 0, 45, 90, and 135 degrees - to obtain
* I(0), I(45), I(90), and I(135)
*
            I000(I,J) = 0.5*(K_1 + K_2)*(ISRF(I,J) + QSRF(I,J))
            I045(I,J) = 0.5*(K_1 + K_2)*(ISRF(I,J) + USRF(I,J))
            I090(I,J) = 0.5*(K_1 + K_2)*(ISRF(I,J) - QSRF(I,J))
            I135(I,J) = 0.5*(K_1 + K_2)*(ISRF(I,J) - USRF(I,J))
*
* Calculate maximum intensities for each of the intensity distributions
* I(0), I(45), I(90), and I(135)
* [I(0) & I(90) are image pairs; I(45) & I9135) are image pairs]
*
            IF (I000(I,J).GT.IMAX1) IMAX1 = I000(I,J)
            IF (I090(I,J).GT.IMAX1) IMAX1 = I090(I,J)
            IF (I045(I,J).GT.IMAX2) IMAX2 = I045(I,J)
            IF (I135(I,J).GT.IMAX2) IMAX2 = I135(I,J)
*
4           ENDDO
            ENDDO
*
            WRITE(*,*) ' '
            WRITE(*,*) 'Starting 2nd loop ... '
            WRITE(*,*) 'IMAX1,IMAX2 = ',IMAX1,IMAX2
            WRITE(*,*) ' '
*
            DO I = P+1,Q
            DO J = P+1,Q
*
* Calculate effective intensity measured by sensor: effect of film exposure
* + effect of film processing + effect of digital transformation
* [I_eff = DN_max*((I+bias)^(-gamma_eff))]
*
            I000(I,J) = I000(I,J) + BIAS
            I045(I,J) = I045(I,J) + BIAS
            I090(I,J) = I090(I,J) + BIAS
            I135(I,J) = I135(I,J) + BIAS
*
            I000(I,J) = FLOAT(INT(DN_MAX*((I000(I,J)/IMAX1)**(-GAMMA))))
            I090(I,J) = FLOAT(INT(DN_MAX*((I090(I,J)/IMAX1)**(-GAMMA))))
            I045(I,J) = FLOAT(INT(DN_MAX*((I045(I,J)/IMAX2)**(-GAMMA))))
            I135(I,J) = FLOAT(INT(DN_MAX*((I135(I,J)/IMAX2)**(-GAMMA))))
*
* Recalculate Stokes images from intensity images
*
```

169

```
        ISRF(I,J) = 0.5*(I000(I,J) + I045(I,J) + I090(I,J) + I135(I,J))
        QSRF(I,J) = I000(I,J) - I090(I,J)
        USRF(I,J) = I045(I,J) - I135(I,J)
*
        IF (ISRF(I,J).NE.0.0) THEN
                PSRF(I,J) = SQRT(QSRF(I,J)**2.0 + USRF(I,J)**2.0)/ISRF(I,J)
        ELSE
                PSRF(I,J) = 0.0
        ENDIF
*
* Recalculate Stokes derivative images from Stokes images
*
        IF (USRF(I,J).NE.0.0) THEN
                TSRF(I,J) = 0.5*ATAN2(USRF(I,J),QSRF(I,J))
        ELSE
                TSRF(I,J) = 0.0
        ENDIF
*
        ENDDO
        ENDDO
*
    RETURN
    END
```

Appendix B   **Vita**

Name: Jan Arthur North

Date & Place of Birth: 17 January 1956
                               Oshkosh Wisconsin

Education:

High School   Burlington High School
1974   Burlington Wisconsin

BA in Biochemistry   Lawrence University
1978   Appleton Wisconsin

MS in Imaging Science   Rochester Institute of Technology (RIT)
1989   Rochester New York

Employment: United States Air Force   (1983 - Present)

                               1983 - 1987 Satellite Operations Director
                                            Air Force Satellite Control Facility
                                            Sunnyvale California

                               1987 - 1989 Graduate Student Officer at RIT
                                            & Education With Industry (EWI)
                                            Participant with Eastman Kodak
                                            Rochester New York

                               1989 - 1993 Ground Systems Engineer
                                            White Sands Missile Range
                                            White Sands New Mexico

                               1993 - 1995 Graduate Student Officer at
                                            SUNY CESF
                                            Syracuse New York

                               1995 -   Staff Scientist
                                            Central Imagery Office
                                            Vienna Virginia